DESIGN, FABRICATION, AND CHARACTERIZATION OF MICRO THERMAL ACTUATORS

A THESIS SUBMITTED TO
THE GRADUATE SCHOOL OF NATURAL AND APPLIED SCIENCES
OF
MIDDLE EAST TECHNICAL UNIVERSITY

BY

BUĞRAHAN GÜLCÜLER

IN PARTIAL FULFILLMENT OF THE REQUIREMENTS
FOR
THE DEGREE OF MASTER OF SCIENCE
IN
MECHANICAL ENGINEERING

SEPTEMBER 2020

Approval of the thesis:

DESIGN, FABRICATION, AND CHARACTERIZATION OF MICRO THERMAL ACTUATORS

submitted by **BUĞRAHAN GÜLCÜLER** in partial fulfillment of the requirements for the degree of **Master of Science** i**n Mechanical Engineering, Middle East Technical University** by,

Prof. Dr. Halil Kalıpçılar
Dean, Graduate School of **Natural and Applied Sciences** _____

Prof. Dr. M. A. Sahir Arıkan
Head of the Department, **Mechanical Engineering** _____

Assoc. Prof. Dr. Kıvanç Azgın
Supervisor, **Mechanical Engineering, METU** _____

Examining Committee Members:

Prof. Dr. Haluk Külah
Electrical & Electronics Eng., METU _____

Assoc. Prof. Kıvanç Azgın
Mechanical Eng., METU _____

Assoc. Prof. Sezer Özerinç
Mechanical Eng, METU _____

Assoc. Prof. Ulaş Yaman
Mechanical Eng., METU _____

Asst. Prof. Erdinç Tatar
Electrical & Electronics Eng., Bilkent University _____

Date: 23.09.2020

I hereby declare that all information in this document has been obtained and presented in accordance with academic rules and ethical conduct. I also declare that, as required by these rules and conduct, I have fully cited and referenced all material and results that are not original to this work.

Name Last name : Buğrahan Gülcüler

Signature :

ABSTRACT

DESIGN, FABRICATION, AND CHARACTERIZATION OF MICRO THERMAL ACTUATORS

Gülcüler, Buğrahan
Master of Science, Mechanical Engineering
Supervisor: Assoc. Prof. Kıvanç Azgın

September 2020, 115 pages

This thesis presents the design, fabrication, and characterization of V-Type thermal actuators, which will be used in an actuator system that is planned to be a tensile and compressive test setup to characterize the expandible cells by the help of double-ended tuning fork resonators as a force sensing mechanism. Actuators are serially packed to increase the generated force by them while maintaining the same deflection values. They have been connected to the overall system by springs to create a force on test subjects in both compressive and tensile states. In order to cut the effect of high-temperature values generated from the actuators, cooling fingers have been added just after the actuators. Two large plates are designed on the actuator system to put the test subjects. While one side of the actuator system consists of actuators packs and one of the plates, the other side consists of the other plate and the force-sensing mechanism. Between these two sides of the actuator system, the only connection will be test subjects. The cell attachment mechanism and other biology-related research are not the focus of the interest of this thesis. On the other side of the sensor, the force sensing mechanism consists of Double Ended Tuning Forks, DETF, as a resonant sensor. Modeling, design, and characterization of the

DETF are discussed extensively. After the fabrication, characterization tests of the actuators takes place. It has been seen that the mathematical model and COMSOL analysis for the actuators hold the test results.

For 8V of voltage values, 8-9 μm deflection values have been obtained in a maximum temperature of $\sim$700 K and an average temperature of $\sim$560 K. Similarly; fabricated DETF structures have been tested to see the performance of DETF under both vacuum and air conditions. It has been observed that DETF has two modes around 70 kHz, the in-phase mode in 69 kHz and out-of-phase mode in 72 kHz. It has also been shown that proof mass voltage only affects the amplitude and not affects the natural frequency of the DETF. Also, the quality factor for both vacuum and air conditions are obtained as 23316 and 182. The in-phase mode and the out-of-phase mode have a 3kHz difference because of the stiffnesses on the connections. It has also been verified by the mathematical model and COMSOL analysis. The tests to find the sensibility of the DETF could not be done since both plates on every sensor broke down. Only mathematical model and COMSOL results for the force sensibility has been studied.

Keywords: MEMS Thermal Actuator, MEMS V-Type Actuator, MEMS DETF Resonator, Double-Ended Tuning Fork, MEMS Tensile and Compressive Test Setup

ÖZ

MİKRO TERMAL EYLEYİCİLERİN TASARIMI, ÜRETİMİ VE KARAKTERİZASYONU

Gülcüler, Buğrahan
Yüksek Lisans, Makina Mühendisliği
Tez Yöneticisi: Doç. Dr. Kıvanç Azgın

Eylül 2020, 115 sayfa

Bu tez uzayabilen kas hücrelerini karakterize etmek için tasarlanan bir termal eyleyici bazlı servo sisteminde kullanılacak olan V-Tipi termal eyleyicileri ve çift sonlu diyapazon kuvvet sensörlerinin tasarımın, üretimini ve karakterizasyonunu sunmaktadur. Eyleyiciler, aynı uzama değerlerini korurken, ürettikleri kuvveti artırmak için seri olarak paketlenmiştir. Hem sıkışma hem de gerilme durumlarında test denekleri üzerinde bir kuvvet oluşturmak için uçlarında yaylarla genel sisteme bağlanmışlardır. Eyleyicilerden üretilen yüksek sıcaklık değerlerinin etkisini azaltmak için eyleyicilerin hemen ucuna soğutma parmakları eklenmiştir. Denekleri yerleştirmek ve test etmek için eyleyici sistemi üzerinde iki büyük plaka konumlandırılmıştır. Eyleyici sisteminin bir tarafı eyleyici serisine diğer tarafı ise kuvvet algılama mekanizmasından oluşmaktadır. Eyleyici sisteminin bu iki tarafı arasındaki tek bağlantı ise denek veya denekler olacaktır. Hücre bağlanma mekanizması ve biyoloji ile ilgili diğer araştırmalar bu tezin ilgi odağında değildir, sadece mekanik tasarımı çalışılmıştır. Sensörün diğer tarafında kuvvet algılama mekanizması olarak Çift Sonlu Diyapazon rezonant sensörü, DETF'den oluşur. DETF'in modellenmesi, tasarımı ve karakterizasyonu kapsamlı bir şekilde incelenmektedir. Sensör üretiminden sonra eyleyicilerin karakterizasyon testleri

gerçekleştirilmiştir. Eyleyiciler için matematiksel model ve COMSOL analizinin test sonuçlarının birbiriyle tuttuğu görülmüştür. 8V gerilim değerleri için maksimum ~ 700 K sıcaklıkta ve ortalama ~ 560 K sıcaklıkta 8-9 μm sapma değerleri elde edilmiştir. Benzer şekilde, fabrikasyondan sonra DETF yapıları hem vakum hem de hava koşullarında DETF performansını görmek için test edilmiştir. DETF'in 70 kHz civarında iki moda, 69 kHz'de eş fazlı mod ve 72 kHz'de faz dışı moda sahip olduğu gözlemlenmiştir. DETF'e uygulanan DC gerilimin yalnızca büyüklüğü etkilediği ve DETF'nin doğal frekansını etkilemediği de gösterilmiştir. Ayrıca hem vakum hem de hava koşulları için kalite faktörü 23316 ve 182 olarak elde edilmiştir. Eş faz mod ile faz dışı mod bağlantılardaki sertliklerden dolayı 3kHz farka sahiptir. Bu durum matematiksel model ve COMSOL analizi ile de doğrulanmıştır. Her sensördeki her iki plaka da üretim sırasında kırıldığı için DETF'nin hassasiyetini bulmaya yönelik testler yapılamamıştır. Kuvvet duyarlılığı için sadece matematiksel model ve COMSOL sonuçları incelenmiştir.

Anahtar Kelimeler: MEMS Termal Eyleyici, MEMS V-Tipi Eyleyici, MEMS DETF Resonatör, Çift Sonlu Ayar Çatalları, MEMS Sıkışma ve Gerilme Test Sensörü

To my lovely mother, father, and sweetheart…

ACKNOWLEDGMENTS

First and foremost, I would like to express my deep and sincere thanks to my thesis advisor, Assoc. Prof. Kivanc Azgın for his support, guidance, and encouragement during my graduate studies.

I would like to express my deep gratitude to everybody working on the METU MEMS Center for sharing their knowledge and always-friendly attitudes during my M.Sc. study. I learned many new things because of their guidance.

I would like to thank my colleague, Ertuğ Şimşek, for his support on design, fabrication steps, and every other detail of this thesis. I could not finish this thesis without his support, knowledge, and mentorship. Also, I would like to thank my office mates, Ahmet Gülsaran, Bahar Atik, Baran Utku Şimşek, Batuhan Beşcan, Büşra Erdoğan, Emrah Dirican, Emre Ersoy, Esin Gül, Gürel Dimez, Meltem Okan, and Seval Şahin for their everyday support to complete my thesis. Also, I would like to thank A. Murat Yağcı and Kadir Ulak for their extraordinary work to finish my sensor packaging.

I would like to thank to my special friends, Alperen Tüğen, Büşra Karakoç, Denizhan Erdoğan, Kemal Güçhan Kar, Oğuz Örs, Sevgi Ericek, Tuğçe Canbilen and Yusuf Mahir Nartok, although I know that there is no way to express my gratitude to have you around me.

I would like to thank my family, Emrah Gülcüler and Filiz Kenkül, for their endless support, love, and encouragement for everything I do.

Lastly, I would like to thank my sweetheart, Imren Karalar, for her support, love, and endless patience towards me; I could not make it without her.

TABLE OF CONTENTS

LIST OF TABLES

TABLES

LIST OF FIGURES

FIGURES

CHAPTER 1

1. INTRODUCTION

All human beings have orphans in their bodies to keep vital activities running. In order for orphans to keep working, they need blood, and that is where the heart takes responsibility. It pumps blood to every corner of the human body to make sure things run smoothly. They are made of cardiac muscle or heart muscle. In cardiac muscle, there are little cells called cardiomyocytes or cardiac muscle cells that have long chains of sarcomeres. Sarcomeres are the essential parts of the muscle cells since they are the contractile units.

In order to the heart to pump blood through the body, its cardiomyocytes should be forcibly contracted. Since the cardiomyocytes are a vital part of the heart, any problem about them could be the reason for devastating results. It is known that cardiac tissues have a pretty low capability to restore or regenerate themselves. In order to heal the tissue during a severe problem, different approaches should be followed. [1]–[5] One of the approaches is stem cell-derived cardiomyocytes. These cardiomyocytes can be used to repair the damaged regions of the cardiac muscle. Currently, in addition to its capability of repairing the damaged regions of the cardiac muscle, stem cell-derived cardiomyocytes have been used in different areas such as potential drug treatments [4]–[6] and to restore the heart function. [1], [7] Nevertheless, in all these studies, it had been found that the contractile output of stem cell-derived cardiomyocytes is much smaller than their adult counterparts. The reason for this situation is their small and round morphology and their sarcomeric structure. Therefore, characterizing and studying the contractile behavior of the stem cell-derived cardiomyocytes is essential.

It has been seen that the traditional methods of cell culturing can not model organ microenvironments accurately. Likewise, methods that involve animal testing results

in the same problem. It was estimated that only one-third of the successful animal tests had been transformed into succeeding human clinic trials. This is mostly a result of different methods that have been used in animal tests and human trials and the differences between the species. [8]–[11]

By creating a model of the patient, preclinical evaluation methods can be designed more effectively. It has been known that the stem cell can provide the patient-relevant foundation to realize the in vitro modeling. These stem cells have different characteristics of the patients such as age, sex, or ethnicity. [12] Organs on Chips are the tools to be used in this foundation to mimic the structure and the function of the patient for necessary tests. [13]

MEMS can be a great foundation to create a chip that can be the basis to mimic the structure and the function of the patient. By combining MEMS technologies and biosystems, a new system to characterize and study the contractile behavior of the stem cell-derived cardiomyocytes can be designed.

In this thesis, an actuator system which will be developed to create the basis for testing of muscle cells is studied. In Chapter 1.1, an Overview of MEMS Test Setups studied in the literature will be presented. Immediately after, Overview of MEMS Thermal Actuators and Overview of MEMS Resonators will be presented. Finally, at the end of Chapter 1, Objectives and Organization of Thesis Study will be mentioned.

1.1. **Overview of MEMS Test Setups**

In MEMS, in order to mimic the structure and the function of the patient, many designs have been studied in the literature. Until now, most of the proposed methods have been measuring the contractile force of the cardiomyocytes by optical-based tools. All of these proposed methods have used micropillar arrays

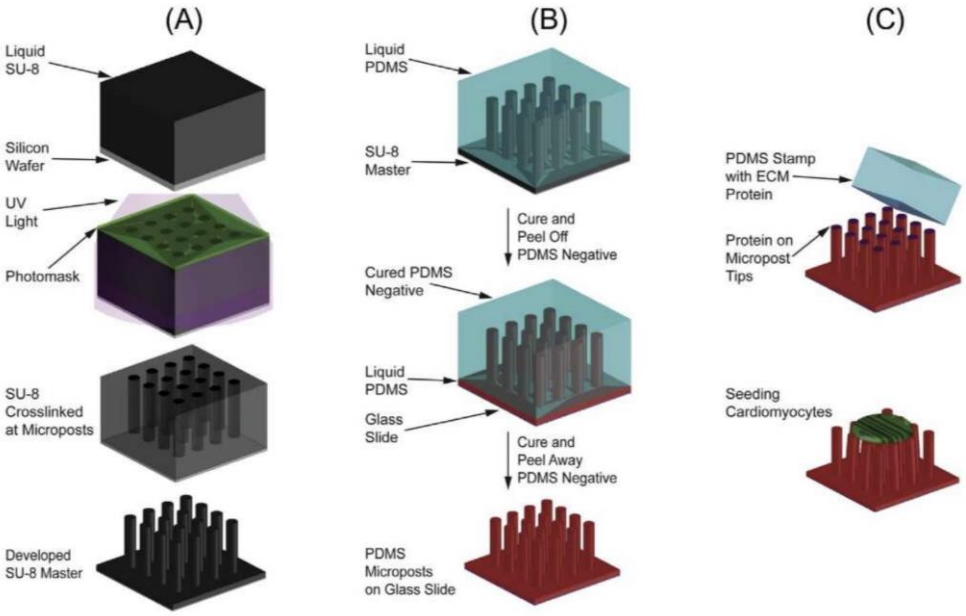

Figure 1. Lithography, manufacturing and microcontact printing processes of micropost that has been designed in [14]

for measuring the contractile force. In these methods, cardiomyocytes are cultured on micropillar covered substrate, and the contractile force is estimated by optically measuring the deflection of the micropillars. [14]–[18] Another way to use the optic-based tools is by using fluorescent microbeads. [19]–[21] By culturing the cardiomyocytes on the substrate, which is covered by fluorescent microbeads.

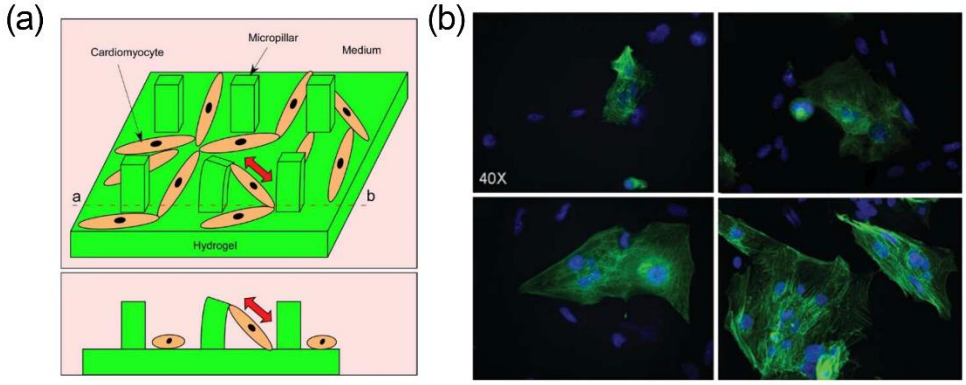

Figure 2. (A) Design and Actuation principle of hydrogel micropillars [15] (B) Human embryonic stem-cell derived cardiomocytes in which immnostaining performed on them to image cardiomyocytes and compare cellular morphology as a function of substrate stiffness.

When the cardiomyocytes are contracted, this will result in the deformation of the substrate. By following the deflection of fluorescent microbeads by optic-based tools, the contractile force of the cardiomyocytes can be estimated. The problem with these methods is the low temporal resolution of the optical-based tools.

Measuring the force by mechanical tools can be the result of increased resolution. One of the mechanical ways to measure this force is by using the piezoresistive cantilevers. [22]–[24] By bending the piezoresistive cantilevers by contractile force, the resistance change of the piezoresistors can be measured. Another studied method, which also includes piezoresistive sensing elements, measure both high stiffness and high force sensitivity of the substrate. [25] In addition to this, there is also a high-sensitivity tri-axis force sensor which consists of both piezoresistors and a micropillar to measure the cellular traction force of a single cell. [26] All these methods are passive stimulation methods that can only sense the forces created by the cell, which means there is no external force from the medium. However, many studies implement active

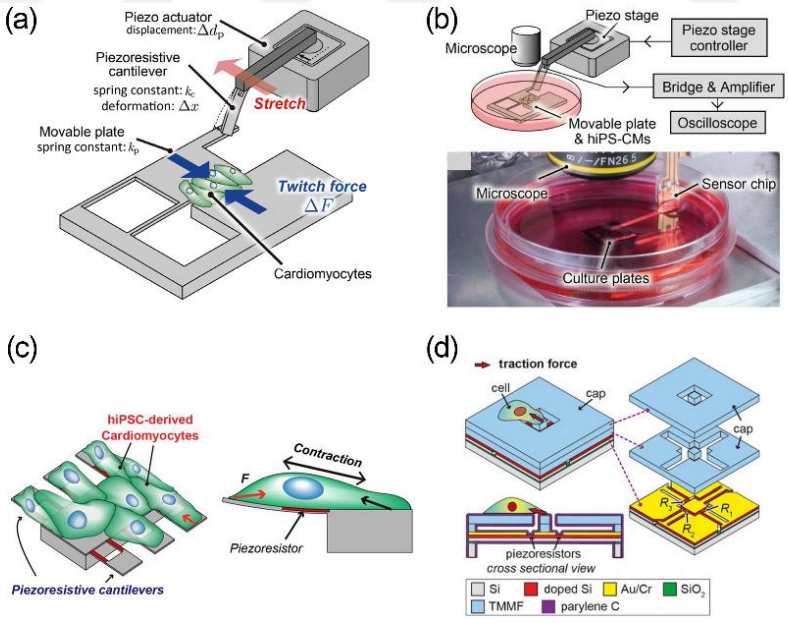

Figure 3. (A) Piezo stage design and (B) test setup [22], (C) Piezoresistor design [23] and (D) Tri-axis force sensor design [26]

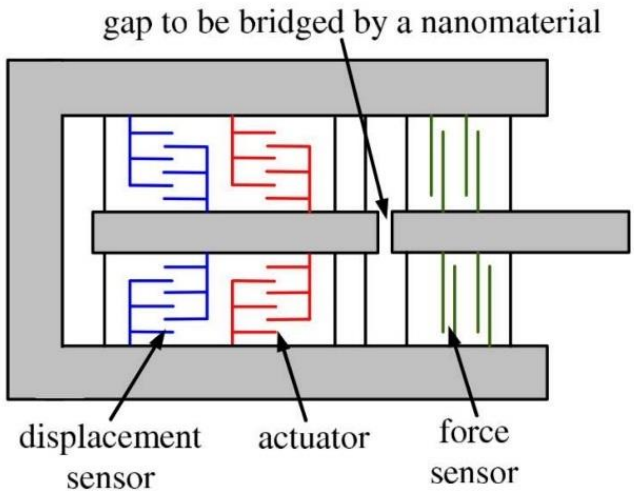

Figure 4. Schematic of the MEMS Tensile test setup device which integrates an actuator and two sensors. [35]

stimulation methods to see its effects on cells. All these studies have been performed in non-MEMS systems. These studies include the following physics to create a mechanical force on cells; Optical tweezers, [25], [27], [28] Magnetic tweezers [29]–[31], and Acoustic tweezers. [32] By combining MEMS and active stimulation methods, a more effective system can be obtained to track the force generation by cells in different environmental mediums.

By using MEMS technology, various test setups for non-bio material testing have already been developed in the literature. Some of these test setups include membranes to measure the different mechanical properties [33], [34], some of them include electrostatic comb-drive actuators [35], [36], and others include thermal actuators [37]–[42] to generate a mechanical force on specimens.

There are different approaches to connect the specimen to the assembly; for example, gripper assembly [41] or mounting gaps between actuator and force sensor have been used in different systems. [38] Using these MEMS tensile test setup mechanism, it is desired to create a system where biological cells can be used as the specimen. In this way, their behavior under different mechanical stimuli (compressive and tensile) can be measured.

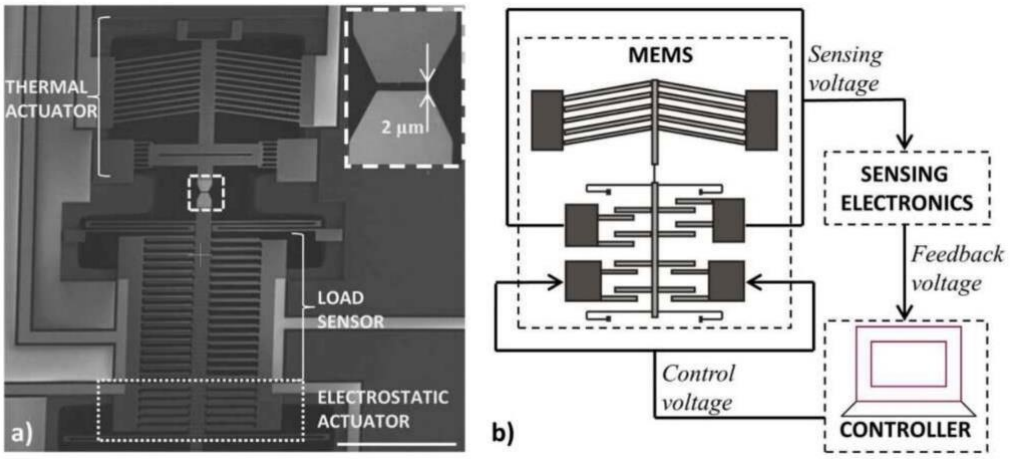

Figure 5. Schematic of the MEMS Tensile test setup device, which integrates an actuator and two sensors. [35]

There should be three parts to be considered in order to design such a test setup, the actuation part, cell attachment part, and the force-sensing part. In order to put the cells without any problem, two 500x1000 um plates have been placed with 10μm apart to place the one end of the cell to the one plate and the other end of the cell to the other plate. It has been shown that cardiomyocyte's length differs from ~75μm to ~150μm while their width differs from

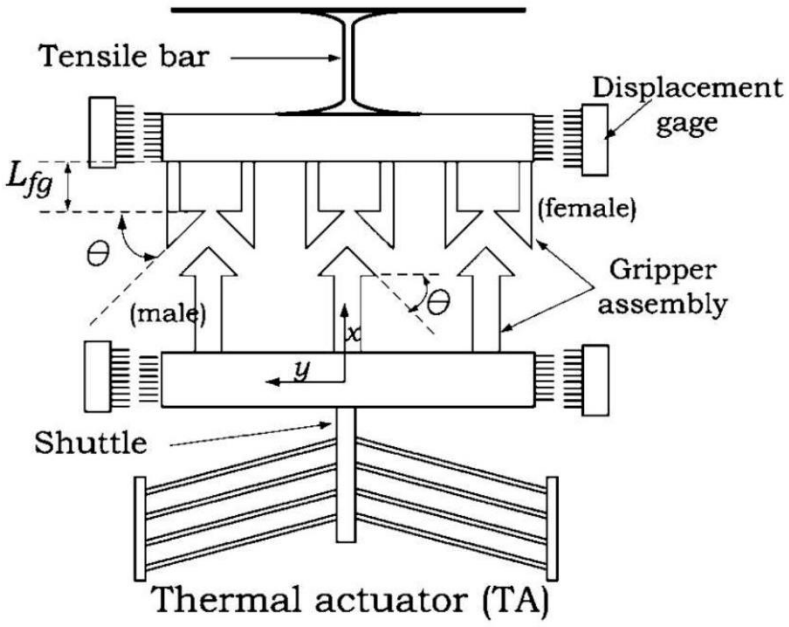

Figure 6. Gripper Assembly on a tensile test setup. [41]

~30 µm to ~40 µm. Creating a 10µm space between the plates means there will be no problem for cardiomyocytes to hold on to the plates. These two plates will be connected to the anchors around them by flexible elements, i.e., rollers. One of these plates will be connected to the actuation part while the other will be connected to the force-sensing part. Moreover, the only connection between these two plates will be the cells. The plate which is connected to the actuators will move to a considerable extent while the other plate, which is connected to the force-sensing part, will almost stay steady because of the design of the force sensor.

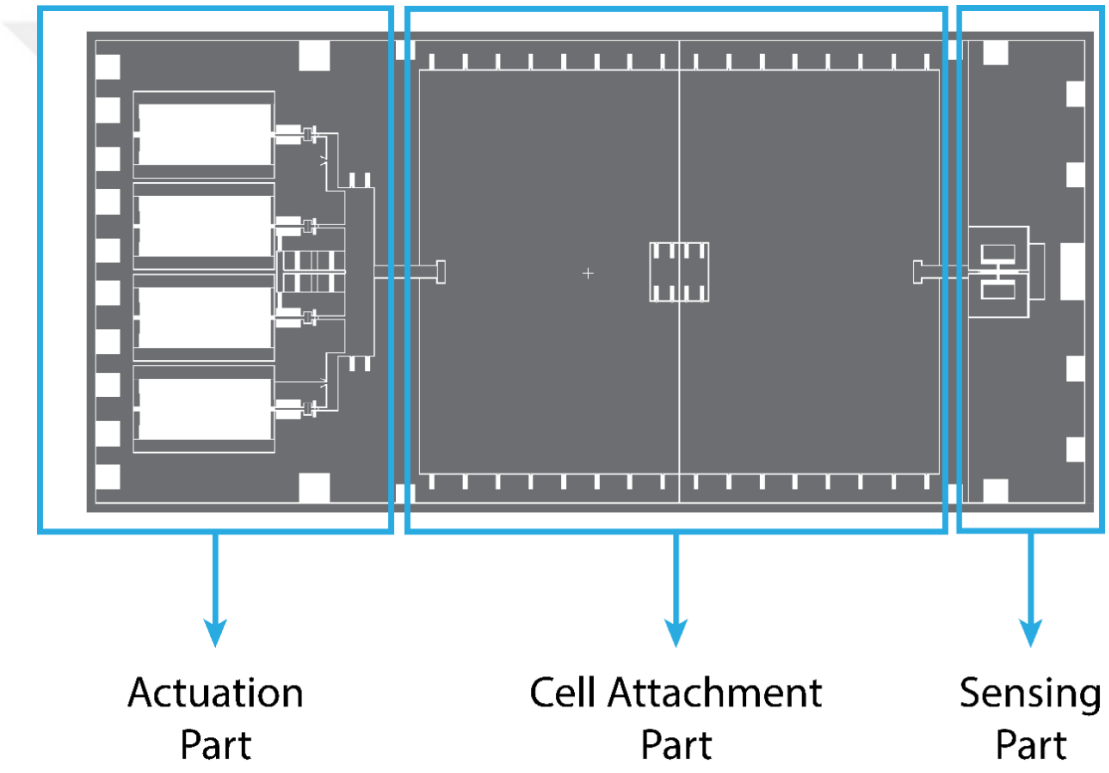

Figure 7. Design of Proposed MEMS-Based Tensile/Contractile Test Setup

The proposed design of the system can be seen in Figure 7, where the left-hand side is the actuation part, the middle part is the cell attachment part, and the right-hand side is the force sensing part. Since the middle part's introduction has been made in this chapter, both actuation and force sensing parts will be introduced in Chapter 1.2 and Chapter 1.3, respectively.

1.2. **Overview of MEMS Thermal Actuators**

In Microelectromechanical systems, MEMS, actuation is an essential part of most designs. There are many physics to use in order to create actuation. These physics can be sorted as; Electrostatic, Thermal, Piezoelectric, and Magnetic. [43] All these physics offer a different range for speed, resolution, power dissipation, and robustness. In literature, it has been seen that most of the micromechanical testing systems have used the thermal actuator because of its compact, stable, and high force output foundation. [44] They have been used in different applications such as micro-engines [45], positioners [46], micro x-y stages [47], and instrumentation for material characterization. [48] They are also used to increase displacement range for specific applications with compliant mechanisms. [46]

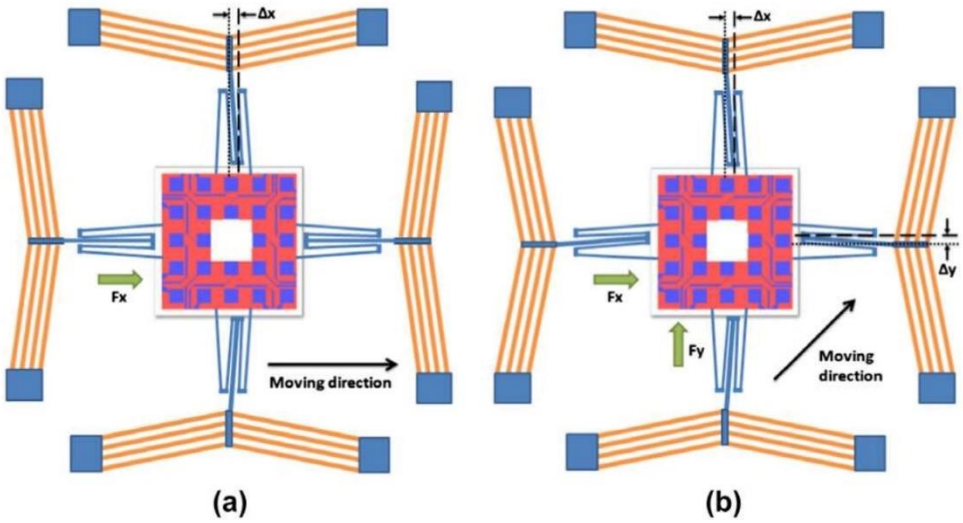

Figure 8. Illustration of the x-y stage (a) in the x-direction only and (b) in both x and y directions. [47]

In this study, the main focus will be on actuators to model, simulate, and test the performance of them. The working principle is the same for all MEMS thermal actuators. By applying a voltage difference along with the actuator, the system heats up because of the Joule heating. Because of the thermal expansion happening along with the actuator, it will deflect in the prescribed axis. Since the main idea is the

same, a difference occurs when the design and material properties change. There are three alternatives mostly used in literature to design thermal actuators. The first one is U-Type or hot arm thermal microactuators. [49] In this type of thermal actuators, there are two arms with different thicknesses. By applying a voltage difference along with the two anchors of the system, the thin arm heats up much more than the thick arm because of the increased electrical resistance, and this will result in asymmetric elongation of the arms, which creates a deflection in the whole system. In Figure 9, the design and motion direction of the hot arm thermal actuators can be seen.

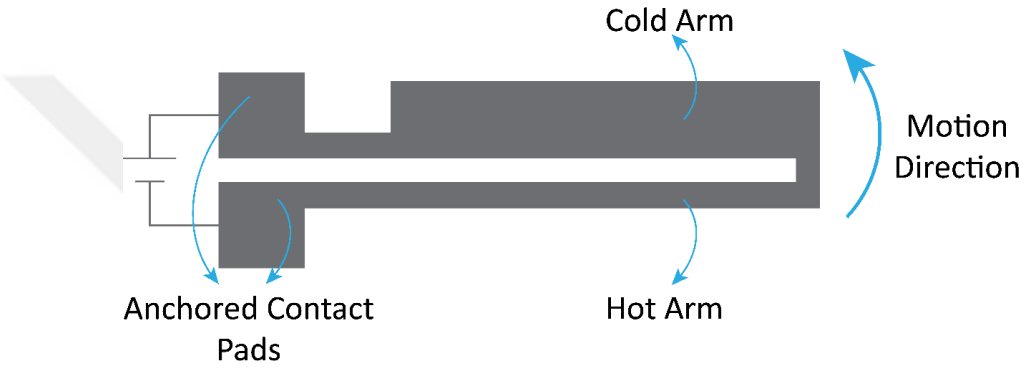

Figure 9. U-Type thermal actuator design with segment names and motion directions

The thin or cold arm has a narrow flexure section near the connection point of the arm. Linear motion can be generated by connecting two U-Type thermal actuators symmetrically around the central shuttle.

The second one is bimorph thermal actuators, which have two different layers that have different thermal expansion coefficients. By combining these two layers, a bimorph actuator can be constructed. By using this actuator, high force and low operating voltage can be achieved. However, there are some problems with this design; it consumes high electrical power, has an operating frequency, and has a laminated structure. [49] It has been widely used to generate motion in the z-direction. [50][51] The design and motion direction of the bimorph thermal actuators can be seen in Figure 10.

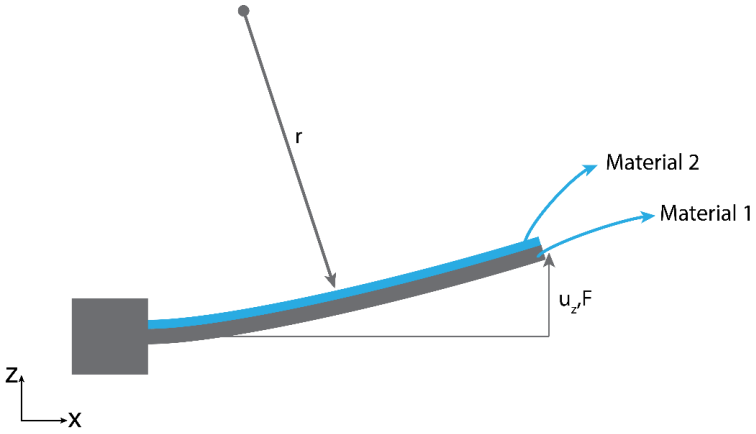

Figure 10. Bi-Morph thermal actuator with its design and motion direction

The third and last thermal microactuators are V-Type or Chevron type thermal microactuators. In this type, there are two bent beams which are symmetrical according to its shuttle. The design of the v-type actuator and deflection motion can be seen in Figure 11. [52], [53]

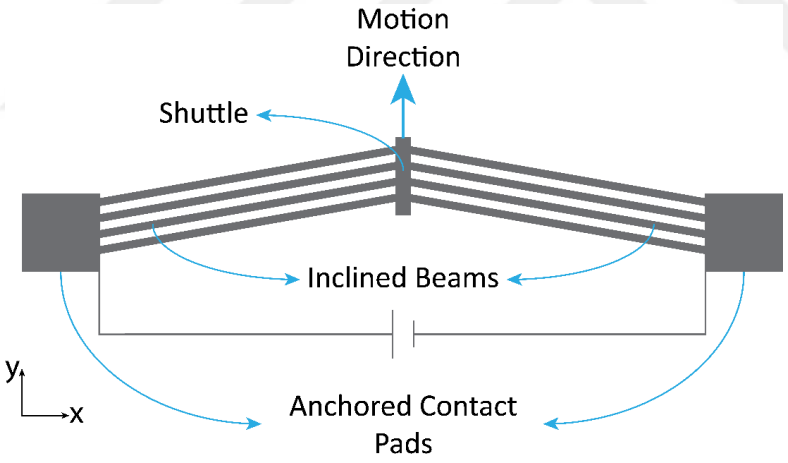

Figure 11. V-Type thermal actuator design with segment names and motion directions

Compared to traditional electrostatic comb-drive or parallel plate actuation methods, this type of thermal actuators can achieve a hundred times higher output force and ten times lower actuation voltages. At the same time, the much smaller area has been consumed and frictionless motion have been achieved. [54]

In this type of thermal actuators, electric, thermal, and structural fields have been coupled as in other types of thermal actuators. By applying a voltage along with the anchors of the actuators, beams heat up as a result of Joule Heating, and because of the thermal expansion, beams move in the prescribed axis. The reason for the bent beam design is to create this prescribed motion. Because of the bending of the beams, they will always buckle in the +y axis.

Many papers have reported methods to model the coupled behavior of the design. Some of these papers studied the electro-thermal coupling of the design by generating a voltage-dependent temperature formula. [55]–[58] In these studies, heating by resistance has been studied. Other papers studied the thermo-mechanical coupling of it by generating the temperature-dependent deflection formula. [38], [59]–[63] In addition to those, some papers studied the fully coupled v-type actuators by combining electrothermal and thermomechanical couplings; however, most of the studies have very little detail about the outcomes of the fully coupled model. [54], [64]–[67] There are also studies for the fully coupled 3D finite element analysis, which has been generated in different software. [68] Only [38] have been studied the v-type actuators in a fully coupled analytical method in detail. There are also studies about characterizing temperature-dependent electrothermal properties of the materials used in these actuators. [44]

In this thesis, an analytical model of a fully coupled V-Type thermal actuator will be examined. First, the system will be modeled, and then, this model will be verified by COMSOL finite element analysis.

1.3. **Overview of MEMS Resonators**

MEMS resonators have been used in people's life quite extensively. They can be combined with many other MEMS devices to create larger systems. The reason they have been used extensively is that they have simple principles of operation. [69] Both industrial companies and research-focused groups are using these types of MEMS

sensors in a variety of areas, including photonic, acoustic, and optical systems. [70]–[74] In these areas, different types of MEMS resonators have been developed, such as bulk acoustic wave resonators, ring resonators, and contour mode plate resonators. In addition to those sensors, double-ended-tuning-fork type resonators are used more and more every day. The popularity of them arises from its strain-sensitive tines.

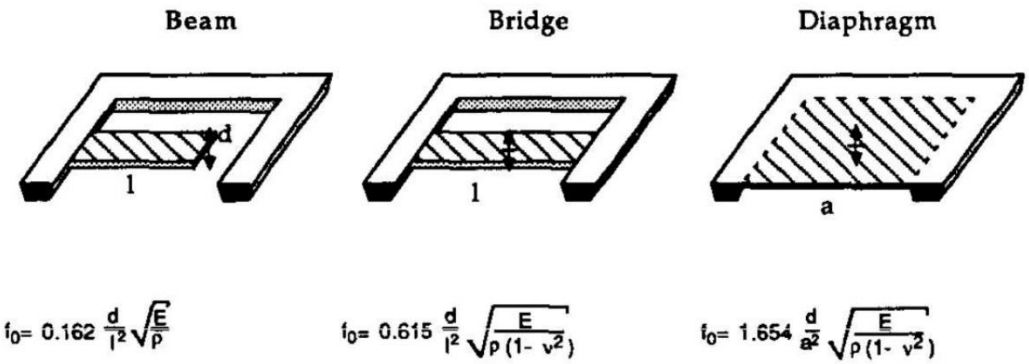

Figure 12. Three basic resonant structures and their flexural resonance frequencies [69]

In the literature, many studies reported the strain effects on the DETF tines. This strain effects cause the frequency shift of the lateral vibrational mode of the double-ended-tuning fork tines. In order to use the DETF structure as a physical sensor, targeted measurand should be expressed in terms of the frequency shift of the tines. By using this expression, MEMS Force sensors [75], pressure sensors [76], accelerometers with differential sensing [77], [78], and strain sensors [79] have been developed in the literature.

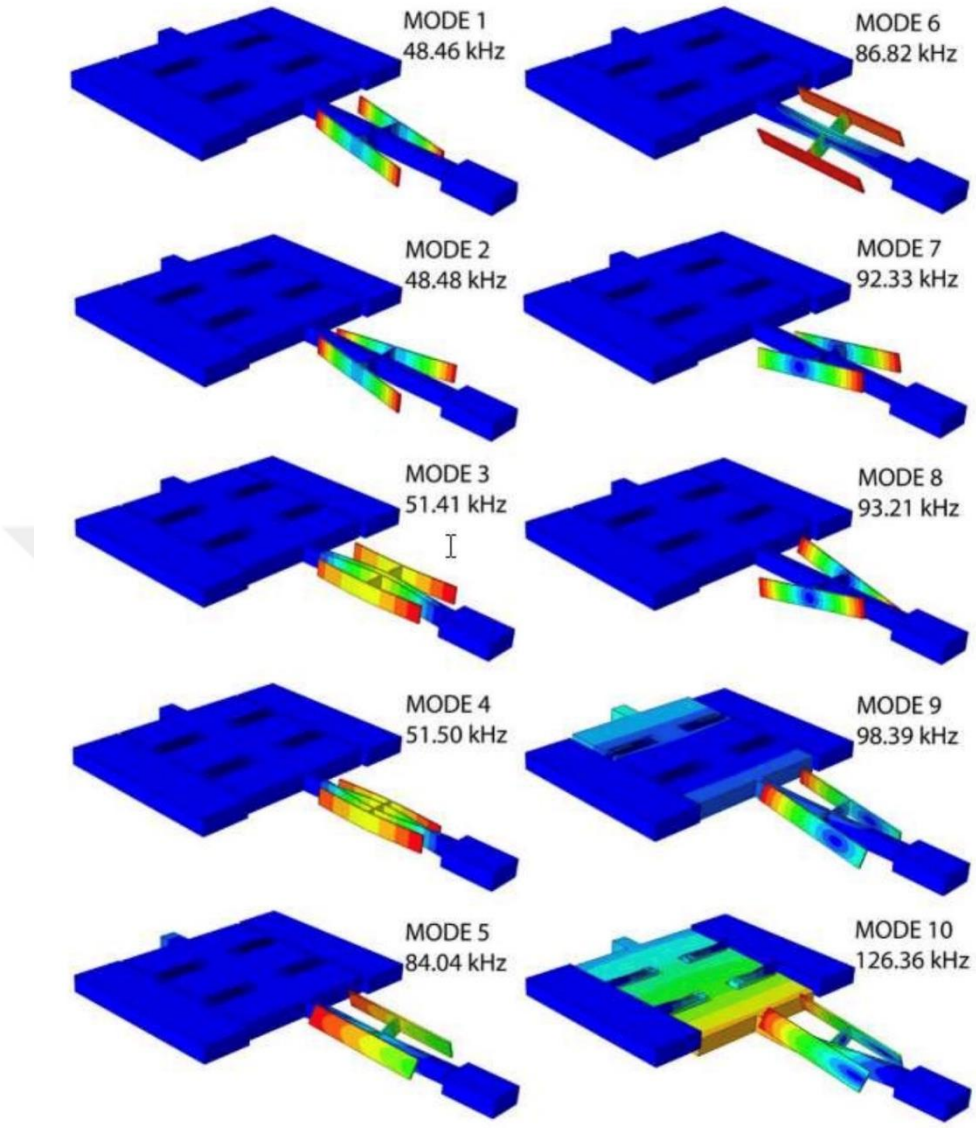

Figure 13. Zero load resonant mode shaped of the DETF. [75]

In Figure 14, the DETF design in this study has been presented. By applying an AC voltage difference by the Drive Electrodes in resonant frequency, Resonant Tuning Forks have been excited. Other pairs of electrodes, sense electrodes, sense the change in the capacitor gap with a specific time interval. The sense electrode also responds with an AC signal with a vibration frequency of the forks. [80][81]

When an external force has been applied to the tip of the resonator, the natural frequency of the tine's changes, this change can be detected by a feedback loop that can adjust the drive frequency to sustain the natural frequency.

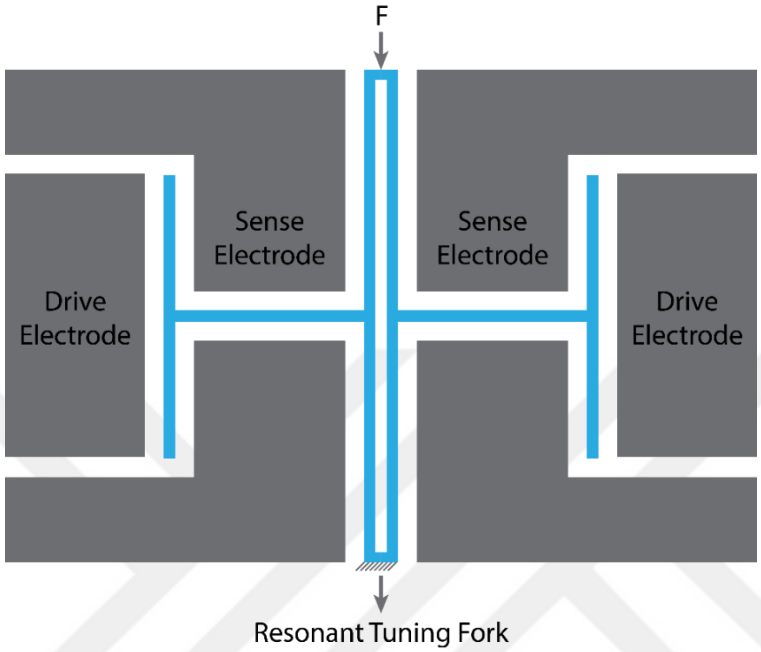

Figure 14. DETF design and its main parts

There is three-factor that affect the resolution of the DETF, geometric dimensions, the Quality factor to express the amount of electrical and mechanical losses, and the noise level of the electronic equipment.

1.4. **Objectives and Organization of Thesis Study**

The motivation of this thesis is to propose a brand-new thermal actuator-based servo system to create a basis to stimulate cardiomyocytes actively and other contractile cells in a MEMS-based system. Moreover, the objectives of this study are mainly focused on the design, analysis, fabrication, and execution of thermal actuators and resonant force sensor. When the objectives are divided into smaller parts, the following specific objectives can be listed:

- To create a detailed design procedure of MEMS-based thermal actuators to be presented with the parametric analytical models in order to optimize the force/deflection ratio.
- To create a detailed design procedure of MEMS-based force sensors to be presented with the parametric analytical models in order to optimize the sensitivity of the sensor.
- To create a detailed design procedure of MEMS-based test setup to be presented in order to create μm level deflection or nN level force on cells. This design will be verified by finite element analysis.
- In order to support the attachment plates and create both tensile and compressive force and deflection, flexible elements will be detailly analyzed.

The organization of this thesis will be presented below by explaining the context of each section below.

In Section 2, the operation principles of MEMS Thermal Actuators, MEMS Force Sensors, and MEMS Tensile Test Setups will be presented. For each of these MEMS systems, operation principles will be given together with design steps and Finite Element Analysis (FEM) results. Also, derived analytical models, their results, and comparison of them to FEA results will be discussed. Biological information will also be presented briefly in order to support the cell attachment part in the MEMS Tensile Test Setup section.

In Chapter 3, the fabrication process of the MEMS Tensile Test Setup is presented with the details of the fabrication process flow. Then, the necessary information about the fabrication process will be given. The fabrication results will also be presented in this section using SEM images of the fabricated sensors.

Chapter 4 shows the test procedures, preparation of the test setup, and test results of the fabricated sensors. The characterization tests of MEMS Actuators and Force Sensors are discussed in different sections extensively discuss the results. Overview of the system-level test results and deflection, force generation results are presented in tables to show the achievements of the thesis.

CHAPTER 2

2. DESIGN AND MODELLING OF MEMS TEST SETUPS, THERMAL ACTUATORS, AND FORCE SENSORS

In this chapter, the Design and Modelling of MEMS Test Setups, Thermal Actuators, and Force Sensors studied in this thesis will be discussed one by one in each subsection. Firstly, the Design needs of MEMS Thermal Actuators will be discussed in Chapter 2.1. Then, the Design needs of MEMS Force Sensors used in this study will be discussed in Chapter 2.2. After that, the Design needs of MEMS Tensile Test Setups will be discussed in Chapter 2.3. In Chapters 2.1, 2.2, and 2.3, operation principles, mechanical design, and Finite Element Modeling Simulations will be studied extensively.

2.1. **Design of MEMS Thermal Actuators**

MEMS Thermal Actuators have general use in many different actuation applications, as stated in Chapter 1.2. In this study, actuation is planned to be supplied by the V-Type MEMS Thermo-Electro-Mechanical Actuators since they are found as more robust and more reliable compared to other types of actuators. To explain the working principles of V-Type Thermal Actuators, firstly, operation principles of MEMS Thermal Actuators will be discussed. This will take place in Chapter 2.1.1 by analyzing the working principles of V-Type Thermal Actuators used in this study in detail. After understanding the working principles of V-Type Thermal Actuators, analytical modeling of the V-Type Thermal Actuators used in this study will be derived in Chapter 2.1.2. Lastly, by obtaining the Finite Element Modelling results, the accuracy of the derived analytical model of the V-Type Thermal Actuators used in this study and the results of the Finite Element Modelling Simulations will be presented in Chapter 2.1.3.

2.1.1 Operation Principles of MEMS Thermal Actuators Used in This Study

This Chapter will include three subsections to study V-Type Actuators in detail. In Chapter 2.1.1.1, the effects of applying a voltage to the actuators will be examined. To be more specific, the voltage-dependent temperature distribution across the actuator will be obtained. In Chapter 2.1.1.2, using the temperature distribution obtained in chapter 2.1.1.1, thermal expansion of the actuators will be derived. By deflection obtained by this temperature increase, there will also be a force generation in the system. This force generation will also be studied in the same chapter.

2.1.1.1. Heating of MEMS Thermal Actuator Used in This Study

There are three basic building blocks required to manipulate and utilize electricity: *Voltage, Resistance,* and *Current*. Electricity is defined as the movement of electrons as their nature electrons create a charge as they move, which can be harnessed to do work. Every technological device is harnessing the movement of the electrons in order to do this work. They all operate using the same fundamental power source: the movement of electrons.

The three basic principles can be explained using electrons, or more specifically, the charge they create:

- *Voltage:* the difference in electric potential between two points.
- *Current:* the rate at which charge is flowing through the material.
- *Resistance:* The material's tendency to resist the flow of charge, which depends on the geometry and material properties.

Ohm's Law states how all these affect each other. Ohm's Law states that through a conductor, the current between two points is directly proportional to the potential difference, voltage, across the same two points. Combining the elements of voltage, current, and resistance, Ohm developed the following formula,

$$V = IR \tag{1}$$

Where

- V: Voltage in Volts
- I: Current in amps
- R: Resistance in ohms

This equation is called Ohm's Law to express the relationship between voltage, current, and resistance.

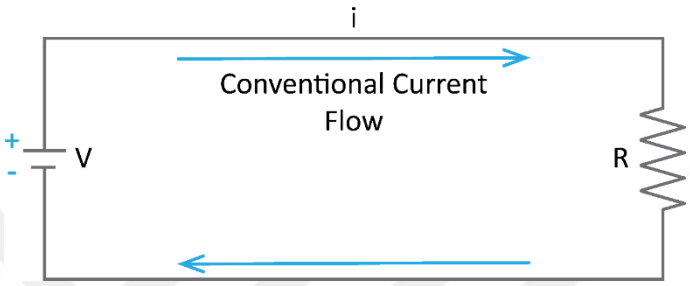

Figure 15. A simple circuit to present fundamental electricity principles

A circuit can be prepared to show how all of these elements are created. As can be seen in Figure 15, voltage is supplied by a generation device, generally a battery, there is resistance in the material, and because of the supplied voltage and the resistance, there exist current.

The resistance of a beam is defined as how hard for an electron to flow through that material. In mechanics, friction shares basic conception with the resistance. It is directly proportional to the length of the beam or wire,

$$R \propto L$$

It is also inversely proportional to the cross-sectional area of the beam or wire

$$R \propto \frac{1}{A}$$

Where the area is the $width \times height$ of the beam.

It is known that it is directly proportional to the resistivity of the material of the beam or wire;

$$R \propto \rho$$

Then, the resistance of a beam can be found by a given geometry and material property as;

$$R = \frac{\rho L}{A} \tag{2}$$

When the resistance equation is placed in Ohm's Law, the following equation can be obtained;

$$I = V\frac{A}{\rho L} \tag{3}$$

Joule Heating, which is also known as Ohmic heating or resistive heating, is a concept which happens when an electric current pass through a conductor. When the current flows, it produces heat because of the previously mentioned resistance. *Joule's First Law*, which is also known as the *Joule-Lenz Law*, describes the concept as the thermal energy converted from electrical energy because of the collision of charged particles with the ions in the conductor. It is found that the generated power is proportional to the square of current and resistance.

$$P \propto I^2 R$$

The fundamental formula for Joule heating is the multiplication of current with the voltage difference across the tip points or exerted power on the system by electrical means. It can be written as;

$$P = (V_A - V_B)I \tag{4}$$

- P: Power converted from electrical energy to thermal energy.
- I: Current traveling through the resistor or another element.
- $V_A - V_B$: is the voltage difference between the tip points of the beam.

In suitable conditions, *Ohm's Law* can be used, and when it is used, the formula can be written in other equivalent forms, such as;

$$P = IV = I^2 R = \frac{V^2}{R} \tag{5}$$

Any form of power representation above can be used in future calculations.

A primary objective in a conduction analysis is to determine the temperature field in a medium resulting from conditions imposed on its boundaries. That is, it is wished to know the temperature distribution, which represents how temperature varies with position in the environment. When this distribution is known, the conduction heat flux at any point in the environment or on its surface may be computed from *Fourier's Law of Heat Conduction*. Other significant quantities of interest may also be determined. For a solid structure, knowledge of the temperature distribution could be used to ascertain structural integrity through the determination of thermal stresses, expansions, and deflections.

To apply the conservation of energy, firstly, infinitesimally small control volume should be defined as $dxdydz$. In this control volume, only thermal energy need is considered. Considering a homogenous stagnant medium and temperature distribution, $T(x, y, z)$, is expressed in Cartesian coordinates. The conduction heat rates which are perpendicular to each of the control surfaces at the $x-, y-$ & $z-$coordinate locations are indicated by the terms q_x, q_y, q_z respectively. The conduction heat rates at the opposite surfaces can then be expressed by a Taylor Series expansion where higher-order terms will be neglected to keep things as simple as possible,

$$q_{x+dx} = q_x + \frac{\delta q_x}{\delta x}\delta x \tag{6}$$

$$q_{y+dy} = q_y + \frac{\delta q_y}{\delta y}\delta y \tag{7}$$

$$q_{z+dz} = q_z + \frac{\delta q_z}{\delta z}\delta z \tag{8}$$

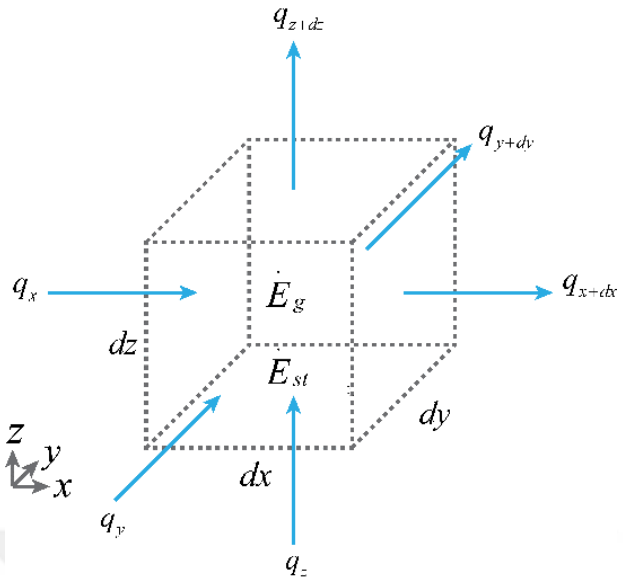

Figure 16. Differential control volume, dx-dy-dz, for conduction analysis in Cartesian Coordinates

In the control volume, there may be an energy source that can be associated with the rate of thermal energy generation. This term can be represented as;

$$\dot{E}_g = \dot{q}dxdydz \tag{9}$$

where $\dot{q}$ is the rate at which energy is generated per unit volume of the medium W/m^3.

In a condition where the material is not experiencing a change in phase, latent energy effects are not concerned, and the energy storage term may be expressed as;

$$\dot{E}_{st} = \rho c_p \frac{\delta T}{\delta t} dxdydz \tag{10}$$

where $\rho c_p \frac{\delta T}{\delta t}$ is the time rate of change of the sensible (thermal) energy of the medium per unit volume.

It should be mentioned that $\dot{E}_g$ and $\dot{E}_{st}$ expressions are representing different physical processes. $\dot{E}_g$ term is a manifestation of energy conversion in which the end product is thermal energy generated from chemical, electrical, or nuclear energy. On

the other hand, $\dot{E}_{st}$ term represents how the matter stores much rate of change of thermal energy.

By the *Fourier Laws of Heat Conduction*, conduction heat rates in isotropic material in which material properties act the same in all the directions may be evaluated.

$$q_x = -kdydz\frac{\delta T}{\delta x} \tag{11}$$

$$q_y = -kdxdz\frac{\delta T}{\delta y} \tag{12}$$

$$q_x = -kdxdy\frac{\delta T}{\delta z} \tag{13}$$

Thereby the appropriate control surface area each heat flux component has been multiplied to obtain the heat transfer rate. In these equations, k is representing the thermal conductivity of the material.

By the rate equations, the general form of the conservation of energy requirement is

$$\dot{E}_{in} + \dot{E}_g - \dot{E}_{out} = \dot{E}_{st} \tag{14}$$

After substituting the heat generation, heat storage, and heat conduction terms and dividing out the dimensions of the control volume (dx, dy, dz), the following expression is obtained

$$\frac{\delta}{\delta x}\left(k\frac{\delta T}{\delta x}\right) + \frac{\delta}{\delta y}\left(k\frac{\delta T}{\delta y}\right) + \frac{\delta}{\delta z}\left(k\frac{\delta T}{\delta z}\right) + \dot{q} = \rho c_p\frac{\delta T}{\delta x} \tag{15}$$

This equation is often referred to as the *Heat Diffusion Equation*, provides the essential tool for heat conduction analysis. From its solution, temperature distribution $T(x, y, z)$ can be obtained. This equation states that at any point in the medium, the rate of change of thermal energy stored within the volume should be equal to the net rate of energy transfer by conduction into a volume plus the volumetric rate of thermal energy generation.

Under steady-state conditions, there can be no change in the amount of energy storage. So, the storage component can be neglected, and the equation takes the form;

$$\frac{\delta}{\delta x}\left(k\frac{\delta T}{\delta x}\right)+\frac{\delta}{\delta y}\left(k\frac{\delta T}{\delta y}\right)+\frac{\delta}{\delta z}\left(k\frac{\delta T}{\delta z}\right)+\dot{q}=0 \quad (16)$$

Moreover, if the heat transfer is one-dimensional, the other dimensions can be neglected, and the equation reduces to

$$\frac{\delta}{\delta x}\left(k\frac{\delta T}{\delta x}\right)+\dot{q}=0 \quad (17)$$

In this study, a one-dimensional heat diffusion equation under steady-state conditions will be used. So, the above equation is the equation that will be improved from now on.

In equation (17), generated energy, $\dot{q}$, will come from the Joule Heating. As explained in the previous section, the heat generated by the passing current can be found as;

$$P=IV=I^2R=\frac{V^2}{R} \quad (18)$$

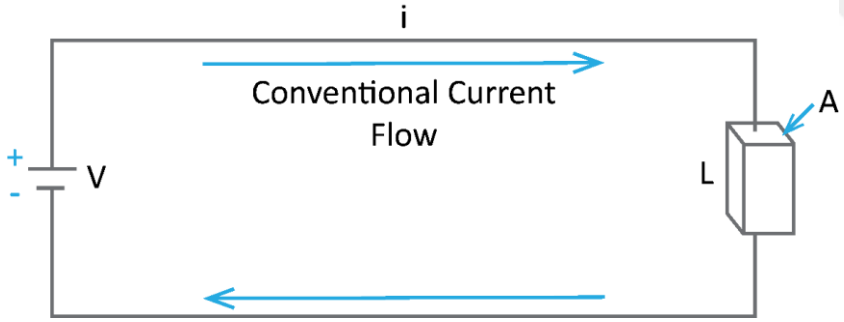

Figure 17. Heating a beam by applying a voltage difference

In a one-dimensional system, $\dot{q}$ will be equal to the P/Ax. Considering, in the dimension of $x-direction$ as length or L, it can be found as

$$\dot{q}=\frac{P}{AL}=\frac{I^2R}{AL} \quad (19)$$

In the electricity basics section, it is found that the resistance of a beam is equal to

$$R=\frac{\rho L}{A} \quad (20)$$

Adding this expression to the power generation equation;

$$\dot{q} = \frac{P}{AL} = \frac{I^2 \frac{\rho L}{A}}{AL} = \frac{I^2 \rho}{A^2} = J^2 \rho \tag{21}$$

Where J is the *current density of the control volume*. Now the final form of the general heat equation can be written as;

$$\frac{\delta}{\delta x}\left(k \frac{\delta T}{\delta x}\right) + J^2 \rho = 0 \tag{22}$$

By solving this equation, the temperature distribution can be obtained.

Since the heat diffusion equation has been obtained, let's apply a known voltage to the system. To find current density concerning the voltage, the first step should be considering the electricity basics. Let's open up the current expression as;

$$I = \frac{V}{R} = \frac{AV}{\rho L} \tag{23}$$

It is known that the current density is $J = {}^{I}/_{A}$. So, the heat diffusion equation can be found as;

$$\frac{\delta}{\delta x}\left(k \frac{\delta T}{\delta x}\right) + \left(\frac{I}{A}\right)^2 \rho = 0 \tag{24}$$

By adding the current definition, the following expression can be found;

$$\frac{\delta}{\delta x}\left(k \frac{\delta T}{\delta x}\right) + \left(\frac{AV}{\rho L}\frac{1}{A}\right)^2 \rho = 0 \rightarrow \frac{\delta}{\delta x}\left(k \frac{\delta T}{\delta x}\right) + \left(\frac{V}{\rho L}\right)^2 \rho = 0 \tag{25}$$

Before solving the equation, simplifying should be made. By taking temperature-dependent parts to the left-hand side and $x - dimension$ dependent parts to the right-hand side, the equation can be rearranged as;

$$\delta^2 T = -\left(\frac{V^2}{\rho L^2 k}\right) \delta x^2 \tag{26}$$

By taking the integral of both sides two times as,

$$\iint \delta^2 T = \iint -\left(\frac{V^2}{\rho L^2 k}\right) \delta x^2 \tag{27}$$

The temperature distribution of the system can be obtained as,

$$T(x) = \left(\frac{V^2}{\rho L^2 k}\right) \frac{x^2}{2} + c_1 x + c_2 \tag{28}$$

$c_1$and c_2 can be found from the boundary conditions of the system. For example, at the start and end of the system, the temperature should be T_0 or, in other words, room temperature. By putting these values, constant parameters can be found.

These equations are valid when the resistivity of the material and the thermal conductivity of the material are assumed to be constant at any temperature or independent of temperature. When, for example, resistivity changes with the different temperature approaches should be tried. However, putting a complex temperature-dependent term in this integral makes the solution very difficult to find. In this calculation, it is assumed that boundary conditions are $T_0 = 293.15\ K$ at $x = 0$ and $x = 2L$. When these boundary conditions are applied to the temperature distribution equation, constants c_1 & c_2 can be found as follows;

$$c_1 = \frac{V^2}{4L\rho k}\ \&\ c_2 = T_0 \tag{29}$$

By putting these constant values to the temperature distribution equation, the following final expressions can be obtained;

$$T(x) = -\frac{V^2}{4L^2\rho k}\left(\frac{x^2}{2} - Lx\right) + T_0 \tag{30}$$

Now, it is essential to find the average temperature and maximum temperature of the system. The average temperature is essential to compare the results of the analytical model and finite element analysis. The maximum temperature is critical to see if the system passes the temperature limit for the material used. The average temperature equation can be found by;

$$\Delta T_{ave} = \frac{1}{2L}\int_0^{2L} T(x) - T_0 dx \tag{31}$$

By putting the temperature distribution equation into this integral, average temperature expression takes the following form;

$$T_{ave} = \frac{V^2}{12\rho k} + T_0 \tag{32}$$

In V-Type actuators, because of the symmetry, the maximum temperature is on the shuttle of the system if only boundary conditions are on $x = 0$ & $x = 2L$. So, by using the temperature distribution equation, the maximum temperature of the system can be found by the following equation;

$$T_{max}(L) = \frac{V^2}{8\rho k} + T_0 \tag{33}$$

2.1.1.2. Thermal Expansion

When the temperature distribution of the system obtained, the displacement at the tip of the beam in the y-direction and the reaction force in the x-direction, due to an average temperature increase ΔT along the beam, can be found by calculating the stiffness matrix of the system.

The stiffness can be found by $stiffness = k = \frac{F}{\delta} = \frac{Force}{Displacement}$. In the $\zeta - direction$, we will find the axial stiffness. As defined, axial stiffness can be found by

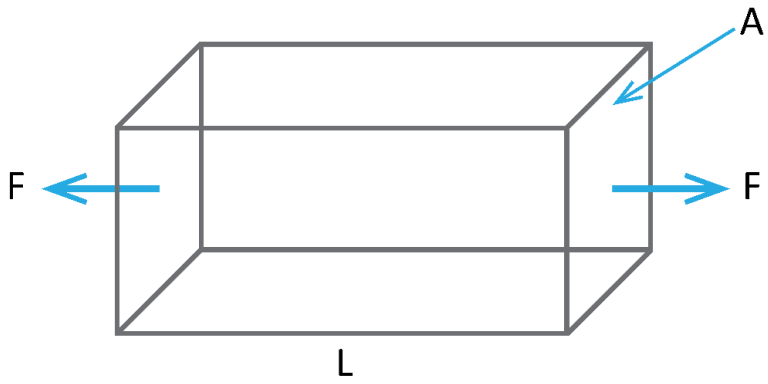

Figure 18. Visual representation of how Axial Stress created

$$k = \frac{AE}{L} \tag{34}$$

Another stiffness value is radial stiffness. In our case, the system's right end is guided, and the end is a fixed position with a force and a moment in the right tip. Let

the end reactions due to settlement at the right end be F and M, as shown in Figure 19. The $M/_{EI}$ diagrams of the beam are also shown in the same figure.

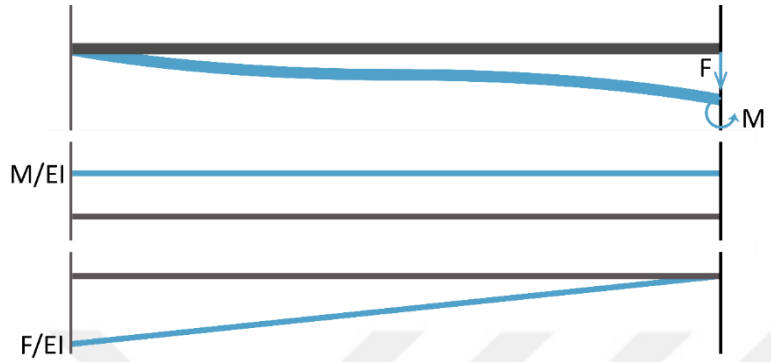

Figure 19. Visual representation of moment and force reactions on the beam

After sketching the visual representation, let's apply the first moment area theorem, which states that the change in slope between any two sections on the elastic curve of a beam is equal to the area under the $M/_{EI}$ diagram between those sections between the left and right ends of the beam.

$$\Delta\theta = \frac{L}{2}\frac{M}{EI} - \frac{FL}{EI}L = 0 \tag{35}$$

Or

$$M = \frac{FL}{2} \tag{36}$$

After finding the moment force relation, now let's apply the second area theorem between right and left ends. The second area theorem is the tangential deviation of any point A on the elastic curve of a beam from a tangent drawn at any other point on the curve is equal to the static moment about point A of the area under $M/_{EI}$ diagram between those points.

$$t = \frac{M}{EI}L\frac{L}{2} - \frac{1}{2}\frac{FL}{EI}L\frac{2L}{3} \rightarrow t = \Delta = \frac{ML^2}{2EI} - \frac{FL^3}{3EI} \tag{37}$$

Solving the results of first and second-moment area theorems, the following expressions can be found as;

$$M = \frac{6EI\Delta}{L^2} \;\&\; F = \frac{12EI\Delta}{L^3} \tag{38}$$

Now, the stiffness value can be found as

$$k = \frac{F}{\Delta} = \frac{12EI}{L^3} \tag{39}$$

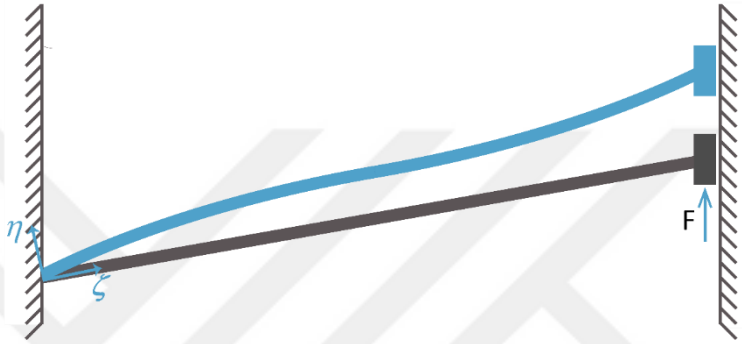

Figure 20. Visual representation of how Radial Stress created

The inertia in the $\eta - direction$ of the system can be found by the below equation.

$$I = \frac{1}{12} w^3 h \tag{40}$$

Force generated by the thermal expansion can be found by the same rule as well. Expanded length because of the thermal expansion can be found by thermal expansion coefficient as;

$$l' = \alpha \Delta T l_0 \tag{41}$$

By the found axial stiffness value, we can find the generated force as;

$$F_{thermal} = l'k = \alpha \Delta T l_0 \frac{AE}{l_0} = \alpha \Delta T AE \tag{42}$$

Since there is no force resulting from the expansion, force is equal to zero at $\eta - axis$.

In the stiffness matrix, other elements, k_{12} and k_{21} elements are equal to zero since there is nothing to coincide between the two axes since they are independent of each

other. To obtain the matrix in the global frame, $x-y\ frame$, we first compute the elastic stiffness matrix in the local reference frame. The system of equations governing the structural behavior of the beam, when subjected to the average increase in temperature ΔT, is

$$\begin{bmatrix} \frac{EA}{L} & 0 \\ 0 & \frac{12EI}{L^3} \end{bmatrix} \begin{bmatrix} U_\zeta^A \\ U_\eta^A \end{bmatrix} = \begin{bmatrix} \alpha \Delta T EA \\ 0 \end{bmatrix} + \begin{bmatrix} R_\zeta^A \\ R_\eta^A \end{bmatrix} \tag{43}$$

In order to apply the boundary conditions in the global reference frame x-y, the system is transformed through the rotation matrix,

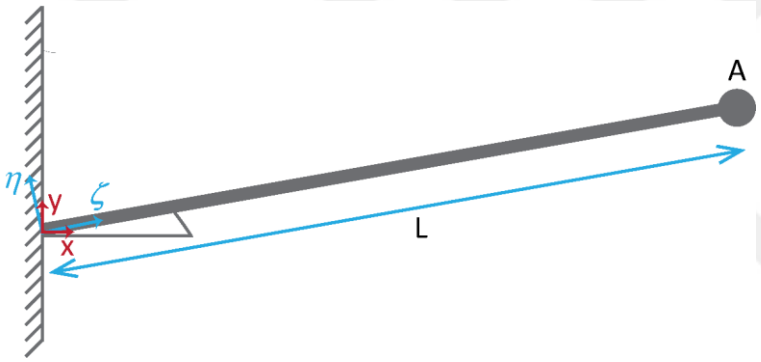

Figure 21. Global (Red) and Local (Blue) coordinates of the system

$$R = \begin{bmatrix} \cos\theta & -\sin\theta \\ \sin\theta & \cos\theta \end{bmatrix} \tag{44}$$

The matrix R is relating the local degrees of freedom to the global ones.

Before going forward, two concepts should be mentioned. First is the inverse transformation. The inverse transformation is the transformation of the new system to the old system. For the given old coordinates, the inverse transformation can be found as

$$A^t A = 1 \tag{45}$$

In other words, the matrix A^T is the inverse of the matrix A.

$$A^T = A^{-1} \tag{46}$$

The next concept is the transformation of an operator. In a cartesian coordinate system S, a matrix operator A acts on the vector x, producing the vector y. In a rotated coordinate system S', the vectors x and y are transformed as

$$x' = Rx \;\&\; y' = Ry \tag{47}$$

Where R is the rotation matrix. By using the previous equations, the following equations can be found;

$$y' = RAx = (RAR^{-1})x' \tag{48}$$

In the S' frame, the relationship between the two vectors takes the form

$$y' = A'x' \tag{49}$$

and also, it can be seen that the operator A transforms to

$$A' = RAR^{-1} \tag{50}$$

So, the transformation matrix of the $\zeta - \eta$ coordinate system transforms into the $x - y$ coordinate system as follows,

$$B_{xy} = R^{-1}B_{\zeta\eta}R \tag{51}$$

Now, the system of equations transforms into the x-y frame as;

$$\begin{bmatrix} c^2\dfrac{EA}{L} + s^2\dfrac{12EI}{L^3} & cs\left(\dfrac{EA}{L} - \dfrac{12EI}{L^3}\right) \\ cs\left(\dfrac{EA}{L} - \dfrac{12EI}{L^3}\right) & s^2\dfrac{EA}{L} + c^2\dfrac{12EI}{L^3} \end{bmatrix} \begin{bmatrix} U_x^A \\ U_y^A \end{bmatrix} = \begin{bmatrix} \alpha\Delta TEAc \\ \alpha\Delta TEAs \end{bmatrix} + \begin{bmatrix} R_x^A \\ R_y^A \end{bmatrix} \tag{52}$$

In equation (52), c and s are representing $\cos\theta$ and $\sin\theta$, respectively. By applying the following boundary conditions, $U_x^A = 0, R_x^A \neq 0, U_y^A \neq 0, R_y^A = 0$ where R_x^A and R_y^A are reaction forces of the node in the x and y directions, respectively. Substitution into the governing system of equations yields

$$\begin{bmatrix} c^2\frac{EA}{L}+s^2\frac{12EI}{L^3} & cs\left(\frac{EA}{L}-\frac{12EI}{L^3}\right) \\ cs\left(\frac{EA}{L}-\frac{12EI}{L^3}\right) & s^2\frac{EA}{L}+c^2\frac{12EI}{L^3} \end{bmatrix}\begin{bmatrix} 0 \\ U_y^A \end{bmatrix}=\begin{bmatrix} \alpha\Delta TEAc \\ \alpha\Delta TEAs \end{bmatrix}+\begin{bmatrix} R_x^A \\ 0 \end{bmatrix} \quad (53)$$

The second equation in the above equation system gives the displacement of the node in the y-direction due to an average increase in temperature ΔT along the beam. In contrast, the first equation provides the reaction force in the x-direction.

$$U^{\Delta T}=U_y^A=\alpha\Delta Tl\frac{\sin\theta}{\sin^2\theta+\frac{12\mathrm{I}}{\mathrm{AL}^2}\cos^2\theta}=\alpha\Delta Tl\frac{\sin\theta}{\sin^2\theta+\frac{\cos^2\theta}{\psi}} \quad (54)$$

$$\begin{aligned} R_x^{\Delta T}=R_x^A&=-\alpha\Delta TEA\frac{\cos\theta}{\frac{\mathrm{AL}^2}{12\mathrm{I}}\sin^2\theta+\cos^2\theta} \\ &=-\alpha\Delta TEA\frac{\cos\theta}{\psi\sin^2\theta+\cos^2\theta} \end{aligned} \quad (55)$$

Where ψ is defined as axial over bending stiffness ratio and expressed as $\psi=\frac{AL^2}{12I}$.

When a voltage is applied to the anchors, the V-shape actuator beams will exert a force because of the expansion of the beams. The maximum force created is given by;

$$F=\sigma A \quad (56)$$

Because the strain energy is given by $\varepsilon(s)=\alpha T(s)$ and axial stress, σ , with Young's modulus is given by $\sigma=E\varepsilon$. The force developed in the y-direction by the actuator with the length $2L$,

$$F_t=A\sigma=AE\varepsilon=AE\alpha T_{avg}2L\sin\theta \quad (57)$$

The sinus term in the last equation term is because the beams are inclined. To find the force in the y-direction, the sinus term should be added.

For n-many V-shape actuator beams, the total force is;

$$F_t=nA\sigma=nAE\varepsilon=nAE\alpha T_{avg}2L\sin\theta \quad (58)$$

And the total Power of the System will become;

$$P = n \times I \times V \tag{59}$$

2.1.1.2.1. Critical Considerations

It is essential to estimate under what conditions the inclined beams might buckle. Buckling occurs when the internal force exceeds the critical buckling force. Buckling occurs in the plane where the moment of inertia is minimum. It can be orthogonal to or parallel to the substrate depending on the beam dimensions. The critical force for buckling can then be written as

$$P_{cr} = \pi^2 \frac{E I_{min}}{L^2} \tag{60}$$

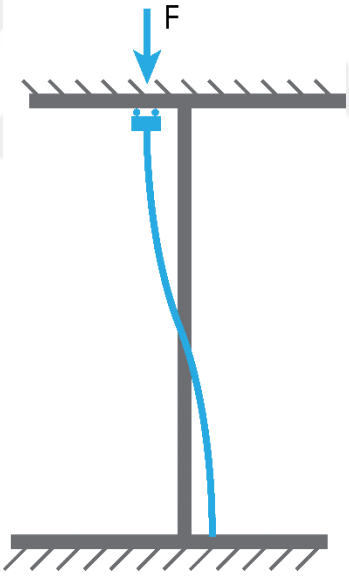

Figure 22. Buckling mode of the system

2.1.2 **Analytical Modeling of MEMS Thermal Actuators**

In order to see if the derived mathematical model is right, the Office Excel model is prepared. In this model, the following parameters can be changed by the scroll bar,

- Length
- Width
- Height
- Tilt Height
- Shuttle Width
- Number of Actuators
- Voltage

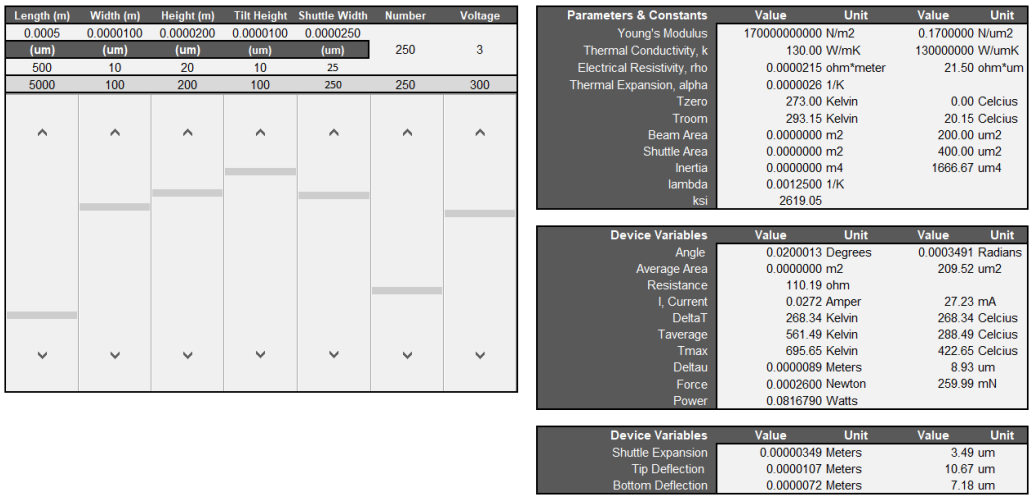

Length (m)	Width (m)	Height (m)	Tilt Height	Shuttle Width	Number	Voltage
0.0005	0.0000100	0.0000200	0.0000100	0.0000250		
(um)	(um)	(um)	(um)	(um)	250	3
500	10	20	10	25		
5000	100	200	100	250	250	300

Parameters & Constants	Value	Unit	Value	Unit
Young's Modulus	170000000000	N/m2	0.1700000	N/um2
Thermal Conductivity, k	130.00	W/mK	130000000	W/umK
Electrical Resistivity, rho	0.0000215	ohm*meter	21.50	ohm*um
Thermal Expansion, alpha	0.0000026	1/K		
Tzero	273.00	Kelvin	0.00	Celcius
Troom	293.15	Kelvin	20.15	Celcius
Beam Area	0.0000000	m2	200.00	um2
Shuttle Area	0.0000000	m2	400.00	um2
Inertia	0.0000000	m4	1666.67	um4
lambda	0.0012500	1/K		
ksi	2619.05			

Device Variables	Value	Unit	Value	Unit
Angle	0.0200013	Degrees	0.0003491	Radians
Average Area	0.0000000	m2	209.52	um2
Resistance	110.19	ohm		
I, Current	0.0272	Amper	27.23	mA
DeltaT	268.34	Kelvin	268.34	Celcius
Taverage	561.49	Kelvin	288.49	Celcius
Tmax	695.65	Kelvin	422.65	Celcius
Deltau	0.0000089	Meters	8.93	um
Force	0.0002600	Newton	259.99	mN
Power	0.0816790	Watts		

Device Variables	Value	Unit	Value	Unit
Shuttle Expansion	0.00000349	Meters	3.49	um
Tip Deflection	0.0000107	Meters	10.67	um
Bottom Deflection	0.0000072	Meters	7.18	um

Figure 23. First Part of the Actuator Excel Model, Variables and Material Properties

In Figure 23, previously mentioned variables can be seen on the left. On the right upper part, Young's Modulus, thermal conductivity, electrical resistivity, thermal expansion coefficient, and room temperature are defined. Beam area, shuttle area, inertia, lambda, and ksi values are derived from the variables.

On the right middle part, angle, average area, resistance, current, average temperature change, average temperature, maximum temperature, deflection, force,

and power are calculated. At last, on the right bottom part, shuttle expansion, shuttle tip deflection, and shuttle bottom deflection are calculated.

On the right part of the calculation part, the plotting of the v-type actuator took place. On the top, Total Resistance, total current, and maximum temperature control have been placed. Below those, coordinates are calculated for four cases, unheated, average deflection, tip deflection, and bottom deflection.

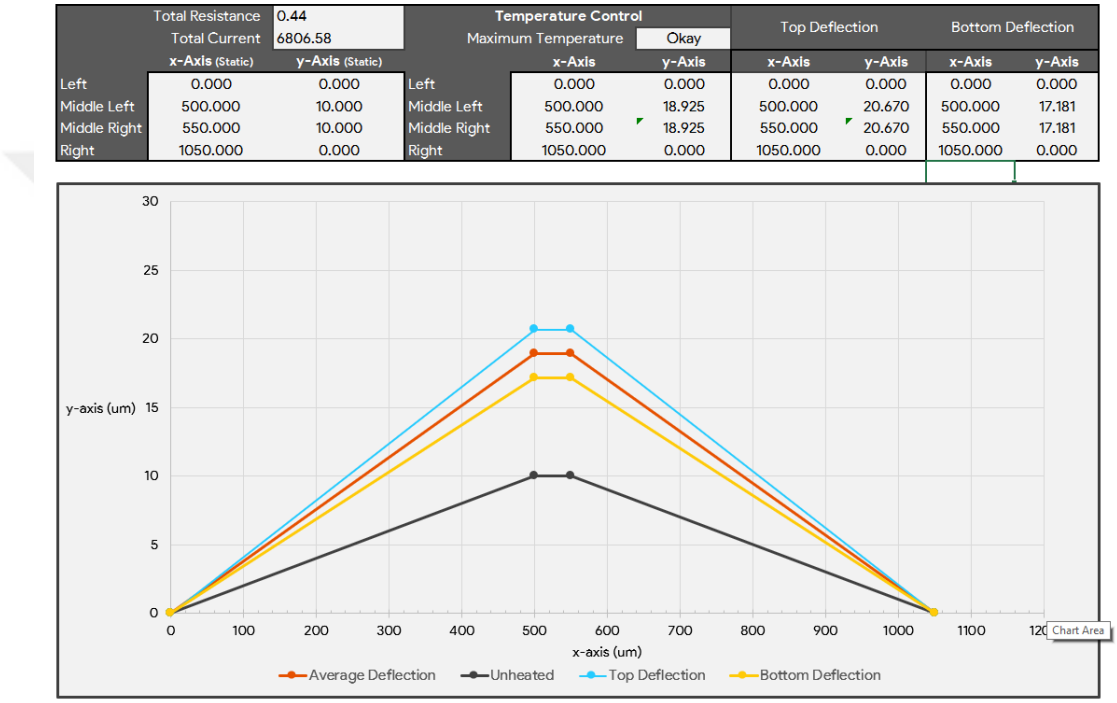

	Total Resistance	0.44	Temperature Control		Top Deflection		Bottom Deflection	
	Total Current	6806.58	Maximum Temperature	Okay				
	x-Axis (Static)	y-Axis (Static)		x-Axis	y-Axis	x-Axis	y-Axis	x-Axis	y-Axis
Left	0.000	0.000	Left	0.000	0.000	0.000	0.000	0.000	0.000
Middle Left	500.000	10.000	Middle Left	500.000	18.925	500.000	20.670	500.000	17.181
Middle Right	550.000	10.000	Middle Right	550.000	18.925	550.000	20.670	550.000	17.181
Right	1050.000	0.000	Right	1050.000	0.000	1050.000	0.000	1050.000	0.000

Figure 24. Second Part of the Actuator Excel Model, Actuator Positions and Actuator Plot

Below this plotting part, six graphs have been plotted; Voltage vs. Maximum Temperature, Average Temperature, Current, Shuttle Position, Force, and Power. It is pretty informative to see all of the results in the same place to see how the overall model is behaving.

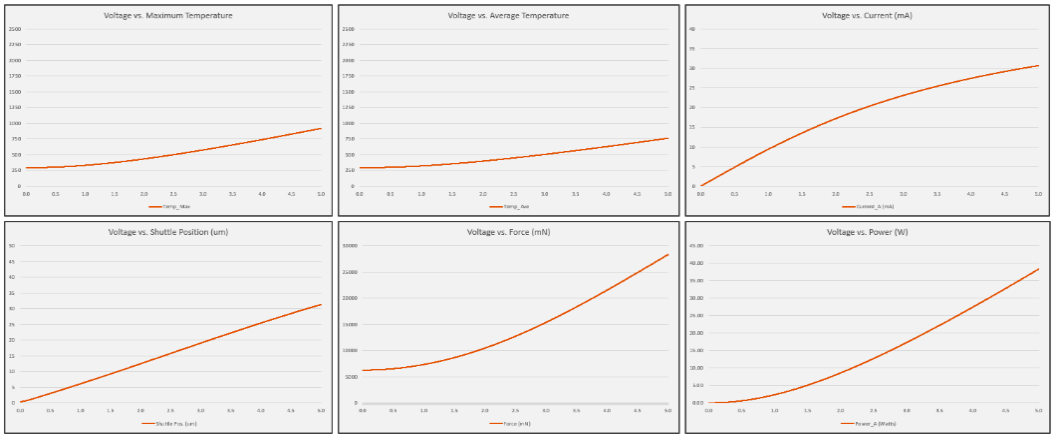

Figure 25. Third Part of the Actuator Excel Model, Voltage vs. Max. Temperature, Avg. Temperature, Current, Shuttle Position, Force and Power graphs

2.1.3 **Finite Element Modeling (FEM) Simulations of MEMS Thermal Actuators**

In this research, finite element analysis is performed in COMSOL Multiphysics 5.2. Four physics have been used in this study, Solid Mechanics, Heat Transfer in Solids, Electric Currents and Multiphysics such as Thermal Expansion, Electromagnetic Heat Source, Boundary Electromagnetic Heat Source, and two Temperature Couplings. All of these physics have been used simultaneously.

Both stationary and time-dependent results have been obtained from the analysis. As a material single-crystal, isotropic silicon with a resistivity value of $0.00015\ \Omega.m$ is defined. In the analysis, Physics controlled mesh is defined with Extra Fine mesh size.

2.1.3.1. Electro-Thermo-Mechanical Simulations of the MEMS Thermal Actuators

Firstly, Solid Mechanics boundary conditions are defined. “Fixed Constrained” boundary condition is selected and defined for both ends of the V-type thermal actuator. Then, in Heat Transfer in Solids physics, the “Temperature” boundary

condition is defined in both ends of the actuator as $293.15\ K$. Then, in Electric Current's physic, “Ground” and “Electric Potential” boundary conditions are defined. The ground is defined on the left-hand side end of the actuator, and Electric Potential is defined on the right-hand side end of the actuator. Lastly, in the Multiphysics section, Thermal Expansion set up as a heat transfer interface defined as Heat Transfer in Solids physic and Structure interface is defined as Solid Mechanics physic. Strain Reference Temperature is expressed as $293.15\ K$. In Electromagnetic Heat Source, Electromagnetic interface is defined as Electric Currents physics, and Heat transfer Interface is defined as Heat Transfer in Solids. In Boundary Electromagnetic Heat Source, both interfaces are defined as on Electromagnetic Heat Source. Finally, both Temperature Couplings are defined as Heat Transfer in Solids to Solid Mechanics and Electric Currents.

Electric Potential is the only variable when all the geometrical dimensions are neglected. So, all the analyses that are performed will have variable voltage or variable dimensions.

2.1.3.2. Electro-Thermo-Mechanical Simulation Results of the MEMS Thermal Actuators

The first analysis was for different voltage values with $300\ um$ length, $10\ um$ widths, and $27.5\ um$ depth. The results of this analysis has been represented in the Table 1.

Table 1. Analysis Results of one thermal actuator with 300 um length, 10 um width, 27.5um depth, and varying voltage

Length (um)	Voltage (V)	Deflection (um)	Max. Temp. (K)
300	1,00	0,055	297,54
300	2,00	0,22	310,71
300	3,00	0,49	332,66
300	4,00	0,88	363,38
300	5,00	1,37	402,89
300	6,00	1,98	451,18
300	7,00	2,69	508,24
300	8,00	3,51	574,09
300	9,00	4,45	648,71

It can be seen that by increasing the voltage, deflection and maximum temperature values are also increasing as expected. To see the effect, the following graphs have been plotted.

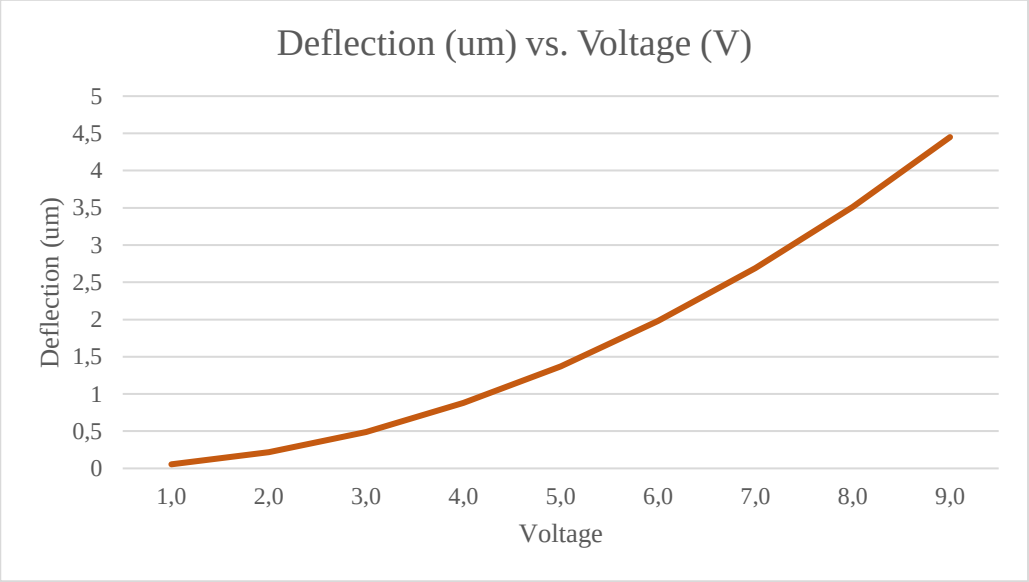

Figure 26. Deflection vs. Voltage plot for 300um length 10um width and 27,5 um depth

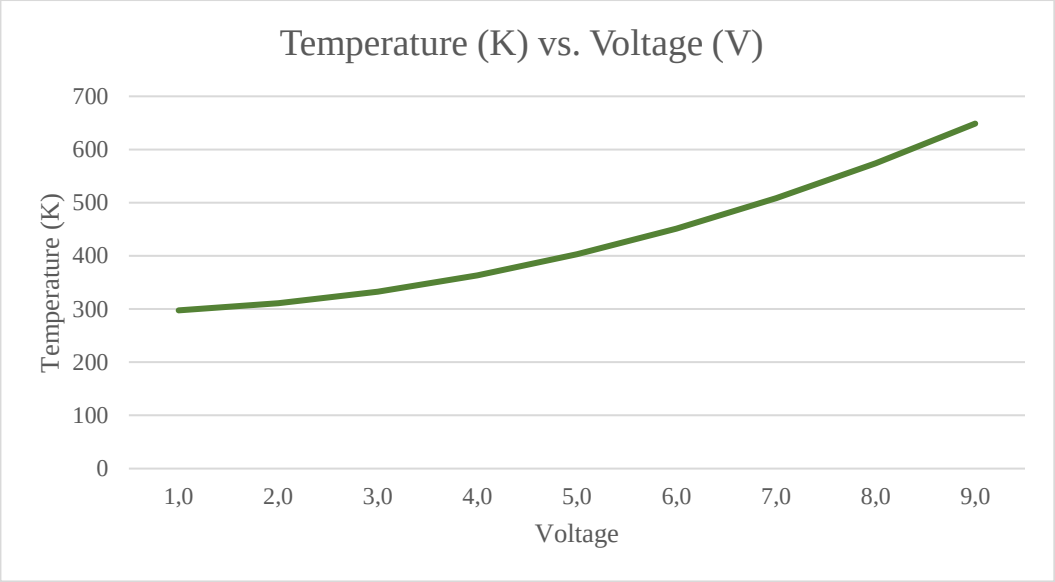

Figure 27. Maximum Temperature vs. Voltage plot for 300um length, 10um width, and 27,5um depth

When the derived equations are considered, changing the length of the actuator changes only the deflection of the beam, not the maximum temperature of the actuator. So, it is expected to get the same temperature results for any of the lengths. To see that, the same analysis is run with length values of $400\ um$ and $500\ um$. The data and plots of these analyses are;

Table 2. Analysis Results of one thermal actuator with 400 & 500 um length, 10um width, 27,5um depth, and varying voltage

Length (um)	Voltage (V)	Deflection (um)	Max. Temp. (K)
400	1,0	0,10	297,51
400	2,0	0,38	310,60
400	3,0	0,86	332,41
400	4,0	1,53	362,95
400	5,0	2,39	402,22
400	6,0	3,44	450,21
400	7,0	4,68	506,92
400	8,0	6,11	572,36
400	9,0	7,73	646,52

Table 3. (continued) Analysis Results of one thermal actuator with 400 & 500 um length, 10um width, 27,5um depth, and varying voltage

Length (um)	Voltage (V)	Deflection (um)	Max. Temp. (K)
500	1,0	0,15	297,50
500	2,0	0,59	310,53
500	3,0	1,32	332,26
500	4,0	2,35	362,69
500	5,0	3,68	401,80
500	6,0	5,30	449,61
500	7,0	7,21	506,10
500	8,0	9,42	571,29
500	9,0	11,92	645,17

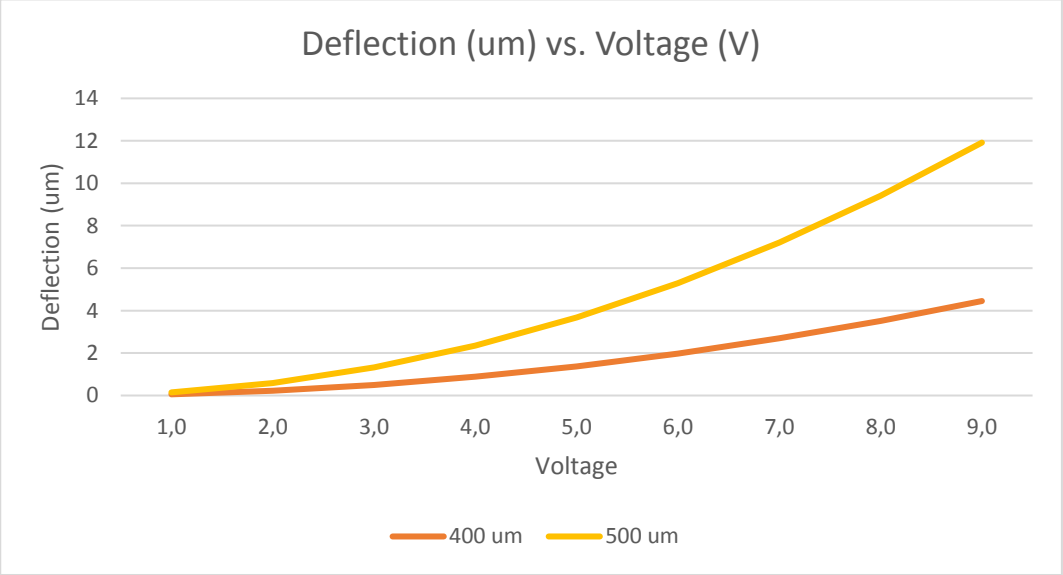

Figure 28. Deflection vs. Voltage plot for 400 & 500um length 10um width and 27,5 um depth

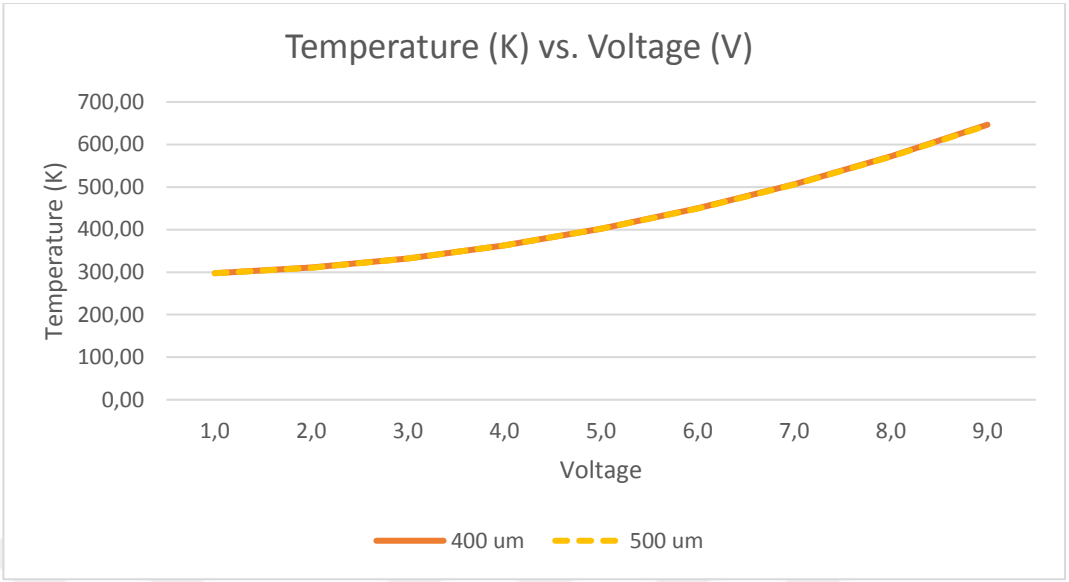

Figure 29. Maximum Temperature vs. Voltage plot for 400 & 500 um length 10um width and 27,5 um depth

As seen, what is expected is proved to be true. For changing length values, the maximum temperature of the system remains the same. However, because of the geometry, as the length increases, the deflection of the system also increases.

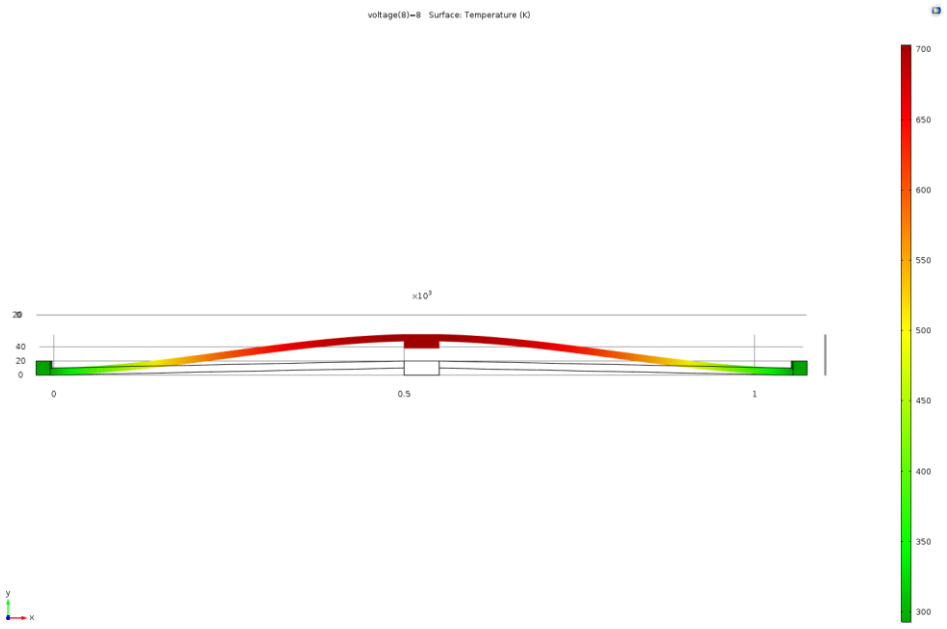

Figure 30. Finite element analysis results for deflection (magnified) and temperature for 500um v-type actuator under 8V

When the mathematical model programmed in Office Excel and finite element analysis on Comsol compared for $500\ \mu m$ length, it has been seen that the values coincide pretty well. For deflection, a maximum 5.92% error is obtained, and for maximum temperature, a maximum 0.67% error is obtained. The results are tabulated in Table 4.

Table 4. Mathematical model and Finite Element Analysis result comparison for 500 um actuators

500um						
	Deflection (um)			Av. Temp. (K)		
Voltage	Model	Comsol	Error (%)	Model	Comsol	Error (%)
1	0,14	0,15	5,92	299,41	297,39	0,67
2	0,56	0,59	5,91	310,09	310,12	0,01
3	1,25	1,32	5,90	331,46	331,34	0,04
4	2,22	2,35	5,91	361,38	361,04	0,09
5	3,47	3,68	5,91	399,84	399,22	0,16
6	5,00	5,30	5,90	446,85	445,89	0,21
7	6,81	7,21	5,90	502,40	501,05	0,27
8	8,89	9,42	5,90	566,50	564,69	0,32
9	11,25	11,92	5,90	639,15	636,82	0,36

2.1.3.3. Packed Actuators

When more than one V-shape actuators are combined to generate more force with the same amount of deflection, one should consider the effect of thermal expansion of the shuttle since the temperature values can exceed $400 - 500\ Kelvin$ in the shuttle. As the one designs the shuttle longer, the expansion will be more significant, and the deflection on the bottom of the actuator pack will elongate less than the actuators on the top of the pack.

A finite element analysis had been performed to see this effect. Below, a finite element analysis results are presented to see this behavior. First, let's take a look at the V-Shaped actuator with $500\ um$ length, $10\ um$ widths, and $27{,}5\ um$ height. If we apply $8V$ voltage to the system, the following results are obtained;

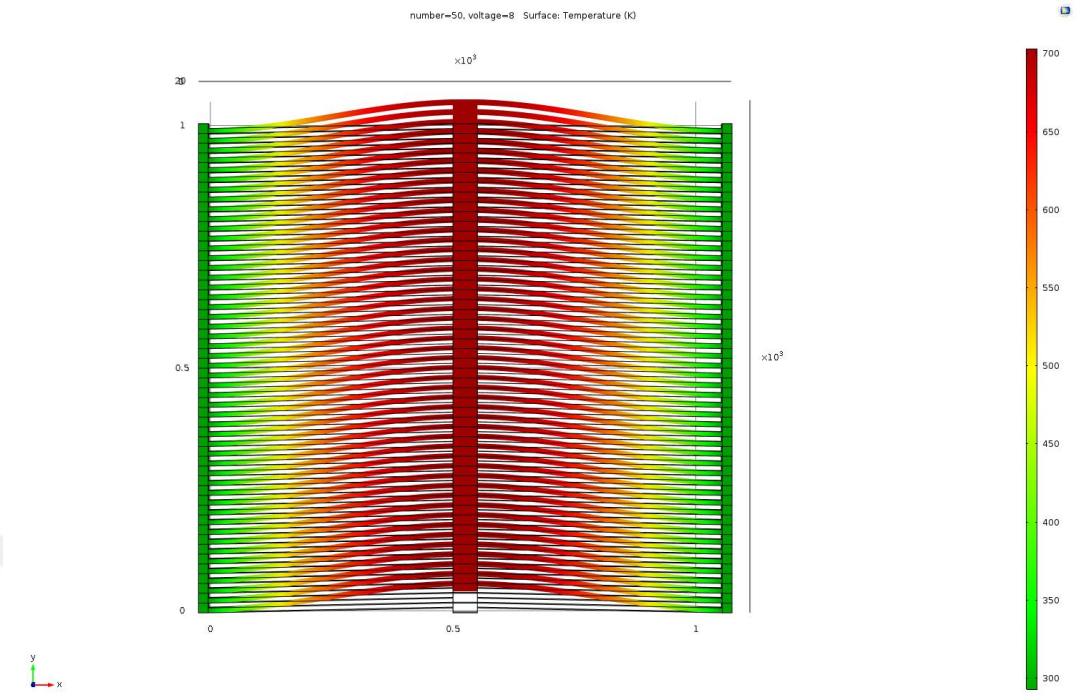

Figure 31. Finite Element Analysis results for deflection (Magnified) and temperature of 50 packed actuators under 8V

Table 5. Analysis Results of one thermal actuator with 500 um length, 10um width, 27.5 um depth, 8V Voltage, and a varying number of actuators

Number of Actuators	Tip Deflection	Bottom Deflection
1	9,44	9,42
25	9,63	9,07
50	9,91	8,79
75	10,18	8,50
100	10,42	8,20
150	10,92	7,63
200	11,40	7,09
250	11,89	6,61

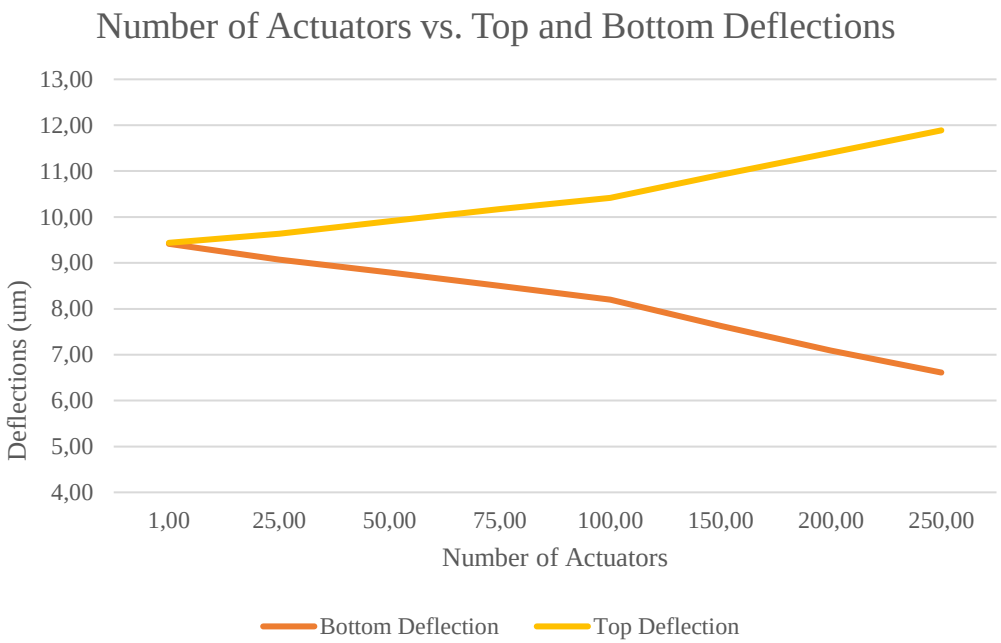

Figure 32. Analysis Plot of actuator pack with varying number of actuators in 8V Voltage and 500um Length

One can see that when the number of actuators increased, the gap between the top and bottom deflection values also increase. This is because of the thermal elongation of the shuttle.

The maximum temperature of the system exceeds 1000 Kelvin between 10V-11V for 500 μm actuator beams, as stated before. To be on the safe side and to decrease the temperature of the system proposed model will work on voltage values that are smaller than 10V.

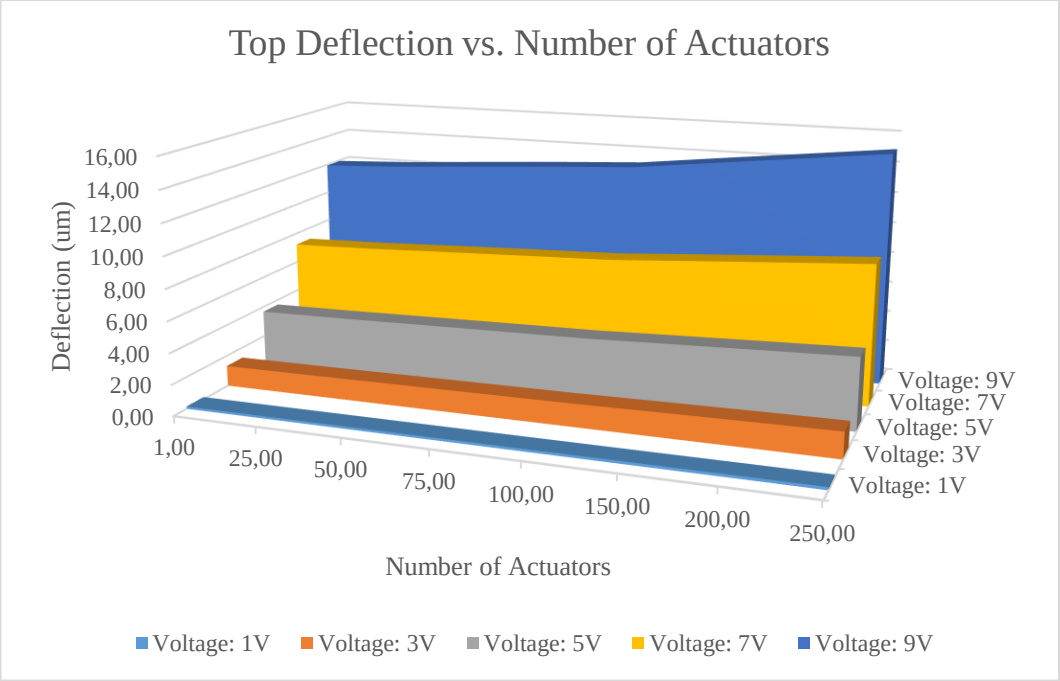

Figure 33. Tip Deflection vs. Number of Actuators Analysis Plot of 500 um variable number of the packed actuator at variable voltage values

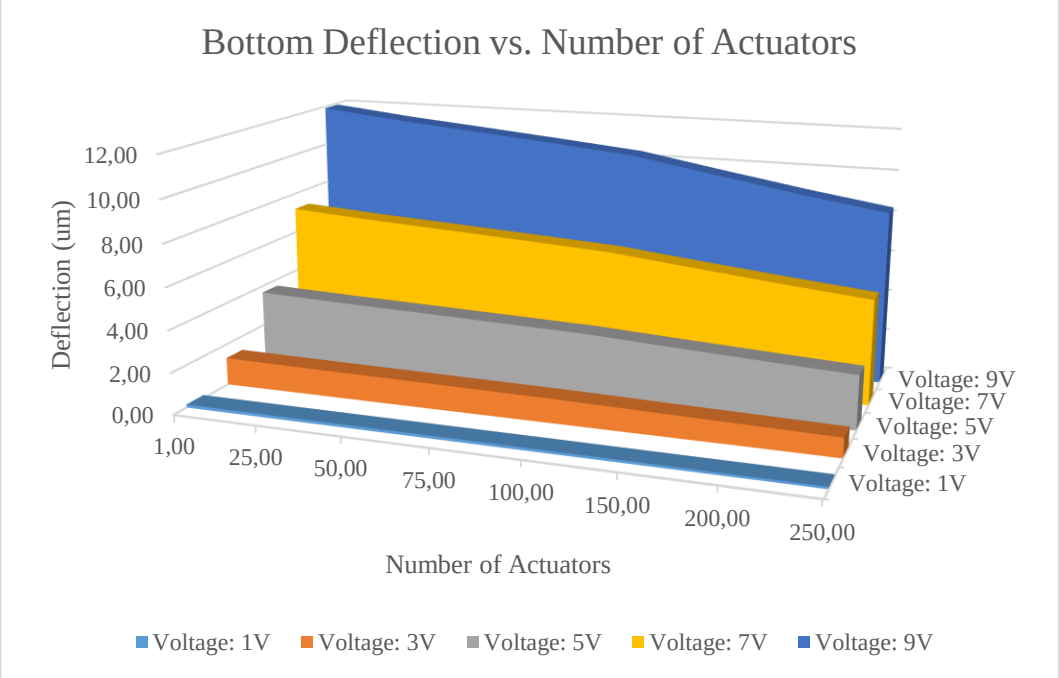

Figure 34. Bottom Deflection vs. Number of Actuators Analysis Plot of 500 um variable number of the packed actuator at variable voltage values

2.1.4 **Effect of Gravity**

The packed actuator system will have a massive shuttle, and it should be analyzed that how much the shuttles drop in the effect of gravity. Using COMSOL, this analysis had been performed. By applying gravity on z-direction, a packed actuator with 150 thermal actuators which have 500 um in length, 5 um in width, and 25 um in height, -0.0025777 um deflection had been calculated in the z-direction, which is 2.5 nanometers. It being safe to assume that shuttle is not moving in z-direction when gravity acts on the system.

2.2. **Design and Modelling of MEMS Force Sensors**

MEMS Resonators have been used extensively in many different areas, as stated in Chapter 1. In this thesis, force sensing will be done through MEMS resonators. To explain the working principles of this resonant based force sensors, firstly, operation principles of MEMS resonators will be represented. Hence, in section 2.2.1, the working principles of MEMS Resonators will be studied in detail. After how resonators work is described, the mechanical design of MEMS resonators will be examined in section 2.2.2. Then, with the FEM analysis results in section 2.2.3, this section will come to an end.

2.2.1 **Operation Principles of MEMS DETF Resonators Used in This Study**

Double-Ended Tuning Fork (DETF) type resonator is used in this thesis to sense how much force has been applied to the specimen. DETF resonators are consist of two thin tines in the structure, and which can move under the effect of electrostatic force mechanically. By the two electrode sets, this electrostatic force has been generated and applied to the tines. These two electrode sets are named as drive electrodes and sense electrodes. They are placed around the tines of DETF. The signal can pass through the electrodes, and vibration in the tines can be created. By optimizing the

signal, vibration can occur in tines' desired operation mode concerning the sensing principles. In this part of this thesis, how the tines move under both capacitive and sensing actuation modes will be examined. Firstly, the mechanical motion of the tines will be examined. After that part, in sections 2.2.1.1 and 2.2.1.2, capacitive actuation and capacitive detection mechanisms of the DETF structure will be described respectively.

In this study, in order to provide stable displacements while the tines are resonating, the tines have additional capacitive plates connected from the middle of the tines. In Figure 35, the illustration of the DETF resonator used in this study can be seen. In that figure, area number 1 is the drive electrodes. Area number 2 is the sense electrodes, and area number 3 is the tines of the DETF structures. Area number 3 is fixed in one end, and the other end is where the force is applied.

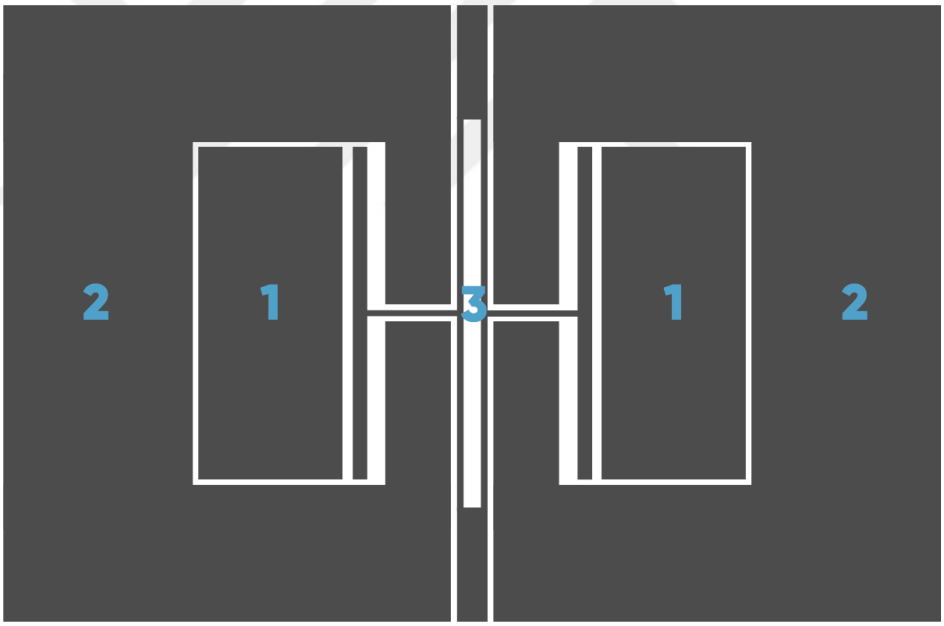

Figure 35. Schematic of the DETF Resonator Structure Used in This Study

The parts of the DETF structure, tines, in this case, can be modeled as a second-order mass-spring-damper system. In Figure 36, the illustration of the model of the tines can be seen.

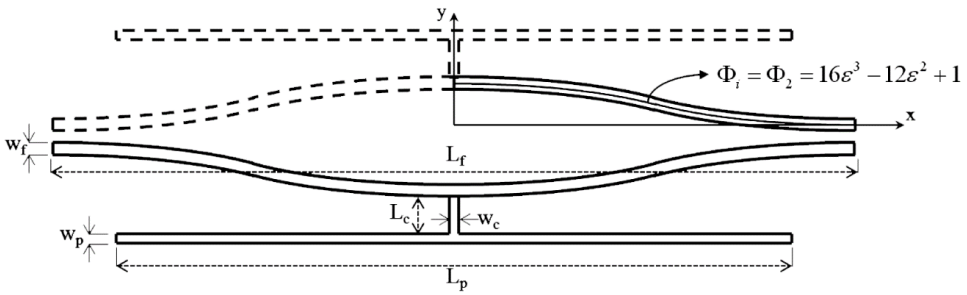

Figure 36. The reference system, geometric variables, and assumed mode shape function throughout the analysis

Equation of motion of the system can be modeled by;

$$m\ddot{x} + b\dot{x} + kx = F \tag{61}$$

In this equation, m is used to denote resonating mass, b is used to denote the damping coefficient of the system, k is used to denote the mechanical spring coefficient in the motion direction, and x is used to denote the displacement of the mass. The transfer function of this system can be found by taking the Laplace transform of the equation of motion. Between the displacement and force, the transfer function can be found as;

$$\frac{X(s)}{F(s)} = \frac{1}{ms^2 + bs + k} \tag{62}$$

From this equation, the undamped and damped natural frequencies and the damping ratio should be found to define the motion of the resonating system. ω_n denotes the undamped natural frequency, ξ denotes the damping ratio and ω_d denotes the undamped natural frequency of this system.

$$\omega_n = \sqrt{\frac{k}{m}} \tag{63}$$

$$\xi = \frac{b}{2\sqrt{km}} \tag{64}$$

$$\omega_d = \omega_n\sqrt{1 - \xi^2} \tag{65}$$

Here, the damping ratio plays a vital role in defining the motion of the system. Because of the damping ratio turns out to be higher than 1 or equal to 1, the system will be overdamped and critically damped, and the system will not be oscillating, which is not desired for this system. In order to keep the system oscillating, the damping ratio should be less than 1. As the damping ratio becomes smaller, it will be easier to create and maintain resonance since the dissipated energy will be lesser.

There is a term to see how underdamped the system is, and it is called the quality factor, illustrated by Q. The quality factor can be found by dividing the resonance frequency by half-power bandwidth. This is happening in the place where the resonance amplitude degrades $3\,dB$ from the peak amplitude. However, for a mechanical system, the quality factor can be calculated by the following equation;

$$Q = \frac{\sqrt{mk}}{b} \tag{66}$$

Where it is assumed that the damping ratio is small. ($\xi < 0.1$)

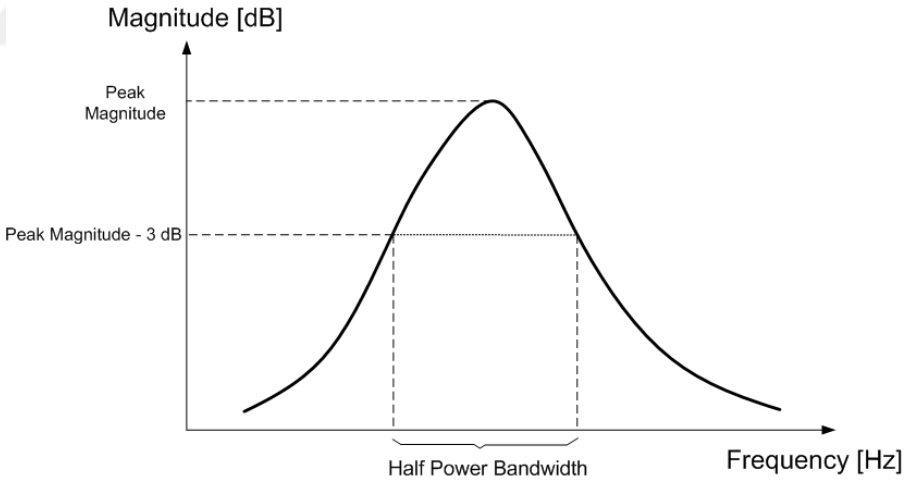

Figure 37. Half-power bandwidth illustration on a typical frequency-response plot

In the case of the double-ended tuning fork, the damped and the undamped natural frequencies have almost the same value in the case of small damping ratio ($\xi < 0.1$) as in most practical cases. In order to simplify the calculations in the future, from now on, the undamped natural frequency formula will be used from this point on. In

the following section, the resonators' trigger mechanism for the resonance will be illustrated.

2.2.1.1. Capacitive Actuation

The capacitive actuation method is used to create the desired motion of the resonator structures. Using the electrostatic forces, this actuation method is used to create a force on the resonator structure thanks to the drive electrodes placed around the resonating mass. The electrostatic forces can be enough to move the tines of the resonator since the structure is micro-sized.

In order to create electrostatic forces, electrostatic energy should have a gradient. This can be showed by

$$F_e = \nabla \mathrm{E} \tag{67}$$

In the above equation, F_e states the electrostatic force and E states the electrostatic energy. Electrostatic energy, E, can be described by;

$$E = \frac{1}{2} C V^2 \tag{68}$$

In this equation, C is used to denote capacitance formed between the drive electrode and the tines, and V is used to denote applied electrical potential between the drive electrodes and the tines. C, the capacitance between the proof mass and the drive electrode can be found by

$$C = \frac{2n\varepsilon A_c}{g} = \frac{2n\varepsilon_0 h(L_0 - x)}{g} \tag{69}$$

In this representation, ε is used to denote the permittivity of the medium in the capacitive gap, A_c is used to denote the capacitive area where the capacitance formed between the proof mass and the drive electrodes, and g is used to denote the capacitive gap between the proof mass and the drive electrodes. While operating, it

is desired to have an in-plane operation mode along only one axis. From now on, the electrostatic force can be expressed as;

$$F_e = \frac{1}{2}\frac{\delta C}{\delta x}V^2 \tag{70}$$

The partial derivative of the capacitance between the drive electrodes and the proof mass should be extracted to express the electrostatic force formula further. After the extraction of the capacitance change concerning the deflection of the tines, the electrostatic force applied on the tines by the drive electrodes can be found as;

$$F_{e,d} = \frac{1}{2}\frac{\delta}{\delta x}\left[\frac{\varepsilon_0 A_c}{g}\right]V^2 \tag{71}$$

$$F_{e,d} = -\frac{n\varepsilon_0 h}{g}V^2 \tag{72}$$

In the above equation, L_0 is used to denote the overlap area's length between the capacitive plate of the tines and the drive electrode, and h is used to denote the structural thickness of the whole system.

It is known that both the AC and DC components will be used in the DETF structure. When they are supplied as the potential to the proof mass and the drive electrode, the above equations take the form;

$$F_{e,d} = -\frac{1}{2}\frac{\varepsilon L_0 h}{(g-x)^2}\left[\left(V_{DC}^2 + \frac{V_{AC}^2}{2}\right) + 2V_{DC}V_{AC}\sin(\omega t) - \frac{V_{AC}^2}{2}\cos(2\omega t)\right] \tag{73}$$

Of course, by adding both DC and AC terms, two frequency related terms in the electrostatic force formula have been obtained. With two frequency related terms, there exists a problem. ωt term will be affecting the tines of the resonators by setting the desired operation mode. However, in this case, $2\omega t$ term will cause the mechanical structure to be excited at the double of the desired operation mode. In order to neglect this effect, DC voltage must be much higher in terms of amplitude compared to the AC signal. If the voltages are chosen as stated in the previous

sentence, the problematic $2\omega t$ term can be neglected, which results in the simplified version of the equation (73),

$$F_{e,d} = -\frac{n\varepsilon_0 h}{g}\left(\frac{v_{AC}^2}{2} + V_{DC}^2\right) + \frac{n\varepsilon_0 h}{g} 2V_{DC} v_{AC} \sin\omega t + \frac{1}{2}\frac{n\varepsilon_0 h}{g}\cos 2\omega t \tag{74}$$

To cancel out the DC terms and the double frequency term, the device could be excited from both sides in the out-of-phase mode. The sinusoidal term will be doubled as a result of this

$$F = \frac{4n\varepsilon_0 h V_{DC} v_{AC}}{g}\sin\omega t$$

Since the structure is symmetrical, the electrostatic forces cancel each other which results in the double the spring constant.

$$k_e = \frac{2\varepsilon_0 L h}{g^3} V_{DC}^2$$

The Pull-in condition had been stated before; now, it is time to express it analytically. It happens when the electrostatic spring constant overcomes the mechanical spring constant of the DETF, in other words, $k_m = k_e$. It had been found that this condition happens when the displacement of the movable part reaches one-third of the capacitive gap. Pull-in voltage, the voltage value when the pull-in happens can be found by;

$$V_p = \sqrt{\frac{8k_m g^3}{27\varepsilon L_0 h}} \tag{75}$$

Pull-in voltage should always be kept in mind since it limits the DC voltage value during the capacitive actuation operations.

2.2.1.2. Capacitive Detection

As stated before, under the effects of the electrostatic forces, the tines of the DETF structures move; hence, capacitive detection takes place. As the tines of DETF structure moves, the capacitance between the sense electrode that is placed on the other side of the tines compared to the drive electrode and the proof mass of the resonator changes. As a result of the capacitance change, there is also a change in the stored charge in the capacitances formed between the sense electrode and proof mass. This change of the stored charge can be observed as a current flowing through the sense electrode. It is necessary to convert this current to a voltage by trans-impedance-amplifier, TIA, and should be fed to the read-out circuit of the resonator. Below, the illustration of the sense electrode positions and the capacitive sensing mechanism of the resonator can be seen.

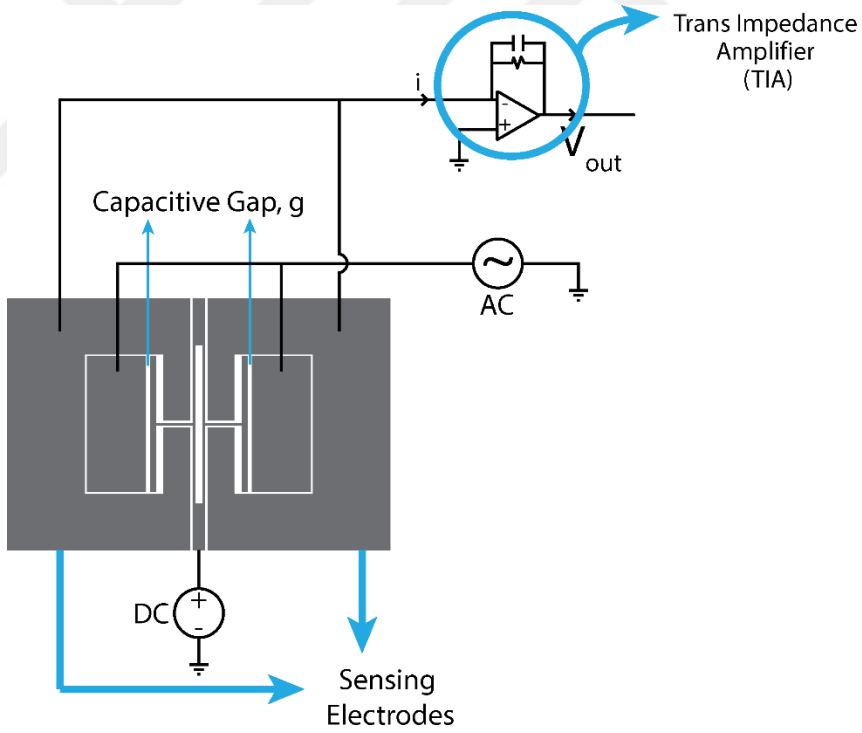

Figure 38. Schematic of the capacitive sensing mechanism

The mentioned current flowing through the sense electrode can be expressed as;

$$Q = CV \tag{76}$$

$$i = \frac{\delta Q}{\delta t} = \frac{\delta C}{\delta t} V + C \frac{\delta V}{\delta t} \tag{77}$$

In this formulation, i is used to denote the current, Q is used to denote the accumulated charge between the capacitive plates of sense electrode and the tines of the resonator, and V is used to denote the applied voltage in between capacitive plates. Using the chain rule, the time rate of the capacitive can be extracted. The second term in the right-hand side of the equation (77) can be neglected since the small amplitude of the AC signal:

$$i = \frac{\delta C}{\delta x} \frac{\delta x}{\delta t} V \tag{78}$$

It is essential to mention that the current flowing through the sense electrode is directly proportional to the velocity of the tine of the resonator, as seen in equation (78). It is also known that in addition to the velocity, it is also directly proportional to the applied DC voltage and the capacitance change. When the displacement formula is derived, it can be seen that it is a function of frequency, as stated before. This frequency term in the current formula is a result of the time derivative of the displacement. It can be concluded that the current flowing through the sense electrode depends on the frequency of the resonator. Also, it can be said that there should be a 90° phase difference as a result of the AC signal and the current flowing through the sense electrode.

In order to obtain the transfer function between the current and the displacement, the Laplace transform of the equation (78) should be taken as;

$$I(s) = \frac{\delta C}{\delta x} \, sX(s)V \tag{79}$$

In this representation, proof mass voltage V_{DC} can be used in equation (78) as V if drive signal is assumed to be negligible compared to the proof mass voltage. In order to transform the current to the voltage, an op-amp should be utilized as TIA, as shown in Figure 38. By this conversion, controlling and manipulating the product of capacitive sensing, the read-out circuit of the resonators can be enabled. V_{out}, the output voltage and the current flowing through the sense electrode can be associated as;

$$V_{out} = -iZ \tag{80}$$

In this representation, Z is used to denote the impedance that is created by the resistor and the capacitor on the TIA. To be more explicit, the output of TIA and the current relation can be obtained by the Laplace transform as;

$$V_{out}(s) = -I(s)\frac{R}{sRC+1} \tag{81}$$

By writing this, it is now possible to write the overall transfer function of the resonator as;

$$H(s) = \frac{V_{out}(s)}{V(s)} = \frac{X(s)}{F(s)}\frac{F(s)}{V(s)}\frac{I(s)}{X(s)}\frac{V_{out}(s)}{I(s)} = \frac{\left(\frac{\delta C}{\delta c}V_{DC}\right)^2 s}{ms^2+bs+k}\frac{-R}{sRC+1} \tag{82}$$

In the modeling of the resonators, this transfer function can be used.

2.2.2 **Mechanical Design of MEMS DETF Resonators Used in This Study**

In Chapter 1.3, it had been stated that DETF resonators would be used as a force sensing mechanism. It was aimed to achieve a design that can read applied force sensitively. Now, in this section, the proposed sensor design will be verified by both the analytical model and finite element modeling analyses. The design will be introduced in the following section with the principles of operations.

2.2.2.1. 1-Degree of Freedom Electromechanical Model

The momentum equation should be used to express the dynamic response of the tine in the absence of dissipative phenomena. This expression can be written as;

$$\frac{\partial^2}{\partial x^2}\left(EI\frac{\partial^2 v(x,t)}{\partial x^2}\right)+\frac{\partial}{\partial x}\left(\frac{F_{appl}}{2}\frac{\partial v(x,t)}{\partial x}\right)+\rho A\frac{\partial^2 v(x,t)}{\partial t^2}=P_e(x,t) \tag{83}$$

In this equation, v is used to denote the deflection, EI is used to denote the flexural stiffness, F_{appl} is used to denote the external axial force, and ρ is used to denote the density of the material. In order to continue, separation of variables will be used,

$$v(x,t)=\phi(\varepsilon)y(t) \tag{84}$$

Where $\varepsilon = x/L_f$, the equation of motion of the system becomes

$$M_{eff}\ddot{y}+K_{eff}y=P_e(t) \tag{85}$$

Where M_{eff} is used to denote the effective mass, K_{eff} is used to denote the effective stiffness, and c is used to denote the damping coefficient.

$$M_{eff}=\int_0^L \rho A\phi_i^2 dx+\sum_j m_j\phi_j^2(x_j) \tag{86}$$

$$K_{eff}=\int_0^L EI\left(\frac{\delta^2\phi_i}{\delta x^2}\right)dx+\int_0^L F\left(\frac{\delta\phi_i}{\delta x}\right)^2 dx \tag{87}$$

$$c=\frac{\sqrt{K_{eff}M_{eff}}}{Q} \tag{88}$$

Rearranging the equations with the help of $\varepsilon = x/L_f$, following expressions can be obtained;

$$K_{eff} = \frac{2EI}{L_f^3}\int_0^{\frac{1}{2}} \left(\frac{d^2\phi_i}{d\varepsilon^2}\right)^2 + \frac{2\frac{F_{appl}}{2}}{L_f}\left(\frac{d^2\phi_i}{d\varepsilon^2}\right)^2 d\varepsilon \tag{89}$$

$$M_{eff} = 2\rho A L_f \int_0^{\frac{1}{2}} \phi_i^2 d\varepsilon + \sum_j m_j \left(\phi_i(\varepsilon_j)\right)^2 \tag{90}$$

$\phi_i(\varepsilon)$ is used to denote the vibration mode shape, m_j is used to denote the mass of the actuation plate, L_f is used to denote the length of the tine, and Q is used to denote the quality factor of the mechanical oscillator. Different models had been studied for the estimation of Q as a function of device geometry and the medium viscosity, but, in this study, Q will be considered as an external parameter which can be adjusted by changing the air pressure, which is easy to do in a vacuum chamber. In this study case, the mode shape of the beam can be approximated to the elastic of a clamped-clamped beam, which has a point load at the center.

$$\phi_i = \phi_2 = 16\varepsilon^3 - 12\varepsilon^2 + 1 \tag{91}$$

By using this expression, both effective stiffness and effective mass can be calculated as;

$$K_{eff} = 192\frac{EI}{L_f^3} + 2.4\frac{F_{applied}}{L_f} \tag{92}$$

$$M_{eff} = \frac{13}{35}\rho h \omega_f L_f + \rho h\left(\omega_p L_p + \omega_c L_c + 2w_{comb} L_{comb} n_{comb}\right) \tag{93}$$

where, L_f and w_f are used to denote the length and width of the tine, L_p and w_p are used to denote the length and width of the actuation plane, L_c and w_c are used to denote the length and width of the connector, and h is used to denote the thickness of the device. The number of comb drives can be found by

$$n_{comb} = 1 + \frac{L_p - L_{comb}}{2(L_{comb} + g)}$$

By using both expressions, the damped natural frequency can be found as;

$$\omega_{n,D} = \sqrt{\frac{K_{eff}}{M_{eff}}(1-2\xi^2)}$$

$$= \sqrt{\frac{192\frac{EI}{L_f^3} + 2.4\frac{F_{applied}}{L_f}}{\frac{13}{35}\rho h\omega_f L_f + \rho h\left(\omega_p L_p + \omega_c L_c + 2w_{comb}L_{comb}n_{comb}\right)}(1-2\xi^2)} \tag{94}$$

Where ξ is used to denote the damping coefficient as;

$$\xi = \frac{1}{2Q} \tag{95}$$

In very low damping conditions, which can be expressed as $\xi \ll 1$, the equation can be written as

$$\omega_{n,D} = \sqrt{\frac{192\frac{EI}{L_f^3} + 2.4\frac{F_{applied}}{L_f}}{\frac{13}{35}\rho h\omega_f L_f + \rho h\left(\omega_p L_p + \omega_c L_c + 2w_{comb}L_{comb}n_{comb}\right)}} \tag{96}$$

With the following related sensitivity term (Frequency change for a unit applied force)

$$\frac{\delta\omega_n}{\delta F_{appl}} = \frac{1.2}{\omega_n M_{eff} L} \tag{97}$$

In the last equation, the sensitivity term is defined as the frequency change to a unit change applied force. This sensitivity term defined the scale factor of a single tine. It can be seen that the scale factor is not constant in the active range because of its dependence on resonance frequency itself.

While the tines move, a current which is proportional to its velocity is flowing. This current can be sensed by sensing plates, and it can be converted to a voltage signal via a trans-impedance amplifier of resistance R;

$$V = \frac{R\varepsilon_0 h L_p V_{DC}}{g^2}\dot{y} \tag{98}$$

2.2.2.2. 2-Degree of Freedom Electromechanical Model

In order to model the electromechanical coupling, it is necessary to model the system with at least 2 degrees of freedom. In state-space representation, the overall set of equations can be written as;

$$\begin{aligned} m_1\ddot{y}_1 + c_1\dot{y}_1 + c_{12}(\dot{y}_1 - \dot{y}_2) + k_1 y_1 + k_{12}(y_1 - y_2) &= P_{e,1} \\ m_2\ddot{y}_2 + c_2\dot{y}_2 + c_{12}(\dot{y}_2 - \dot{y}_1) + k_2 y_2 + k_{12}(y_2 - y_1) &= P_{e,2} \end{aligned} \tag{99}$$

Where, m_1 and m_2 are used to denote individual effective lumped masses of each tine, k_1 and k_2 are used to denote individual effective lumped stiffness constants of each tine and c_1 and c_2 are used to denote the individual effective lumped damping constants acting on each tine.

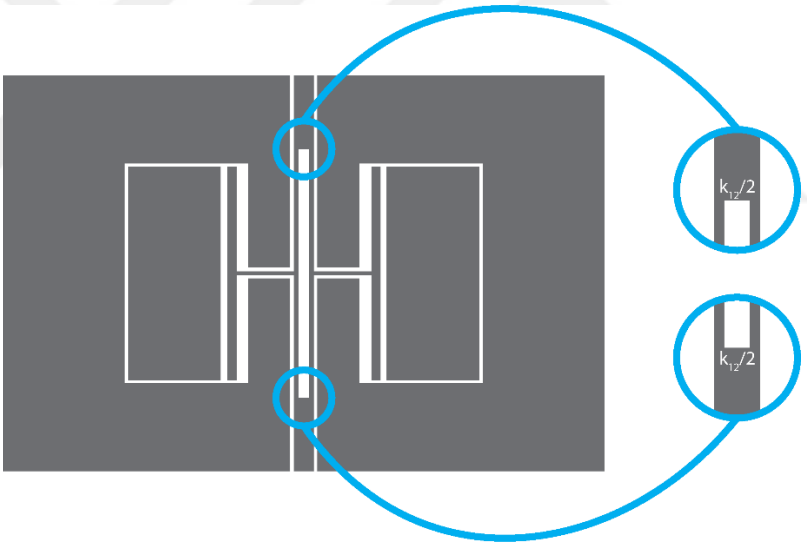

Figure 39. Representation of stiffnesses on connections

When the small fabrication variations are included in the system of equations, it will be much more inclusive. These fabrication variations will affect masses, stiffness constants, and electromechanical parameters. When they are introduced into the system of equations, the following expressions can be obtained.

$$\left(M_{eff}(1+\varepsilon_{m1})\right)\ddot{y}_1 + c_1\dot{y}_1 + c_{12}(\dot{y}_1 - \dot{y}_2) + K_{tine1}y_1 + k_{12}(y_1 - y_2) = P_{e,1}(1+\varepsilon_{e1}) \quad (100)$$

$$\left(M_{eff}(1+\varepsilon_{m2})\right)\ddot{y}_2 + c_2\dot{y}_2 + c_{12}(\dot{y}_2 - \dot{y}_1) + K_{tine2}y_2 + k_{12}(y_2 - y_1) = P_{e,2}(1+\varepsilon_{e2}) \quad (101)$$

Where,

$$K_{tine1} = K_{0,eff,e}(1+\varepsilon_{k1}) + 2.4\frac{F_{applied}}{L_f}(1+\varepsilon_F) \quad (102)$$

$$K_{tine2} = K_{0,eff,e}(1+\varepsilon_{k2}) + 2.4\frac{F_{applied}}{L_f}(1+\varepsilon_F) \quad (103)$$

In these expressions, $\varepsilon_m, \varepsilon_k, \varepsilon_e, \varepsilon_F$ are used to denote the variation coefficients for mass, electromechanical stiffness value, electromechanical transduction, and load sharing on each tine, respectively. $K_{0,eff,e}$ is used to denote the stiffness value of the tine when no force is applied, which can be expressed as;

$$K_{0,eff,e} = 192\frac{EI}{L_f^3} \quad (104)$$

When the overall set of equations are written in matrix form while including the electromechanical excitation and detection, they take the following forms;

$$\dot{Y} = AY + BU \quad (105)$$

$$V = CY \quad (106)$$

Where V is used to denote the trans-impedance amplifier output voltage, U is used to denote the driving input voltage and;

$$Y = \begin{bmatrix} y_1 \\ y_2 \\ \dot{y}_1 \\ \dot{y}_2 \end{bmatrix} \quad (107)$$

$$A = \begin{bmatrix} 0 & 1 & 0 & 0 \\ -\left(\frac{K_{Tine1}+k_{12}}{M_{eff}(1+\varepsilon_{m1})}\right) & -\left(\frac{c_1+c_{12}}{M_{eff}(1+\varepsilon_{m1})}\right) & \left(\frac{k_{12}}{M_{eff}(1+\varepsilon_{m1})}\right) & \left(\frac{c_{12}}{M_{eff}(1+\varepsilon_{m1})}\right) \\ 0 & 0 & 0 & 1 \\ \frac{k_{12}}{M_{eff}(1+\varepsilon_{m2})} & \frac{c_{12}}{M_{eff}(1+\varepsilon_{m2})} & -\left(\frac{K_{Tine2}+k_{12}}{M_{eff}(1+\varepsilon_{m2})}\right) & -\left(\frac{c_2+c_{12}}{M_{eff}(1+\varepsilon_{m2})}\right) \end{bmatrix} \quad (108)$$

$$B = \begin{bmatrix} 0 \\ -\dfrac{\varepsilon_0 h L_p V_{dc}}{g^2 M_{eff}(1+\varepsilon_{m1})}(1+\varepsilon_{e1}) \\ 0 \\ \dfrac{\varepsilon_0 h L_p V_{dc}}{g^2 M_{eff}(1+\varepsilon_{m2})}(1+\varepsilon_{e2}) \end{bmatrix} \tag{109}$$

$$C = \begin{bmatrix} 0 & \dfrac{R\varepsilon_0 h L_p V_{dc}}{g^2}(1+\varepsilon_{e1}) & 0 & -\dfrac{R\varepsilon_0 h L_p V_{dc}}{g^2}(1+\varepsilon_{e2}) \end{bmatrix} \tag{110}$$

Two critical aspects of this system should be noted:

1. The modal frequencies
2. The mode shapes

When the equation is simplified by neglecting the damping coefficients, the characteristic equation of A can be expressed as follows;

$$\omega^4 - \omega^2(\omega_a^2 + \omega_b^2) + (\omega_a^2\omega_b^2 - \omega_{ab}^4) = 0 \tag{111}$$

In this equation,

$$\omega_a^2 = \frac{K_{Tine1} + k_{12}}{M_{eff}(1+\varepsilon_{m1})} \tag{112}$$

$$\omega_b^2 = \frac{K_{Tine2} + k_{12}}{M_{eff}(1+\varepsilon_{m2})} \tag{113}$$

$$\omega_{ab}^2 = \frac{k_{12}}{M_{eff}\sqrt{(1+\varepsilon_{m1})(1+\varepsilon_{m2})}} \tag{114}$$

In this expression, ω_a is used to denote the system frequency when the second tine is clamped. In the same way, ω_b is used to denote the system frequency when the first tine is clamped. Finally, ω_{ab} is used to denote the strength of the coupling. The characteristic equation of A has two solutions with two peaks;

$$\omega_1^2 = \frac{\omega_a^2 + \omega_b^2}{2} - \sqrt{\left(\frac{\omega_b^2 - \omega_a^2}{2}\right)^2 + \omega_{ab}^4} \tag{115}$$

$$\omega_2^2 = \frac{\omega_a^2 + \omega_b^2}{2} + \sqrt{\left(\frac{\omega_b^2 - \omega_a^2}{2}\right)^2 + \omega_{ab}^4} \tag{116}$$

Recalling the Mohr Circle, which is used for the graphical representation of the transformation law, all of the frequencies can be drawn in the Mohr Circle. The lowest frequency corresponds to the in-phase mode, where the higher frequency corresponds to the anti-phase mode.

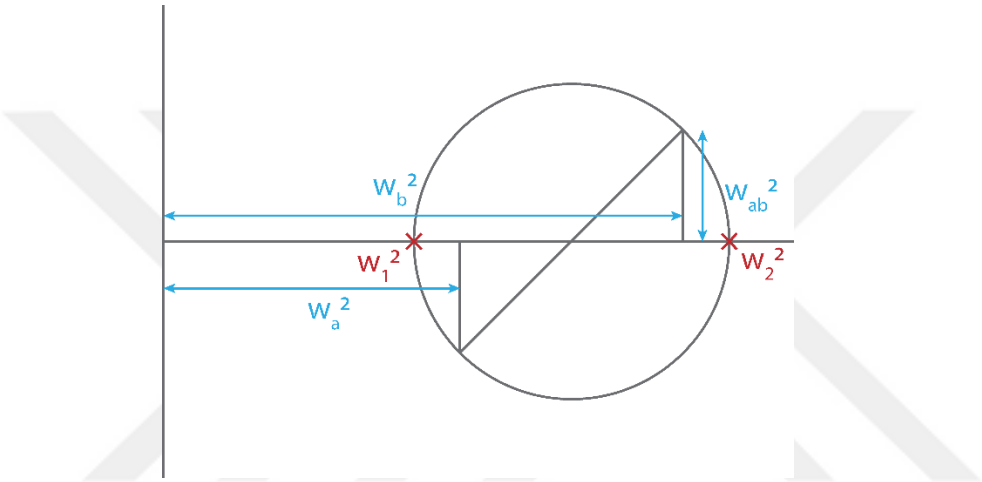

Figure 40. Mohr Circle Representation of the modes

When DETF is entirely fabricated, $\varepsilon_m = \varepsilon_k = \varepsilon_e = \varepsilon_F = 0$, without any damping, two modal frequencies can be expressed as;

$$\omega_{1,p}^2 = \frac{K_{eff,e}}{M_{eff}} \tag{117}$$

$$\omega_{2,p}^2 = \frac{K_{eff,e} + k_{12}}{M_{eff}} \tag{118}$$

By using these equations, the frequency separation at zero loads can be found as;

$$\omega_{2,p} - \omega_{1,p} = \frac{\sqrt{K_{eff,e} + k_{12}} - \sqrt{K_{eff,e}}}{\sqrt{M_{eff}}} \tag{119}$$

It can be observed that the effective stiffness of the tines decreases as the compressive tip loading increases. There is a point which then the load reaches buckling occurs, $\omega_{1,p} = 0$. This point of failure can be found by

$$F_{buckling} = -192\frac{EI}{L_f^2} + \frac{\varepsilon_0 h L_f L_p}{g^3} V_{dc}^2(1+\alpha) \quad (120)$$

When this critical point has been reached, the frequency of the second mode, which is now the minimum operating frequency for this mode, is

$$\omega_{2,min,p} = \sqrt{\frac{k_{12}}{M_{eff}}} \quad (121)$$

The last equation shows the lower frequency limit for the DETF operation when the second mode shape, out-of-phase, is chosen. It is clear that when the fabrication is perfect and connections are perfectly rigid, $k_{12} = 0$, the separation between the modes becomes zero, and the solution of the 1-DOF system becomes correct.

The chosen design parameters of the proposed DETF design can be seen in Table 6. Using these parameters, effective lumped design parameters have been calculated and tabulated in Table 7. As described before, using the analytical model in the previous section, lumped tine stiffness, $K_{eff,e}$ and tine mass, M_{eff} are calculated. It is known that the axial tine stiffness is $K_{axial} = {}^{2EA}/_{L}$, where E is used to denote the Young's Modulus of Silicon, A is used to denote the cross-sectional area, and L is used to denote the length of the tine. By using the axial tine stiffness, the tip deflection can be found by

$$\delta_{tip} = {}^{F}/_{K_{axial}} \quad (122)$$

In Figure 41 and Figure 42, the finite element analysis of the DETF for the displacement and equivalent stress fields in the DETF structure have been graphed for the $100\,mN$ axial static load. The tip is found as $0.866\,um$. The maximum equivalent stress is found as $753.1\,MPa$ which is much smaller than the yield strength of the Silicon, $2000\,MPa$.

Table 6. Geometrical Dimensions of the DETF used in this study

Parameter	**Symbol**	**Value (μm)**
Tine Length	L_f	650
Tine Width	w_f	10
Capacitive Plate Length	L_p	550
Capacitive Plate Width	w_p	10
Capacitive Gap	g	5
Connector Length	L_c	150
Connector Width	w_c	10
Device Thickness	h	27.5

Table 7. Results of lumped tine stiffness, and lumped axials stiffness values of the DETF used in this study

Parameter	**Symbol**	**Value**
Lumped Tine Stiffness	$K_{eff,e}$	$227{,}70\ N/m$
Lumped Tine Mass	M_{eff}	$0{,}97\ \mu g$
Lumped Axial DETF Stiffness	K_{axial}	$135507{,}25\ N/m$

2.2.3 **Finite Element Modeling (FEM) Simulations of MEMS Double-Ended Tuning Forks**

In order to see the operational range of the sensor, three-dimensional finite element analysis has been performed in COMSOL 5.2. Only one physic has been used in this study, Solid Mechanics. Also, both eigenvalue and prestressed eigenvalue studies have been performed.

In Figure 41, the deflection response of the DETF has been shown in the $0.01\,N$ compressive load. Moreover, in Figure 42, stress distribution along the DETF has been shown in $0.01N$ compressive load. In Table 8, the first ten modes for stationary DETF can be seen. On these ten modes, mode number 8, 75863 Hz, is the out of plane mode, and the DETF will be operated on this mode.

Out of phase mode of the DETF structure is the preferred operational mode for the DETF because of its excellent stability. It can be seen that with the pretty close frequencies, different modes exist. These similar modes are the result of the design of the DETF. Since the DETF is symmetric, every two modes have very close frequencies.

In addition to those, two more analyses have been run to see the effects of varying force and displacement on the DETF. The first one is the effect of the external deflection on DETF. With changing the displacement by 0.025N, a graph of the effect of the external deflection has been plotted. Between $-0.0525\,\mu m$ and $-0.055\,\mu m$ external deflection pull-in occurs on the DETF, which is the result of touching of the comb drives on the electrodes and the tines. The second one is the effect of the external force on DETF. With changing the external force by $0.005\,N$, a graph of the effect of the external force has been plotted. Between $-0.070N$ and $-\,0.075N$, external force pull-in occurs on the DETF.

These values are critical since the sensitivity of the sensor increases as it comes near the pull-in values. Figure 43 depicts the natural frequency vs. external deflection graph to illustrate the effect of the deflection. In Figure 44, the natural frequency vs. external force graph shows the effect of the external force on the DETF.

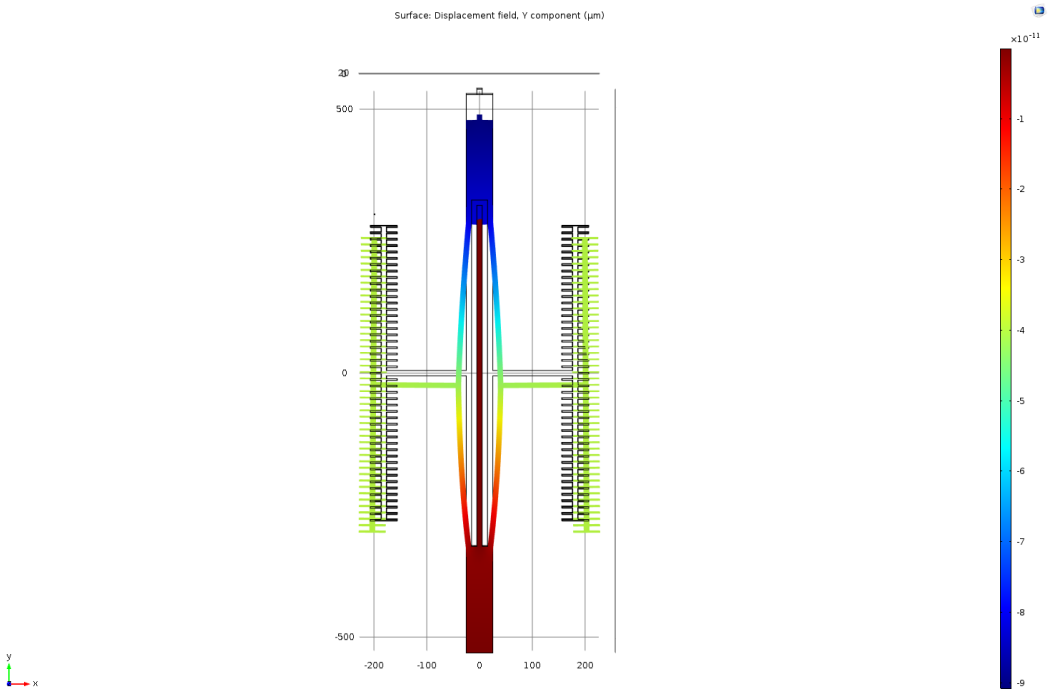

Figure 41. Finite Element Analysis Result for Deflection of proposed DETF

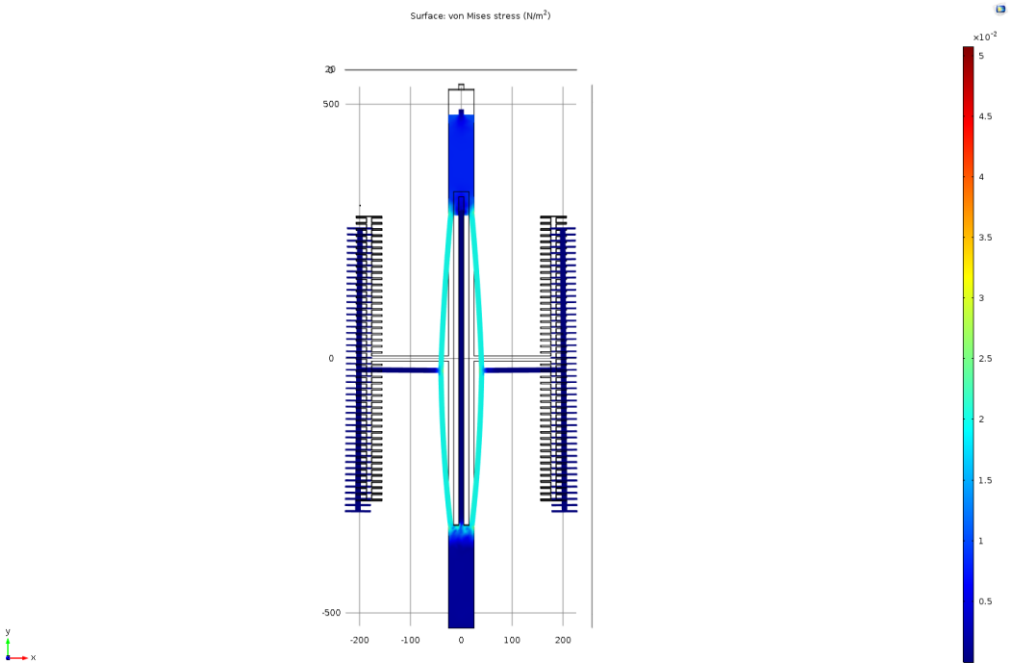

Figure 42. Finite Element Analysis Result for Equivalent Stress Fields of proposed DETF

Table 8. First ten modes for the stationary DETF

Mode Number	Frequency (Hz)	FEM Results
1st	42103	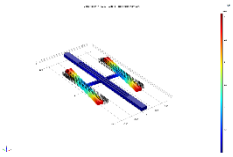
2nd	42600	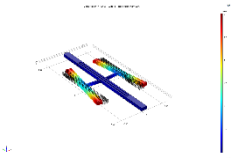
3rd	58662	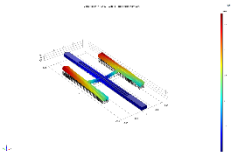
4th	60171	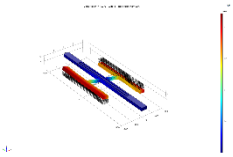
5th	65329	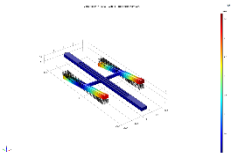
6th	65869	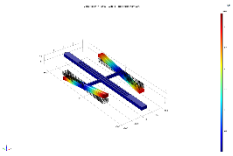
7th	71683	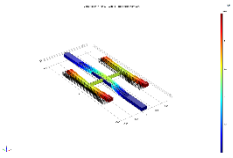
8th	75955	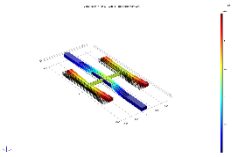
9th	150180	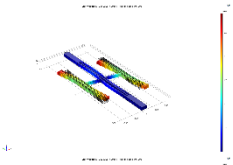
10th	151330	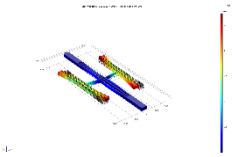

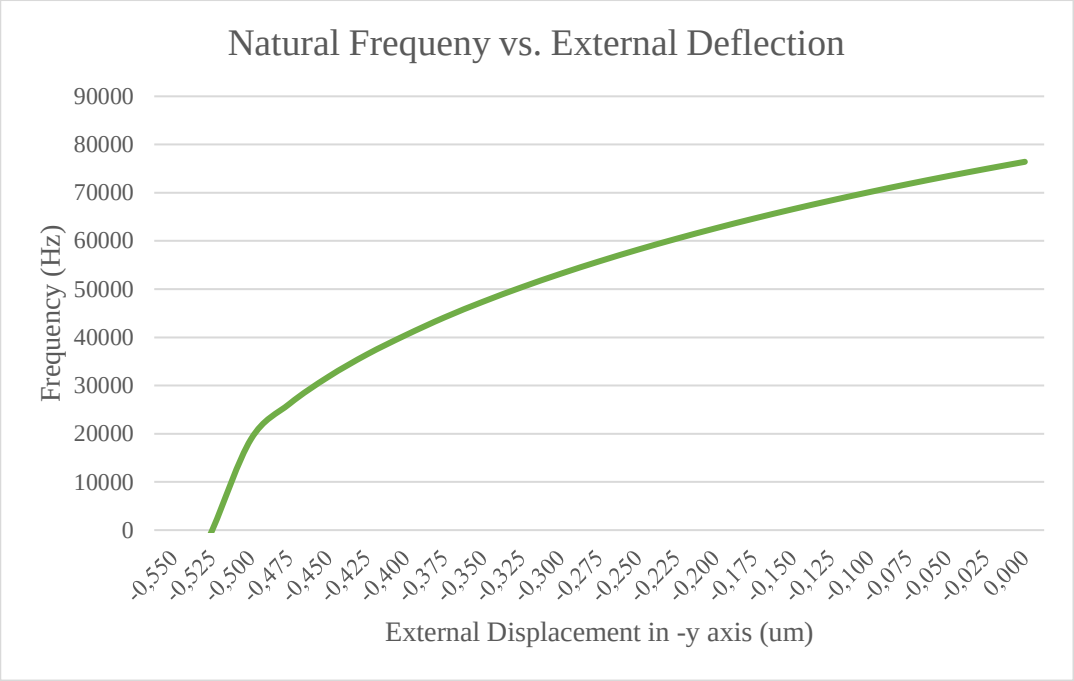

Figure 43. Natural Frequency vs. External Deflection graph from the Finite Element Analysis of the DETF studied in this thesis

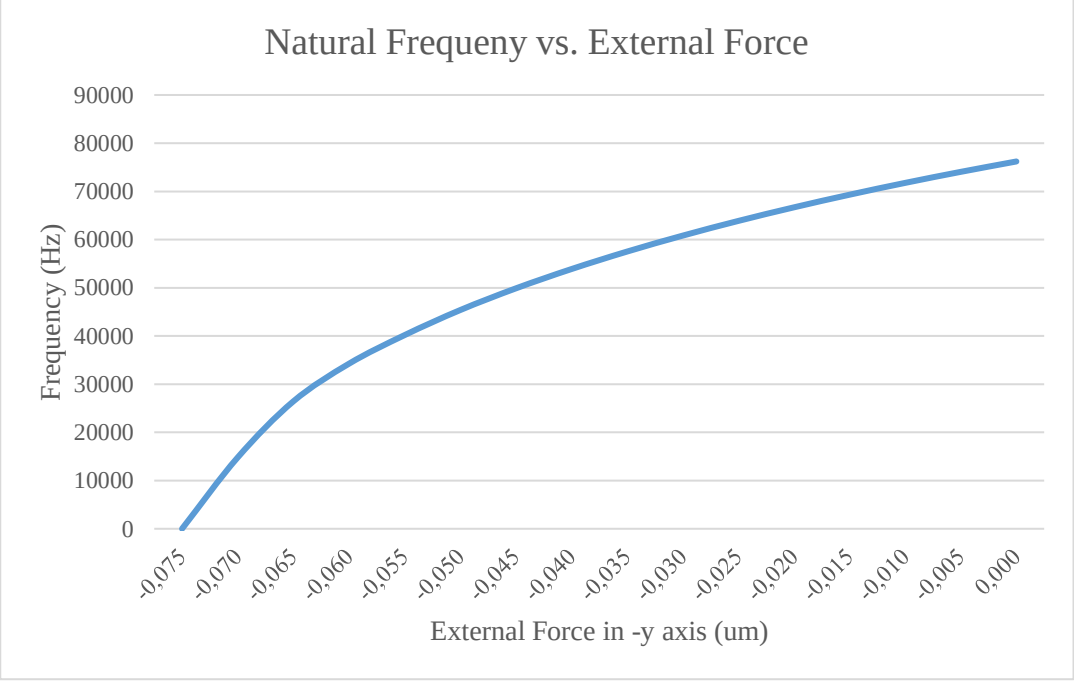

Figure 44. Natural Frequency vs. External Force graph from the Finite Element Analysis of the DETF studied in this thesis

2.3. **Design of MEMS Tensile Test Setups**

MEMS Test Setups have been used extensively to measure the mechanical properties of materials in μm level samples, as stated in Chapter 1.1. In this study, as stated before, the MEMS-based test setup will be used to measure both mechanical properties and behaviors of cardiomyocytes and other types of contractible cells. To explain the working principles of MEMS Test Setups, firstly, operation principles of MEMS Test Setups will be discussed. This will take place in Chapter 2.3.1 by analyzing the working principles of Test Setup proposed in this study in detail. After understanding the working principles of it, the mechanical design of the MEMS-Based Test Setup proposed in this study will be derived in Chapter 2.3.2. Lastly, by obtaining the Finite Element Modelling results, the accuracy of the derived analytical model of the MEMS Test Setup proposed in this study and the results of the Finite Element Modelling Simulations will be presented in Chapter 2.3.3.

2.3.1 **Operation Principles of MEMS Tensile Test Setup Used in This Study**

The three main parts of the system, actuation, cell attachment, and force sensing, will occupy a different amount of area. The actuation part will take up μm^2 area, cell attachment part will take μm^2 area and force sensing part will take μm^2 area. Each part will be examined individually and then, all together, to see the results.

In the actuation part, there will be four groups of actuators in which the outer two of them will move on + direction while the inner two will move on – direction. That way, both tensile and compressive force and deflection can be generated in the same system. Since the cell attachment part determines the width of the sensor, the length of the actuators is chosen to fill the most of this width. $500\ \mu m$ length of the actuators take the most place while still satisfy a rigid structure. 150 actuators have been placed in series in each group to create a more significant force on the cells.

Outer two actuator groups have been placed such that they also create force in – direction, but by putting a lever before connecting all these groups, generated force

and deflection have been switch to + direction. It was necessary since the upper end of the actuator group generated more force and deflection compared to the lower end of the group, as discussed in Chapter 2.1.3.3.

All four groups of actuators have been connected to one thick beam by four springs to create both tensile and compressive forces. This thick beam is supported by rollers to maintain its direction of movement in the prescribed direction. Then this thick beam is connected to the cell attachment part.

In the cell attachment part, there are two large plates with the dimensions of $1000\ \mu m\ x\ 500\ \mu m$. These large plates will be supported by many rollers outside, and to neglect any collapse inside, plates will also be supported by rollers inside. These rollers are fixed at the other end, which is called anchors. In these anchors, there are pads to ground the plates so that static can be neglected, which may harm the cells during the tests.

While one plate is connected to the actuation part, the other part is connected to the force-sensing part, and the only connection between these two plates will be the cell to be tested. The gap between the plates is $10\ \mu m$ since It has been shown that cardiomyocyte's length differs from ~75μm to ~150μm while their width differs from ~30 μm to ~40 μm as stated in Chapter 1.1. 10 μm difference will be significant for both tensile and compressive tests.

The force sensing part is connected to the plate by one end of the DETF resonator. The other end is connected to the fixed end. By drive end sense electrodes, DETF will be operated. Any force or deflection change at the connected pad will be directly measured since the natural frequency of the tines will change.

2.3.2 **Mechanical Design of MEMS Tensile Test Setup Used in This Study**

It has been shown that the actuator groups will be connected to the system by springs in order to create both tensile and compressive motion in the same

system. Because of these springs, net deflection on the cells will be different compared to what has been generated on actuators. For the actuator part in the middle, which generates the compressive motion, net deflection acting on the cells will be half of what they generate; in other words, for a unit deflection generated on actuators net 0.5 unit deflection will be generated on cells. This is the result of the same springs used at the end of actuators. The schematic of the system can be seen in Figure 45.

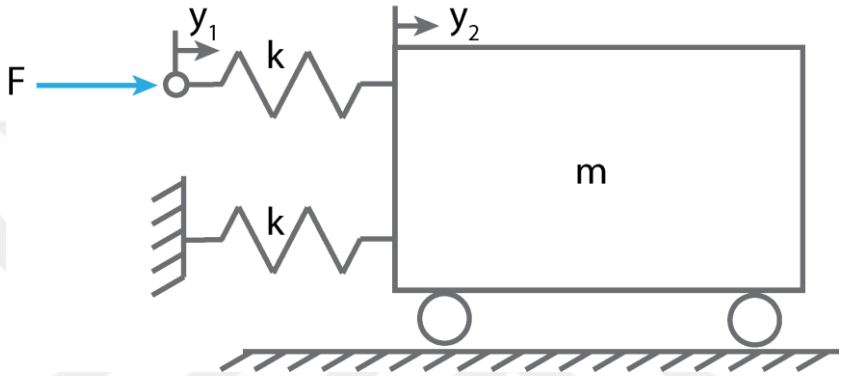

Figure 45. Mechanical Model for the Compressive State of the System

On the other hand, in the tensile state, things are different. Because of the lever, total stiffness is different when outer actuators work. The schematic of the tensile state can be seen in Figure 46.

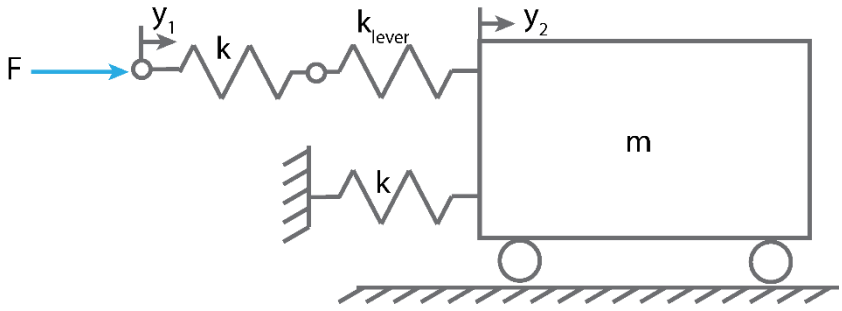

Figure 46. Mechanical Model for the Tensile State of the System

The effects of the lever will be shown in Chapter 2.3.3 with the help of finite element analysis of the system. After that, the actuation part will be connected to the roller supported plate, where part of the cell will be attached. To make the connection

between the plates, a cell is necessary since there is no other connection. When connected, the other plate which is connected to DETF will experience the force, and this force will be measured thanks to DETF.

Since rollers and actuators will support the plates and the thick beam on the actuation part will be connected by springs, in the next section, rollers and springs will be examined in detail.

2.3.2.1. Flexion Elements

In this tensile test setup, various flexion elements are used to characterize and limit the movement of the structure. For this purpose, firstly, single-sided double folded springs will be explained. They are essential because their geometrical properties decide the sensitivity, operation frequency, and many aspects of the sensor structure.

This type of flexion element consists of beam elements connected to the rigid masses. Single-sided double folded springs are chosen because of their much higher stiffness in the vertical axis and linearity of the structure. [82]

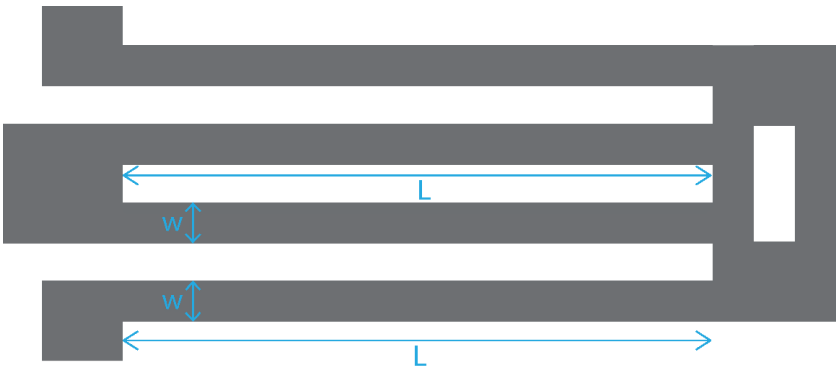

Figure 47. Roller design and dimensions used in the analytical model

If a beam is assumed to be in under force and moment loading, angles of its endpoint deflections can be found by

$$\theta_{Force} = \frac{FL^2}{2EI} \tag{123}$$

$$\theta_{Moment} = \frac{ML}{EI} \tag{124}$$

The slope of the endpoints of the beams which form the folded spring structure that is parallel to each other is zero. To achieve that, force and moment pair should be utilized. By combining these,

$$\theta_{Load} = \theta_{Moment} \tag{125}$$

This equilibrium results in

$$M = \frac{FL}{2} \tag{126}$$

Using superposition of deflections of the moment and the load, the deflection at the one end can be found by;

$$u = \frac{FL^3}{3EI} - \frac{ML^2}{2EI} \tag{127}$$

By substituting M and I;

$$\frac{F}{u} = k_y = \frac{Ehw^3}{L^3} \tag{128}$$

This spring type is stiffer in the vertical axis to its fully balanced force and moment equilibrium. The spring constant of this structure is equal to the spring constant of the single guided beam, that is,

$$k_y^{folded} = \frac{Ehw^3}{L^3} \tag{129}$$

The vertical spring constant, in the x-direction, is then simply,

$$k_x^{folded} = \frac{Ehw}{L} \tag{130}$$

It is known that this type of spring is much stiffer and linear compared to the double folded and double-sided type. All the folded suspension springs are chosen to be used in this type.

In order to combine both tensile and compressive movement in the system, folded beam springs are chosen to be used in the system. Thermal actuators which are

connected in series are connected to the system in both tensile and compressive directions. Of course, the generated deflection will be half of what is produced in the connected actuators part of the system, but by this springs, the double-sided test environment can be created. [83]

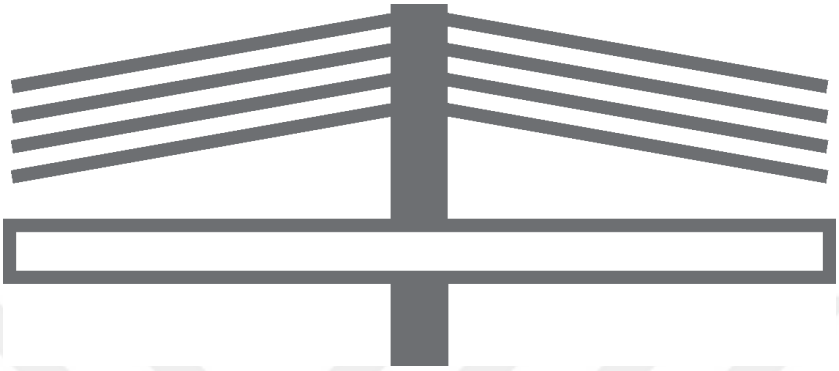

Figure 48. Representation of how springs will be connected to the actuator groups

The folded beam incorporates three components arranged in a series. The stiffness constant of the quarter model can be given in complementary form by

$$\frac{1}{k_{\frac{1}{2}}} = \frac{1}{k_{c1}} + \frac{1}{k_{c2}} + \frac{1}{k_{c3}} \tag{131}$$

The first and third components of the spring are similar to the model of half fixed-fixed beam with a length, 2L, under a transverse load, F, at the midspan of the beam. Shear reaction force, R_a and bending moment M_0 for the model of a half-fixed-fixed beam were obtained as $R_y = \frac{F}{2}$, and $M_0 = \frac{FL}{4}$.

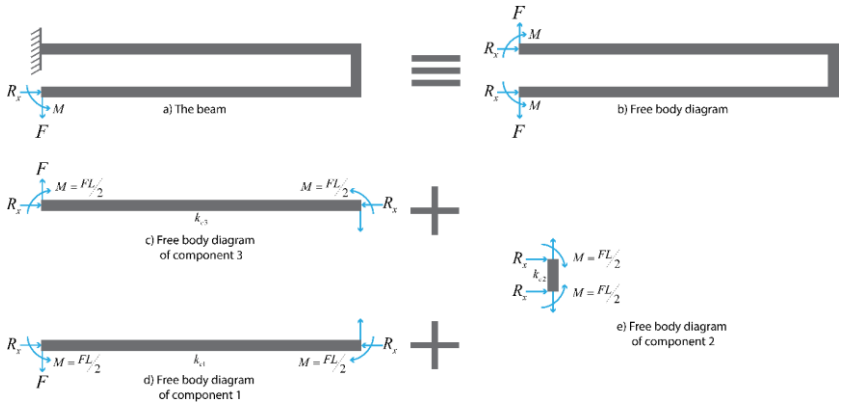

Figure 49. Representation of analytical spring analysis steps

The maximum deflection due to the bending moment happens in the middle of the beam for a fixed-fixed beam. The maximum deflection can be found as;

$$\delta_{bm} = \frac{F(2L)^3}{192EI} = \frac{FL^3}{24EI} \rightarrow k_{full} = \frac{F}{\delta_{bm}} = \frac{24EI}{L^3} \tag{132}$$

For the half model, the stiffness coefficient due to the bending moment was half of the stiffness constant of the full model.

$$k_{bm} = \frac{1}{2}k_{full} = \frac{12EI}{L^3} \tag{133}$$

For a rectangular cross-section area with a specific width, w, and depth, d, the total length of the beam, L, applied transverse load, F/2, The maximum deflection due to shear is given by

$$\delta_s = \frac{3}{5}\frac{F_s L}{wdG} \tag{134}$$

Where G is the shear modulus and can be found as $G = \frac{E}{2(1+\mu)}$.

$$\delta_s = \frac{6}{5}\frac{(1+\mu)FL}{wdE} \rightarrow k_s = \frac{5}{6}\frac{wdE}{(1+\mu)L} \tag{135}$$

The second component is found by a model of a bar element subjected to transverse force and bending moment. These forces and moments are transferred from the first and the third components.

Deflection due to transverse force can be found by,

$$\delta_t = \frac{R_y L_{c2}}{EA_{c2}} = \frac{FL_{c2}}{EAC_2} \rightarrow k_t = \frac{EA_{c2}}{L_{c2}} \tag{136}$$

Deflection in y-direction because of the bending moment can be found by;

$$\delta_y = -\frac{ML_{c2}^2}{2EI_{c2}} = -\frac{FLL_{c2}^2}{4EI_{c2}} \tag{137}$$

Where $M = \frac{FL}{2}$. Stiffness constant due to the bending moment can be found as;

$$k_{bm2} = -\frac{4EI_{c2}}{LL_{c2}^2} \tag{138}$$

The equilibrium stiffness constant is the folded beam can be determined as

$$\begin{aligned} \frac{1}{k_e} = \frac{1}{2k_{\frac{1}{2}}} = \frac{1}{2}\left(\frac{1}{k_{\frac{1}{2}}}\right) = \frac{1}{2}\left(\frac{1}{k_{c1}} + \frac{1}{k_{c2}} + \frac{1}{k_{c3}}\right) \\ = \frac{1}{2}\left[\left(\frac{1}{k_{bm}} + \frac{1}{k_s}\right) + \left(\frac{1}{k_t} + \frac{1}{k_{bm2}}\right) + \left(\frac{1}{k_{bm}} + \frac{1}{k_s}\right)\right] \end{aligned} \tag{139}$$

$$\frac{1}{k_e} = \frac{1}{k_{bm}} + \frac{1}{k_s} + \frac{1}{2k_t} + \frac{1}{2k_{bm2}} \tag{140}$$

The effective stiffness constant of the folded beam spring can be obtained by substituting the stiffness values.

$$\frac{1}{k_e} = \frac{L^3}{12EI} + \frac{6}{5}\frac{(1+\mu)L}{wdE} + \frac{L_{c2}}{2EA_{c2}} - \frac{LL_{c2}^2}{8EI_{c2}} \tag{141}$$

2.3.3 **Finite Element Modeling (FEM) Simulations of MEMS Tensile Test Setup**

In order to see if the assumptions were right, the next step is performing a finite element analysis for the system. To do that, two simulations have been performed for tensile and compressive states. When the compressive state analysis has been performed, it is found that previously assumed nearly half deflection on plates

became true. In Table 9, solutions for different values can be seen, also in Figure 50, the deflection behavior of the system can be seen.

Table 9. Finite Element Analysis Results of the Compressive State for variable voltage values

Voltage	Deflection on the Actuators	Deflection on the Plates
2	0.74	0.37
4	2.98	1.51
6	6.72	3.40
8	11.95	6.05

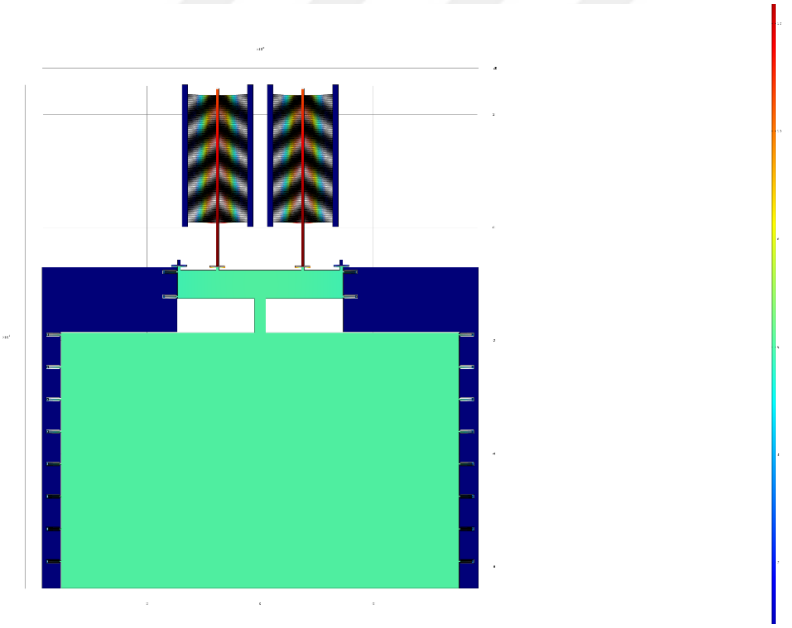

Figure 50. Finite Element Analysis Result of the compressive state for the voltage value of 8V

When the tensile state analysis has been performed, it is found that previously assumed, much less deflection became true. That occurs because of a design error in the spring-lever mechanism. If the mechanism designed such that actuators first apply force to the lever and then the direction changed, force act on the spring deflection on the plates would be more significant. However, during this study, the first mechanism will take place. That is why models and simulations are performed on that design. In Table 9, solutions for deflections on the actuators and the plates

can be seen. Compared to the compressive state, the tensile state's deflection on plates is much smaller. Also, in Figure 51, the deflection behavior of the system can be seen.

Table 10. Finite Element Analysis Results of the Tensile State for variable voltage values

Voltage	Deflection on the Actuators	Deflection on the Plates
2	0.65	0.035
4	2.60	0.32
6	5.85	0.74
8	10.41	1.15

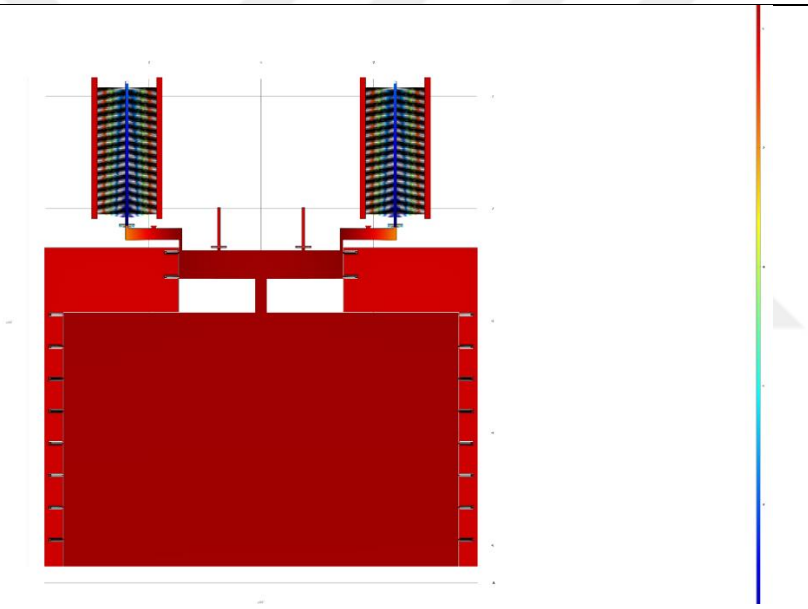

Figure 51. Finite Element Analysis Result of the tensile state for the voltage value of 8V

In addition to a tensile and compressive state analysis, analysis for flexion elements should also be performed in order to verify the analytical model of them. In this manner, two simulations have been performed for roller and spring.

In spring simulation, for spring with $200\,\mu m$ length, $10\,\mu m$ width, and $25\,\mu m$ height, it is found that analytically solved equilibrium stiffness is $720.96\,N/m$. When the same design has been simulated in COMSOL 5.2, the equilibrium stiffness

value is found as 734.23 N/m, which is pretty close to what has been found in the analytical model. It can be said that the analytical model has been verified. In Figure 52, analysis results can be seen.

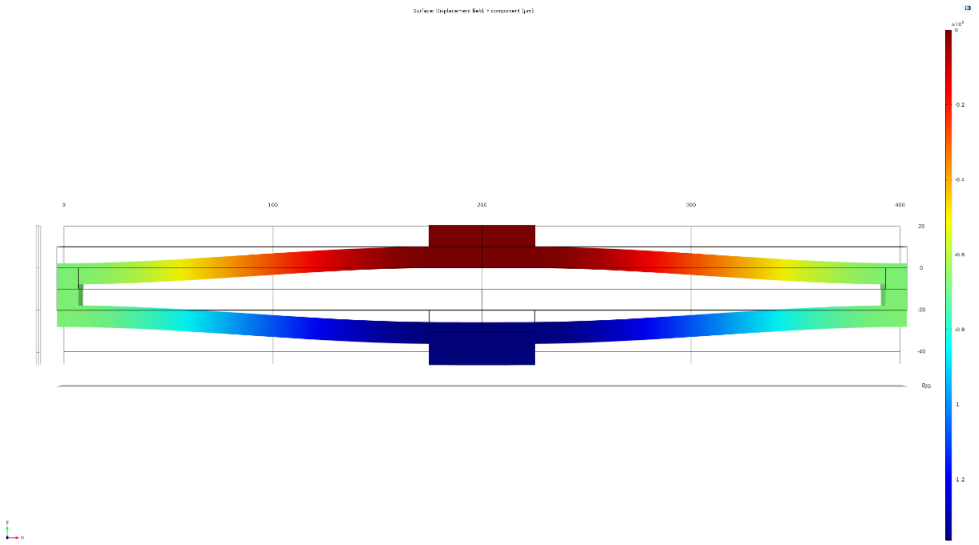

Figure 52. Finite Element Analysis of Spring Structure used in this study

For the roller, the same procedure will be followed. For a roller with 200 μm length, 10 μm width, and 25 μm height, equivalent stiffness value in y-direction has been found as 399.136 N/m. When the same design has been simulated in COMSOL 5.2, the equilibrium stiffness value is found as 387.60 N/m, which is pretty close to what has been found in the analytical model. Again, analytical results have been verified by simulation results. In Figure 53, analysis results can be seen.

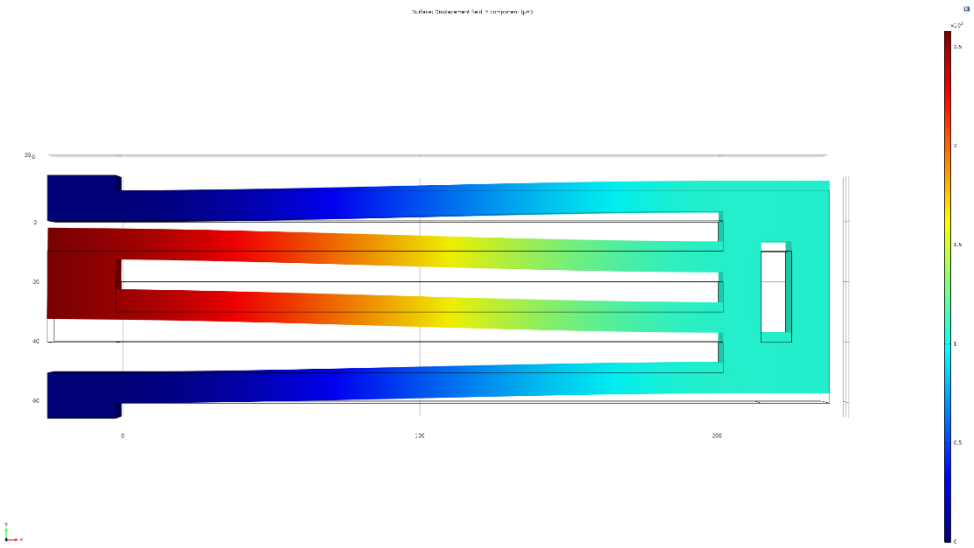

Figure 53. Finite Element Analysis of Roller Structure used in this study

CHAPTER 3

3. FABRICATION OF MEMS TENSILE TEST SETUP

In this chapter, the fabrication processes of the MEMS Tensile Test Setup, whose design procedures had been explained in Chapter 2, will be explained step-by-step. This chapter consists of 4 subchapters. In Chapter 3.1, the fabrication of the structure wafer, which has the sensor structures, will be presented with step by step figures and tables. In Chapter 3.2, the fabrication of the substrate wafer will take place. This wafer will be bonded to the structure wafer, and it includes gold plates to manipulate the system. In Chapter 3.4, fabrication results will be examined with the help of SEM images of the fabricated and the diced sensor dies. At last, in Chapter 3.5, fabrication results of each wafer and the results of fabrication will be summarized.

The fabrication starts on a Silicon-on-Insulator (SOI) wafer for the sensor structures. It continues with the silicon wafer for substrate manufacturing. The two wafers will be bonded by eutectic bonding to each other to obtain the desired final sensor die.

It should be noted before going into detail that the fabrication steps have been performed by Ertuğ Şimşek on METU MEMS Center.

3.1. **Fabrication of Sensor Structures**

Figure 54 shows the cross-sectional view of the sensor structure wafer after each step through 1 to 4. Fabrication of the sensor structure wafer will be done by using a silicon-on-insulator (SOI) wafer. The material properties of the SOI wafer are shown in Table 11.

Table 11. Material Properties of the SOI Wafer

Properties	Value
Handle Thickness	482.6 μm
Handle Resistivity	$1000 - 2000\ \Omega cm$
Device Thickness	27.5 μm
Device Dopant	Boron-P Type
Device Resistivity	$0.004 - 0.006\ \Omega cm$
Oxide Thickness	2.2 μm

Until the bonding of both wafers, the only thing that will be done on the sensor structure wafer is Deep Reactive-Ion Etching (DRIE). All the steps will be mentioned in detail with their relative figures in Figure 54.

1. The SOI wafer had been prepared for fabrication. Dehydration, cooling, and center and dust cleaning had done at this step.
2. Lithography had been performed at this step. Firstly, the primer coat had been applied; after that, Photoresist (PR) coating was applied by the help of Spinner. After the coating, the soft bake took place. After the exposure at the Mask Aligner, development had been performed. Moreover, finally, rinsing and drying of the wafer took place.
3. Then, DRIE silicon etch had been performed.
4. At this final step, polymer removal took place. Furthermore, to control if the structure fabricated right, etch profiles and depth were controlled in the Scanning Electron Microscope.

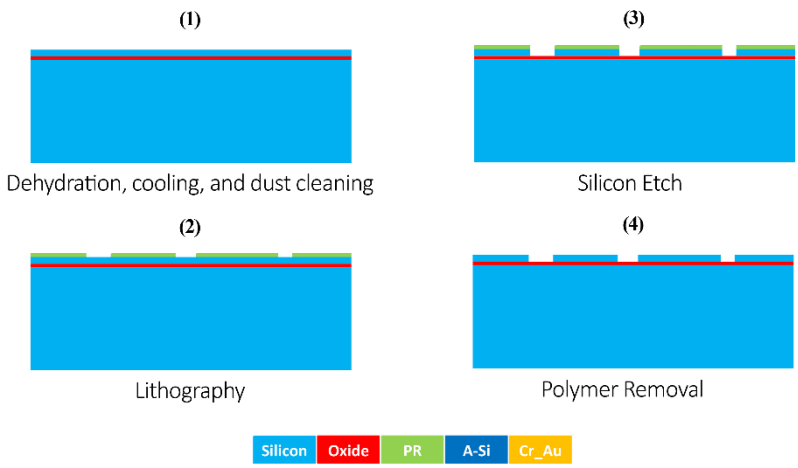

Figure 54. Fabrication Steps of Sensor Wafer

3.2. **Fabrication of Substrate Wafer**

Figure 55 shows the cross-sectional view of the substrate wafer after each step through 1 to 16. Fabrication of the substrate wafer will be done by using a silicon wafer. The material properties of the silicon wafer are shown in Table 12.

Table 12. Material Properties of the silicon wafer

Properties	**Value**
Type	Prime Wafer
Diameter	$100\ mm$
Thickness	$500 - 550\ \mu m$
Dopant	Boron-P Type
Resistivity	$10 - 20\ \Omega - cn$
Front Side	Polished
Back Side	Etched

Every process had been done until the bonding of both wafers. All the steps of its fabrication will be mentioned in detail with their relative figures in Figure 55.

1. The first process will be Piranha and BHF cleaning.
2. A protective Oxide layer had been applied to the top surface.
3. In this step, lithography took place. After dehydration, cooling, and drying, the primer coat was applied. Then, on top of the primer coat, the PR mask coat had been applied by the spinner. After that process, a soft bake was performed. Next, using mask aligner, exposure took place, and finally, development had been completed. After development, rinsing and drying took place. After the lithography, DRIE took place to etch the desired cavities.
4. Next, the PR Strip and piranha cleaning took place. The following steps had performed piranha cleaning; organic cleaning, cleaning, and drying.
5. By using BHF, oxide had been removed from the silicon wafer. Then, cleaning, drying, and dehydration steps took place.
6. In this step, Oxide Deposition or Thermal Oxidation took place.
7. Again, as in step 3, lithography had been performed. After dehydration, cooling, and drying, the primer coat was applied. Then, the PR mask coat was applied, and a soft bake had been performed on the wafer. After that, exposure took place by mask aligner, and development had been completed. Finally, rinsing, drying, and hard bake was performed.
8. Oxide etch had been performed by Reactive Ion Etching (RIE) to create the desired cavities on the oxide layer.
9. To remove the Photoresist, PR strip and piranha cleaning took place.
10. To create the desired cavities on silicon, firstly, wetting of the wafer had been performed. Then, native oxide removal took place, and finally, before rinsing the wafer, Si etch had been performed by TMAH.
11. As in step 10, this step again started by wetting the water. Then, in 1:5 BHF solution, oxide etch had been performed. Then, piranha cleaning took place.
12. Thermal oxidation took place in this step to cover the top surface by oxide.

13. In this step, metal evaporation took place to supply the relevant metal to create the necessary circuits and pads in the design.
14. On the top metal layer, lithography had been performed. As in previous steps, it has started with dehydration, cooling, and drying. After the primer coat and PR mask coat applications, the soft bake took place. Then, exposure and development had been performed. Finally, rinsing, drying, and hard bake took place.
15. In this step, metal etch had been performed to create the desired pads and circuits in the design. After the gold etched by Au etchant, rinsing, cleaning, and drying had been completed.
16. In this final step, PR strip and piranha cleaning had been performed as in previous steps.

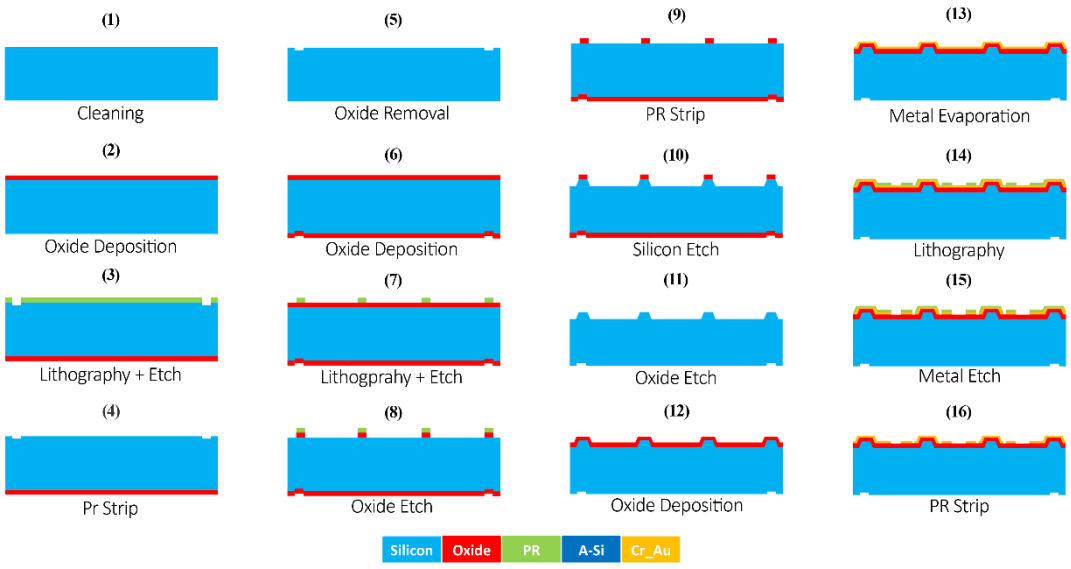

Figure 55. Fabrication Steps of Substrate Wafer

3.3. **Bonding of the Wafers**

Figure 56 shows the cross-sectional view of the bonding processes of both sensor wafer and substrate wafer after each step through 1 to 6.

1. This step started with native oxide cleaning by BHF. Then, Eutectic bonding had been performed.
2. Stack had been flipped upside down, and Vapor HF had been performed to remove sacrificial oxide layers.
3. In this step, thinning had been performed to remove all of the handle layers of the SOI wafer.
4. Then, oxide had been etched as in previous actions on wafer fabrication processes.
5. Next, after dehydration, the primer coat and PR mask coat had been applied, respectively. Moreover, as a final step, soft bake had been performed on the wafer.
6. In the final step, resist stripping had been performed by plasma cleaning.

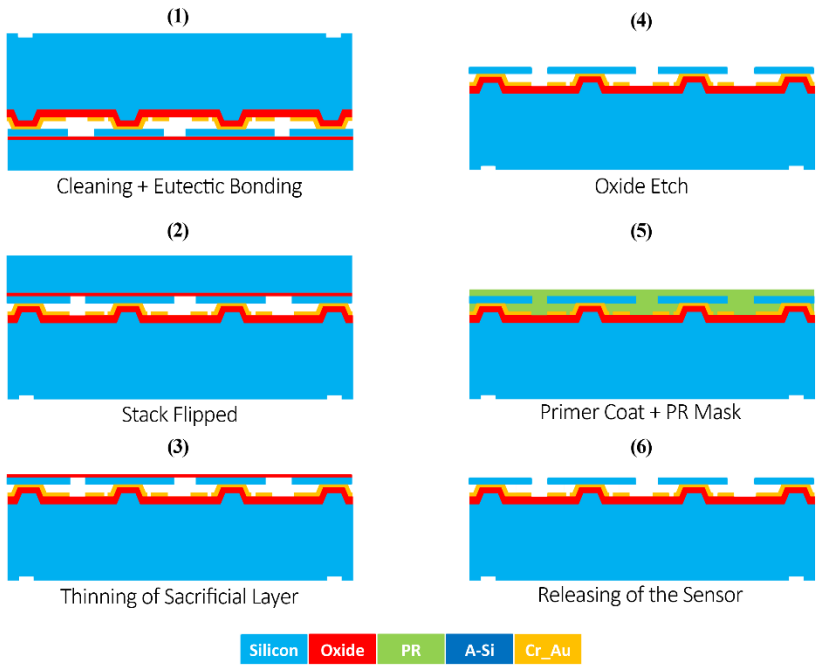

Figure 56. Bonding Steps of Sensor Wafer and Substrate Wafer

3.4. **Fabrication Results**

After the fabrication is done, the fabricated sensor dies have been examined with the help of SEM images taken in METU-MEMS Research and Application Center. In the examination process, critical dimensions, gold deposition quality, and critical device geometries are checked.

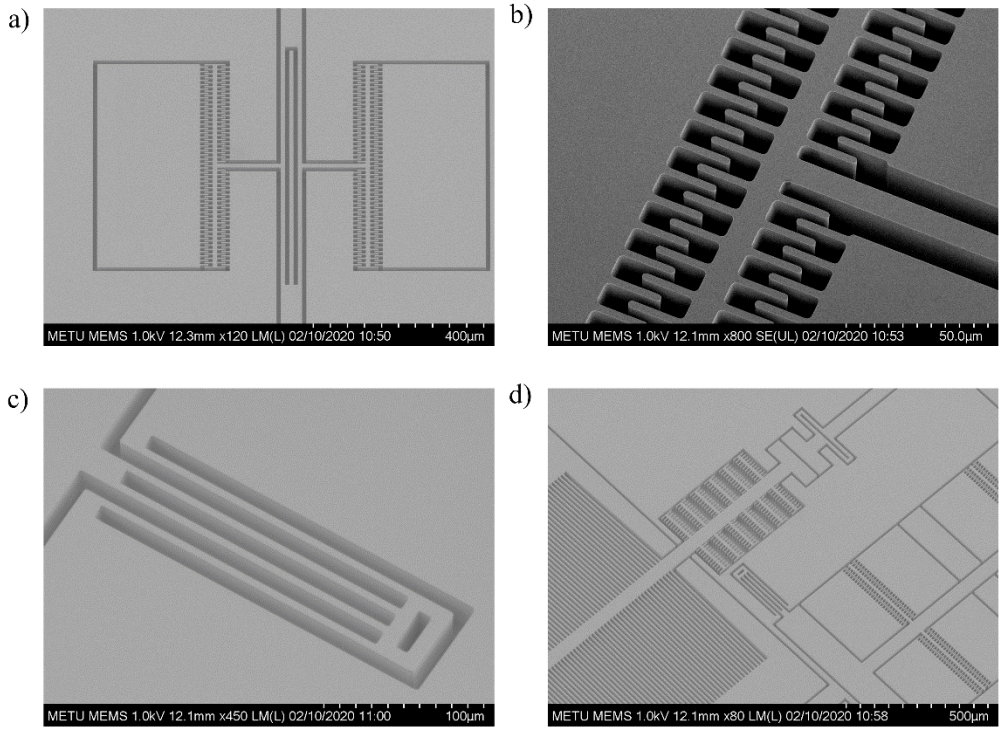

Figure 57. SEM images of the sensor taken after the fabrication. a) DETF part of the sensor b) Close shot of comb drive structures c) Close shot of the rollers used to support plates in the sensor d) Actuator and spring structures

The biggest problem was plates that cells would be attached broken in every sensor. This can occur because of two things; the first, rollers cannot support the plates and they break and the other is while wet etching, even a small amount of liquid can break the pads. Since there are no pads with plates still attached, some of the tests cannot be made. Firstly, actuators and DETF cannot be operated simultaneously since there is no connection. Also, the force sensitivity of DETF cannot be tested.

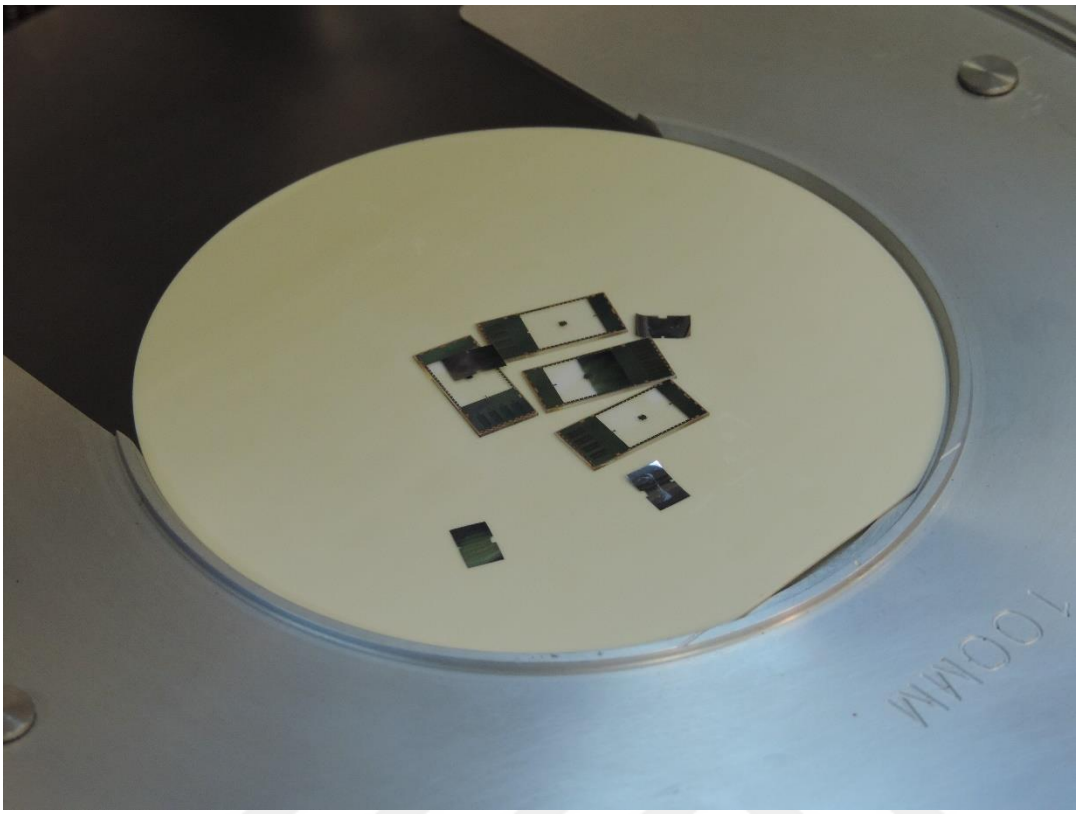

Figure 58. Broke off plates of the sensor during the fabrication processes.

One of the most common fabrication errors in the sensor dies was the undercuts. Undercuts occur as a result of wet etch processes, lithography processes, or gap openings with different sizes during the DRIE process. What undercut does to the performance of the sensor is it can change the resistance along with the actuators, it can change the resonance frequency of the tines of DETF, and it can change the stiffness values of the flexion elements.

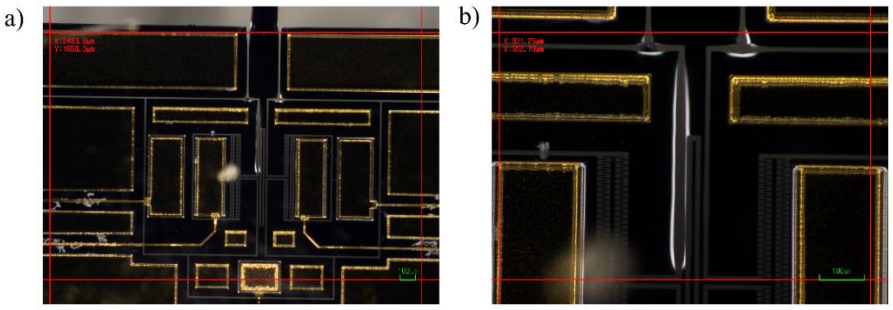

Figure 59. Faulty DETFs because of the undercuts

The other most common error in fabrication was irregularities in critical geometries. Mostly DETF has been affected by this error. By irregularities, DETF tines have different width values along the tines, which makes its resonance frequency to change.

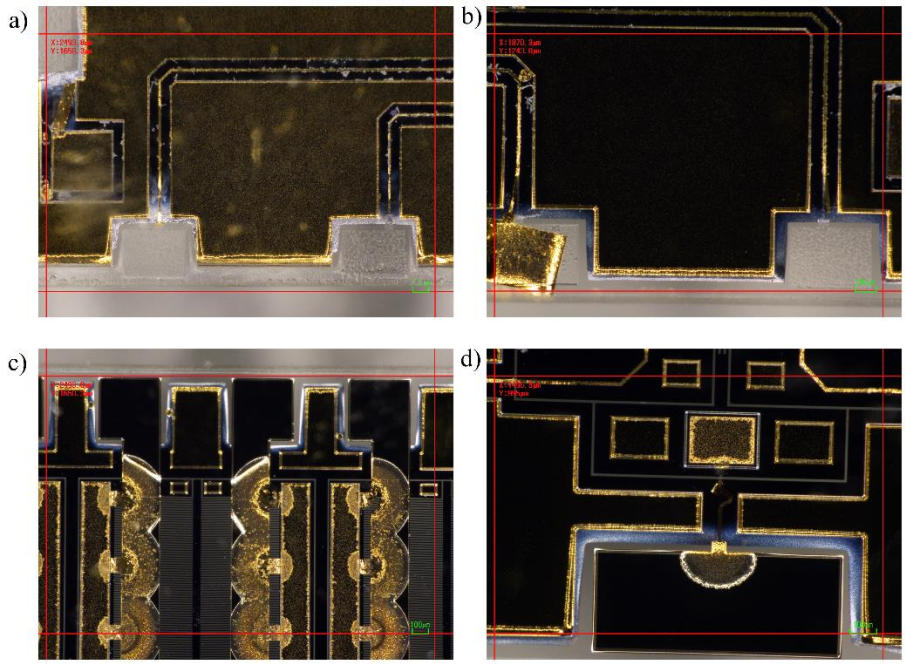

Figure 60. Gold plates of the sensor. a) Broke off gold pads of the DETF part b) Broke of gold pads and faulty gold lines of DETF c) Gold plates under the actuators d) Gold plates of proof mass pads of DETF structure

While designing these elements of the sensor, both undercut and irregularities should be kept in mind. Undercuts do not affect the sensitivity of the designed DETF, but irregularities may have a huge impact on it. In any case, the sensors will be used in the tests to understand how these errors will affect the performance of it.

Not a huge error, but contaminations during the fabrication and wire bonding have also happened. During every step, these types of contaminations had been monitored. If there was contamination on the wafer, necessary actions had been taken to get rid of them; however, there is a chance that there are still small contaminations that cannot be observed with the help of a microscope and SEM.

3.5. **Summary**

In Chapter 3, the fabrication steps and results of the designed and simulated sensor have been presented. All the essential fabrication steps have been illustrated for both of the wafers, and also steps of the bonding of the two wafers have been illustrated. The fabricated sensors have been shown by the microscope and SEM images taken during and after the fabrication steps. Finally, the results of the fabrication have been discussed, and current errors have been presented.

CHAPTER 4

4. TESTS AND MEASUREMENT RESULTS

In this chapter, procedures and equipment of tests for studied actuators, force sensors, and MEMS Test Setup will be explained extensively. Also, results from these tests will be available to see what data the sensors have given. Firstly, V-Type actuators will be tested to see how they deflect under certain potential difference values. Then, necessary tests will be performed to see how the DETF behaves in real life. In Chapter 4.1, the characterization tests of MEMS-based DETF will be explained. In Chapter 4.2, the test setup for actuators and force sensors of the fabricated sensors and the results of them will be explained. Finally, in Chapter 4.3, the summary and conclusion of Chapter 4 will be done.

4.1. **Characterization Tests**

In this part, digitizing the output of a resistor will be done. To do that, a previously mentioned setup with a detection scheme will be prepared. The setup consists of a network analyzer, power supply, resonator, and trans-impedance amplifier. The power supply will be used to provide the DC voltage to the proof mass. By proof mass, capacitance across the sense electrodes and resonating mass will be created. Next is the network analyzer. It will be used to make sure that the tines are resonating. The way it is done is by supplying the AC drive voltage to electrodes by a certain frequency interval while tracking the output voltage. Overall, the detection scheme is created.

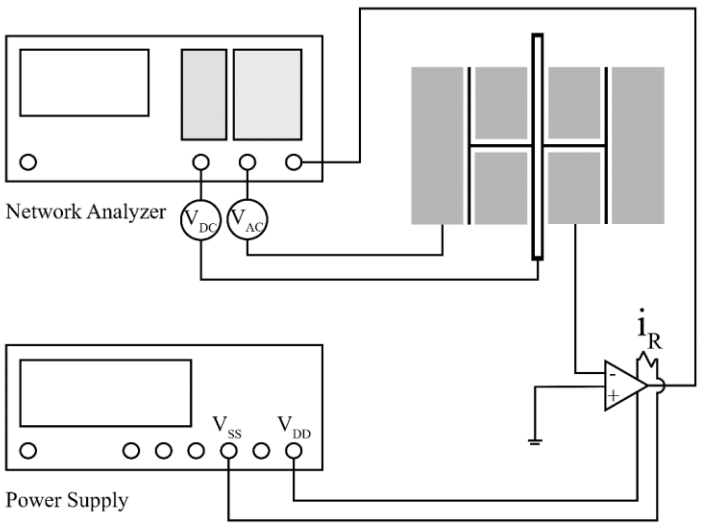

Figure 61. Detection setup which includes network analyzer, DC power supply, trans-impedance amplifier, and the resonator (DETF)

Since the output voltage is easier to handle compared to current, it is preferred to form to control the inputs. It is necessary to convert the current into a voltage and to do that, the trans-impedance amplifier is used because current changes as the tines resonate and the capacitance between the proof mass and sense electrodes change. This generated current is then converted to a voltage by a trans-impedance amplifier. Also, resistance is named gain in this step.

In order to perform the resistance test for the DETF, the test setup in Figure 62 has been prepared. The sensor is placed on a package to easily get the electrical connections and make the tests on the vacuum chamber.

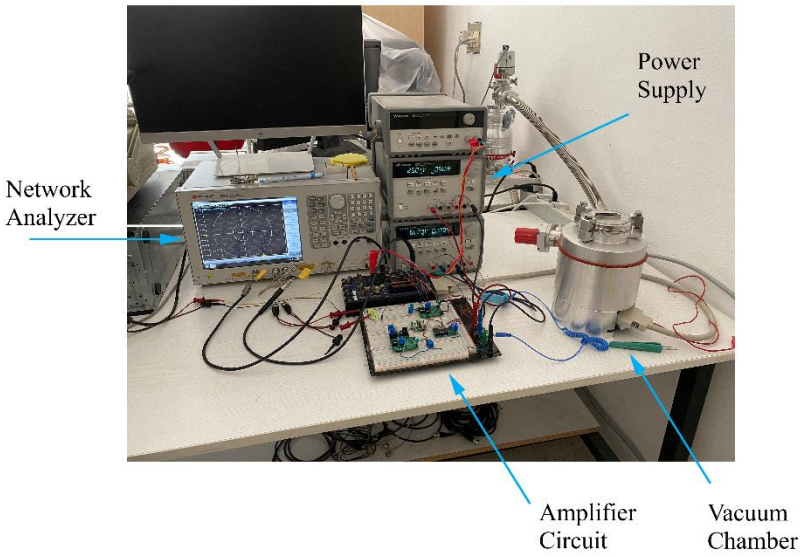

Figure 62. Vacuum chamber test setup for characterization test of DETF

In the test setup, Keysight E5061B network analyzer has been used to track the behavior of the DETF. To get the resonance, sensors are driven with an AC signal, which has a power of -30 dBm on vacuum and -10 dBm on air.

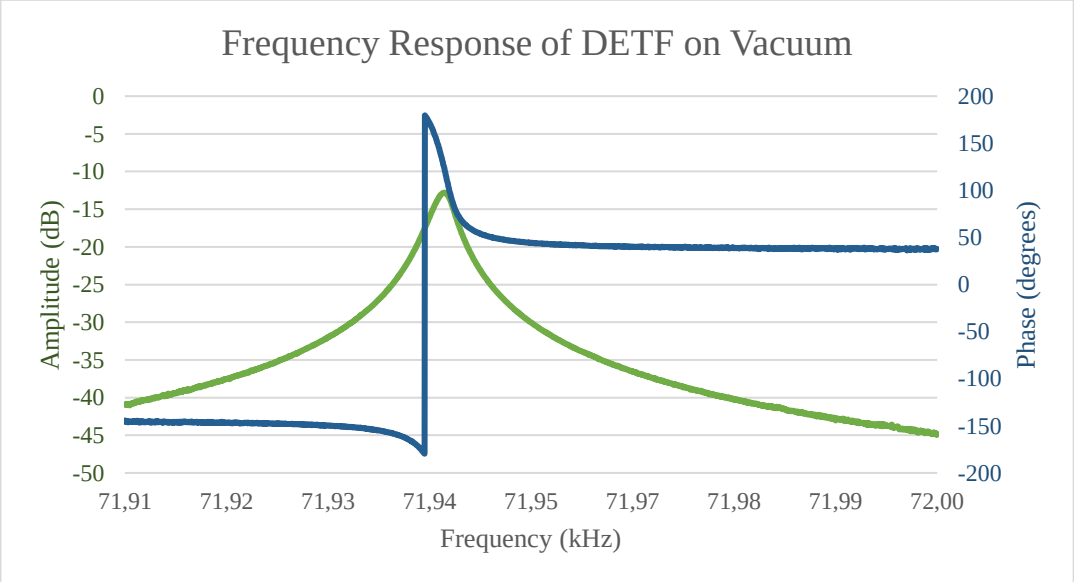

Figure 63. Frequency Response of DETF on Vacuum. A quality factor of 23316 has been obtained

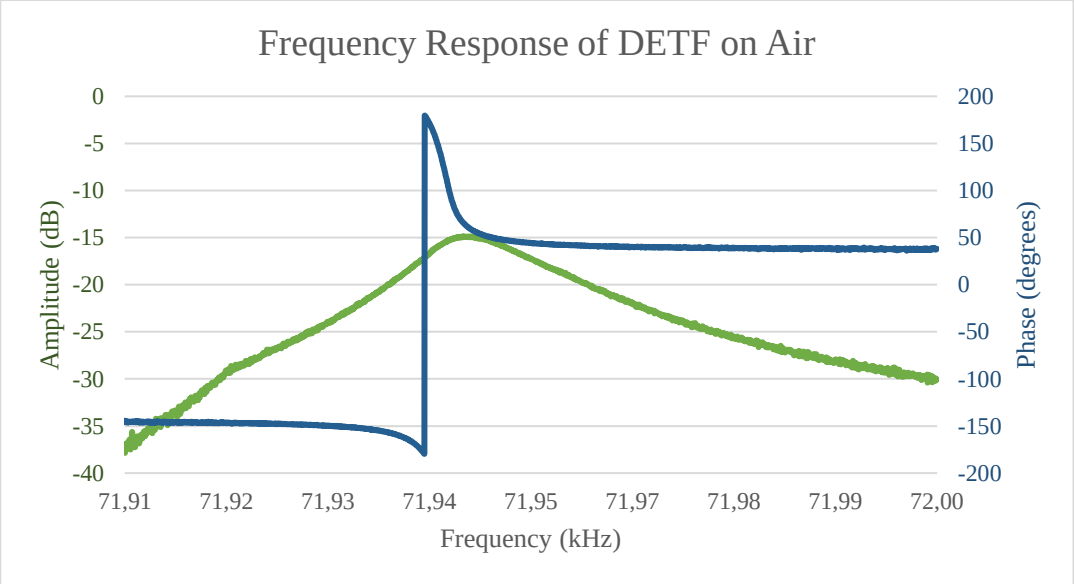

Figure 64. Frequency Response of DETF on Air. Quality Factor of 182 has been obtained

In these tests, the maximum quality factor of 182 in air conditions and 23316 in vacuum conditions are observed. This occurs because of the atmospheric operation conditions and low-quality factor in the air affects the results significantly. In the Figure 63, the frequency response of the sensor in vacuum conditions is shown, and in the Figure 64, the frequency response of the sensor in air conditions is shown. Because of the non-enclosed package, dust and other contaminations were on the sensor during the test.

In Figure 65, the frequency response of DETF on air conditions are observed for varying voltage values to see both in-phase and out-of-phase modes. The peak at the left-hand side is for in-phase mode, and the peak at the right is for out-of-phase mode. It can be seen that in-phase mode is much smaller than the out-of-phase mode, and it is because of the mechanical loss mechanism of in-phase mode.

Changing the voltage affects the peaks in terms of amplitude but not frequency. Compared to the parallel plate DETF's comb drive, DETF's frequency does not get affected by voltage change. In the same figure, it can also be seen. As the voltage decreases, the amplitude of both in-phase and out-of-phase modes decreases.

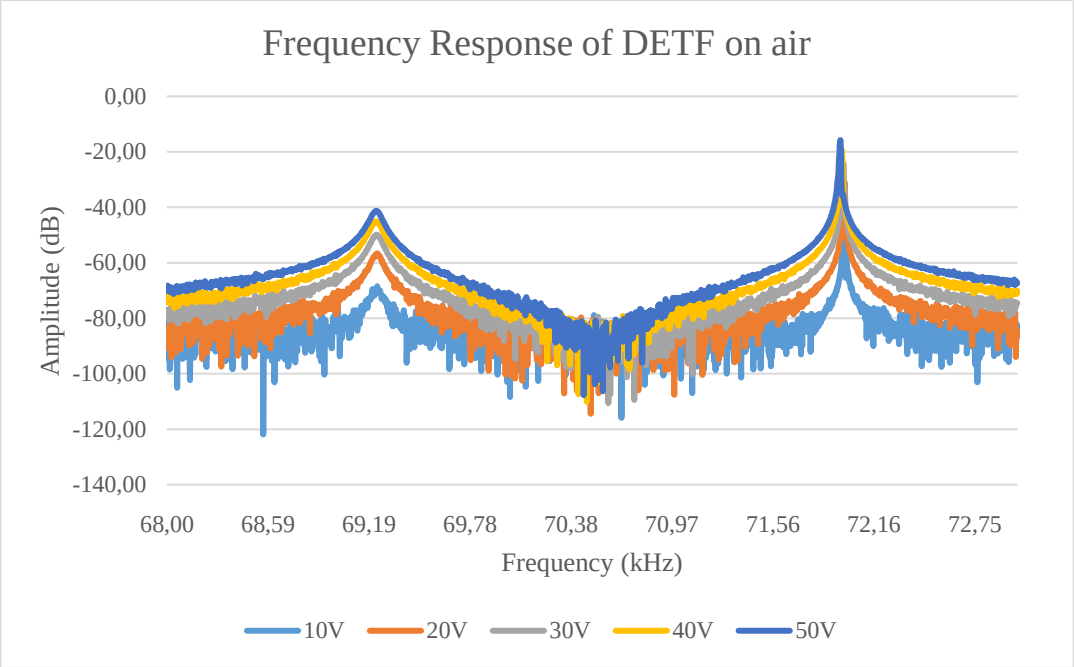

Figure 65. The frequency response of DETF on-air for varying voltage values.

In Table 13, results from the mathematical model, Comsol analysis, and test are compared. It has been seen that the 2-DOF model finds the natural frequency a little bit higher than the others. The difference between the analysis and test can be the result of errors in fabrication. It has been seen that there occur undercuts in the sensor which result in different M_{eff} and K_{eff} values.

Table 13. Natural Frequencies found by the mathematical model, COMSOL analysis and real-time-tests

Mode	2-DOF Model	COMSOL Analysis	Test
Out-of-Phase	79.3 kHz	75.9 kHz	71,9 kHz
In-Phase	76,8 kHz	71,6 kHz	69,2 kHz

4.2. **Measurements**

It was planned to test the DETF by applying displacement on it; however, plates to attach the cells were broke away, and the force generated on the actuators cannot be passed to DETF. For this reason, the deflection effect on the DETF cannot be seen

since the test could not be performed. In the same manner, the effect of a force applied to the DETF again cannot be seen since there was no equipment to apply a force on the DETF.

In order to test the v-type actuators, a probe station has been used to see the effect of the varying voltage values. The test setup for v-type actuators can be seen in the Figure 66. Apart from the probe station, a power supply is also used to supply the DC voltage on the actuators. It should be noted that the deflection of the actuators is measured on the images taken by the microscope.

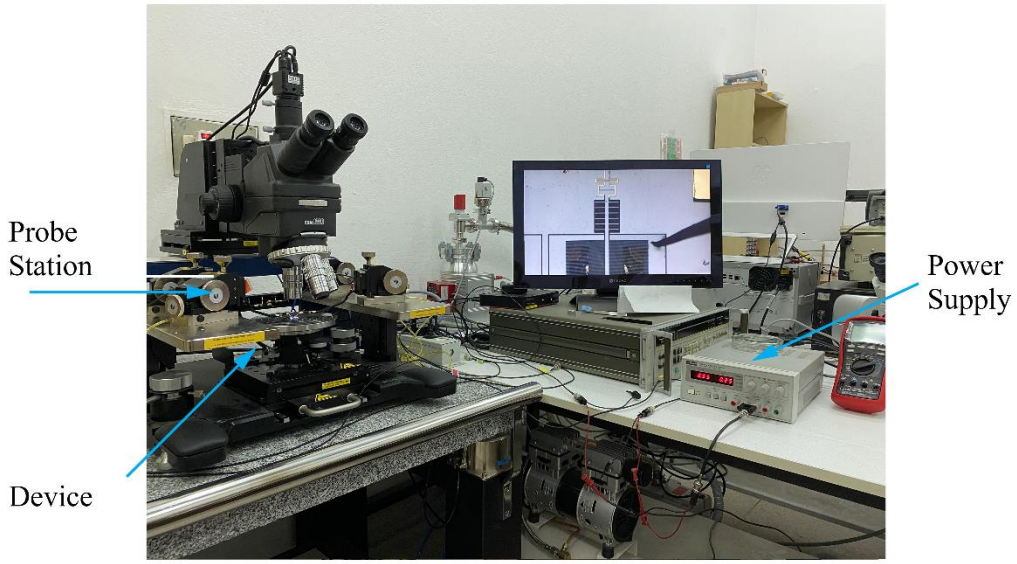

Figure 66. Probe station setup for actuator testing

The fabricated device layer thickness of the sensor is known from the SEM images taken while the fabricating the sensor and dividing the known dimension into the 10 slices, deflection values are estimated. In Figure 67, actuators are deflected on voltage values of 2V, 4V, 6V, and 8V, and the deflections are estimated. In the Figure 13, model, simulation, and test results are tabulated. It can be seen that model and

COMSOL analysis are close, but the test results are slightly smaller. This can be a result of unevenly distributed current across the actuators and fabrication errors. It can be seen that when the actuators are excited, especially in 8V, the shuttle did not move in the right direction; it moved a little bit to the left. This is the result of the fabrication error.

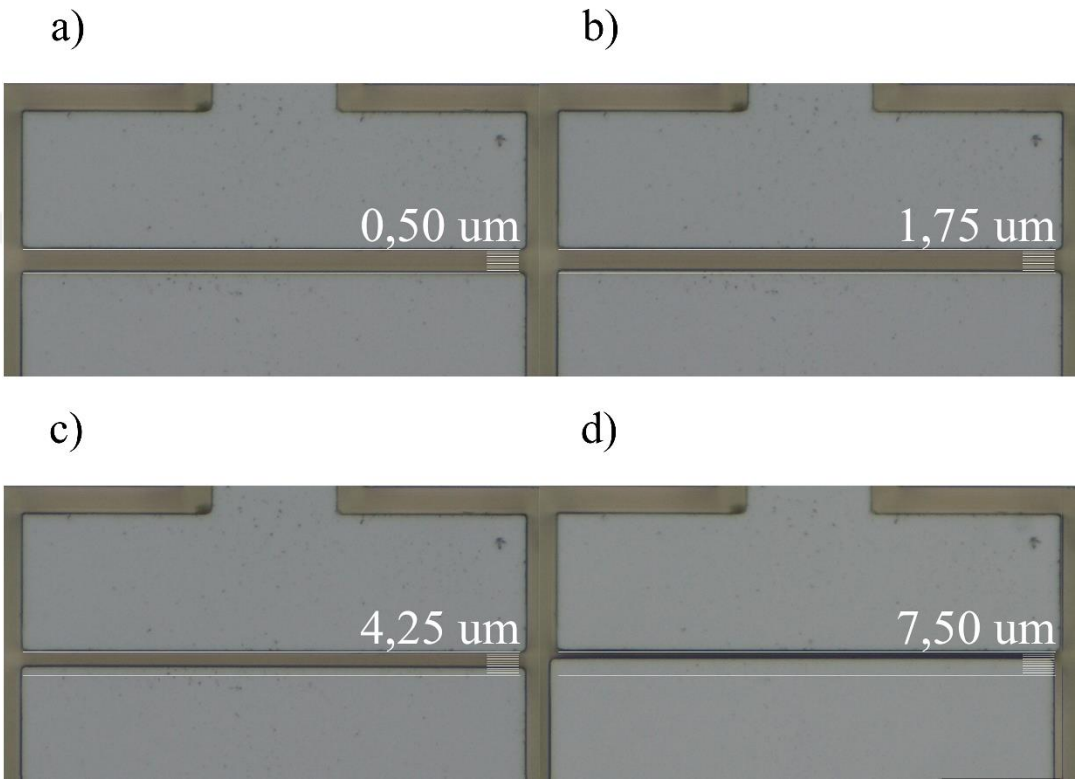

Figure 67. Actuator deflection results. a) DC voltage: 2V b) DC Voltage: 4V c) DC Voltage: 6V d) DC Voltage: 8V

During the test, the DC voltage has been supplied to the sensor by probes on actuators, not on gold pads. It has been seen that placing the probes at the top, middle, and bottom simultaneously results in unevenly distributed actuator displacements. To ignore this, one of the probes placed at the bottom, and the other is placed at the top of the actuator pack. That way, resistance on all of the actuators becomes almost the same, and nearly all of them evenly actuated.

Table 14. Deflection versus voltage values for the fabricated sensor. Mathematical mode, COMSOL, and test results are compared.

Voltage	**Model (μm)**	**COMSOL (μm)**	**Test (μm)**
2V	0.55	0.58	0.50
4V	2.22	2.35	1.75
6V	5.00	5.30	4.25
8V	8.89	9.41	7.50

During the tests, it has been seen that as the voltage increases, the stability of the actuators distorts. Around 7V-8V values, it has been seen that actuators were vibrating significantly but irregularly.

It should also be noted that the resistivity of the wafer is not exactly known. That is because the supplier gives an interval of resistivity value, and the exact value is estimated. The change in the results of analysis or model and test can be because of the error on the resistivity value.

It can be said that these results for both force sensor and the actuators are great to create a bio-tensile test setup. Since the deflection values for the cardiomyocytes should be in the interval of 5 to 10 microns, designed actuators are working as planned. Of course, by increasing the voltage, larger deflection values can be obtained but, in that case, temperature values across the sensor should also be tracked to be sure cells are tested in steady conditions. In addition, it should be kept in mind that actuators are connected to the system by springs so, for 10 μm deflection on the actuators, 5 μm deflection will be present on the cells. Increasing the voltage values to $10 - 11\ V$ can result in near 10 μm deflection on the cells. Also, as seen on the simulations and model of the force sensor, force generated in the mN levels can be tracked by the Double Ended Tuning Fork Force sensor in the system. Of course, the frequency shift at the sensor will not be huge because of the $1 - 2$ mN force values but it can still be tracked to test the cardiomyoctes in this system.

4.3. **Summary and Conclusion**

Test results of the DETF and actuator parts of the sensor are demonstrated in Chapter 4. Along with the characterization tests and test results, test setups and the assembly of them is described extensively. The resonance test has been performed on both the vacuum chamber and air condition. Tests for seeing the deflection and force effects on the DETF could not be performed since the actuators and force sensors are independent as a result of the disconnected plates. To test the actuators, a probe station is used. It has been seen that the analytical model, simulation, and real-time tests are giving close results.

CHAPTER 5

5. CONCLUSION AND FUTURE WORKS

A MEMS-Based test setup with V-Type thermal actuators and Double-Ended Tuning Forks has been studied in this thesis. In Chapter 2, working principles, mechanical design, and analytical models of V-Type Thermal Actuators, Double-Ended Tuning Forks, and overall Test setup has been presented. Analytical models of these devices have been compared to finite element analysis in Chapter 2, which had been performed on COMSOL Multiphysics 5.2 Software. The fabrication processes of the MEMS-Based test setup has been presented in Chapter 3. Finally, in Chapter 4, sensor characterization and system-level test results of both actuators and Double-Ended Tuning Forks have been presented. The conclusions from this study can be summarized as below;

- The theory of the MEMS-based test setup for biological creatures is a new concept. They have been studied on other technologies, but MEMS is not extensively used. In this thesis, MEMS thermal actuator based servo system to create a basis for bio-based test setups have been studied in the literature.
- It has been seen that there are two vital parts of the test setups, force generation mechanism, and force sensing mechanism. For force generation, thermal actuators have been chosen because of their reliable, sturdy, and robust characteristics. For the force sensing part, double-ended tuning forks have been chosen since their stability and resolution are excellent, and it has been studied in the research team extensively before.
- The operation principles of the MEMS-Based V-Type Thermal Actuators have been studied extensively. Both electro-thermal and thermo-mechanical behaviors of the system have been studied and modeled analytically.

Mathematical models of the V-Type actuator has been studied in order to see their performances.

- In order to optimize the geometric parameters of the V-Type Actuators, a Microsoft Office Excel model has been created to show how the parameters affect the performance of the actuators as the voltage has been applied along with the actuator.
- After the determination of the geometric quantities, thanks to Excel Model, Finite Element Modelling has been performed by COMSOL software. Electro-thermo-mechanical simulations are held to simulate the performance of the V-Type actuators.
- The operation principles of the MEMS-Based Double-Ended Tuning Forks as the force sensing mechanism has been studied extensively. The modal behavior of the system has been studied and modeled analytically. Mathematical models of DETF has been studied in order to see its performance.
- In order to optimize the geometric parameters of DETF, a Microsoft Office Excel model has been created to show how the parameters affect the performance of force sensors as both AC and DC has been applied along the DETF.
- After the determination of the geometric quantities, thanks to Excel Model, Finite Element Modelling has been performed by COMSOL software. Modal simulations are held to simulate the performance of DETF.
- The operation principles of the overall setup has been also studied; structural behaviors of the system has been studied and modeled analytically.
- Since the critical elements have been designed, there were only structural elements' geometric quantities left to be determined; a Microsoft Office Excel model has been created to show how these parameters affect the performance of the overall system as the actuators work.

- After the determination of the geometric quantities, thanks to Excel Model, Finite Element Modelling has been performed by COMSOL software on both compressive and tensile states. It has been seen that both states behave differently because of the geometric differences.
- Using the model and COMSOL analysis, frequency response versus applied force behavior of the force-sensing mechanism has been compared. It has been seen that around -0.0725 N pull-in occurred.
- The process flow has presented the fabrication of the overall sensor. The results of the fabrication are illustrated thanks to SEM images, and microscope images of the fabricated sensor dies.
- It has been seen that DETF resonance values hold the mathematical model and COMSOL Analysis. The sensor has been tested in both air and vacuum conditions, and it has been seen that in the vacuum quality factor of 23316 and air quality factor of 182 has been collected. The tests for the frequency response versus applied force on DETF could not be performed since the actuator system and force sensing mechanism becomes independent as a result of breaking plates.
- Actuators have been tested by the probe station to see how the actuators behave under certain voltage values. It has been seen that deflection under these voltage values resulted in a little smaller values than expected.

The studied MEMS-Based test setup, which includes V-Type Thermal Actuators and Double-Ended Tuning Fork, is the major achievement in this thesis. Its performance and applications can be improved with more extensive research. These improvements can be listed as follows;

- Material selection for the cells to attach to the sensor is essential. It has been seen that cells can be attached to the surface more easily when the material of the surface is glass or similar. When the material selection is made correctly, this sensor can work as planned.

- The cell attachment part of the sensor is too big. A more compact design can be achieved by decreasing the cell attachment area. Also, depending on the attachment method, the overall design of the system can be changed such that both actuators and force sensors are placed on the same side of the sensor. The reason for this, if the sensor is placed on a solution to attach the cells, actuators cannot reach the desired temperature values on a solution, or DETF cannot work properly on a solution since the damping on the solution will be much higher than air.
- Since the area for actuators were limited maximum length possible for the actuators have been chosen; however, in order to deflect the actuators in 20-25 μm levels, the temperature should be high, by redesigning the actuators so that the length of the beams of the actuators will be much larger, maximum. Average temperature to reach to the certain deflection levels can be decreased.
- It has been seen that when the V-Type Actuators are packed in series, the behavior of the system changes. Extensive research should be done, and a mathematical model should be created on Microsoft Office Excel to see the behavior of the device on different parameters.
- Tests with living cells cannot be performed since it needs a different professional setup, however, this study showed what problems may occur while developing such a system.

REFERENCES

[1] C. Freund and C. L. Mummery, "Prospects for pluripotent stem cell-derived cardiomyocytes in cardiac cell therapy and as disease models," *J. Cell. Biochem.*, vol. 107, no. 4, pp. 592–599, 2009, doi: 10.1002/jcb.22164.

[2] P. Fomby *et al.*, "Induced Pluripotent stem cells (iPSCs): the emergence of a new champion in tem cell technology-driven biomedical applications," *Ann. Am. Thorac. Soc.*, vol. 12, no. 3, pp. 181–204, 2010, doi: 10.1002/term.

[3] C. Dambrot, R. Passier, D. Atsma, and C. L. Mummery, "Cardiomyocyte differentiation of pluripotent stem cells and their use as cardiac disease models," *Biochem. J.*, vol. 434, no. 1, pp. 25–35, 2011, doi: 10.1042/BJ20101707.

[4] D. van Hoof, J. Krijgsveld, and C. Mummery, "Proteomic analysis of stem cell differentiation and early development," *Cold Spring Harb. Perspect. Biol.*, vol. 4, no. 3, 2012, doi: 10.1101/cshperspect.a008177.

[5] M. Bellin, M. C. Marchetto, F. H. Gage, and C. L. Mummery, "Induced pluripotent stem cells: The new patient?," *Nat. Rev. Mol. Cell Biol.*, vol. 13, no. 11, pp. 713–726, 2012, doi: 10.1038/nrm3448.

[6] M. Mercola, A. Colas, and E. Willems, "Induced pluripotent stem cells in cardiovascular drug discovery," *Circ. Res.*, vol. 112, no. 3, pp. 534–548, 2013, doi: 10.1161/CIRCRESAHA.111.250266.

[7] M. Generali, D. Kehl, A. K. Capulli, K. K. Parker, S. P. Hoerstrup, and B. Weber, "Comparative analysis of poly-glycolic acid-based hybrid polymer starter matrices for in vitro tissue engineering," *Colloids Surfaces B Biointerfaces*, vol. 158, pp. 203–212, 2017, doi: 10.1016/j.colsurfb.2017.06.046.

[8] H. B. van der Worp *et al.*, “Can animal models of disease reliably inform human studies,” *PLoS One*, vol. 12, no. 4, 2017, doi: 10.1371/journal.

[9] E. B. H. & C. D. G. A. D. McClain, J. J.Otten, “Translation of Research Evidence From Animals to Humans,” *Diabetes, Obes. Metab.*, vol. 15, no. 15, pp. 87–90, 2013.

[10] M. Kaste, “Use of animal models has not contributed to development of acute stroke therapies: Pro,” *Stroke*, vol. 36, no. 10, pp. 2323–2324, 2005, doi: 10.1161/01.STR.0000179037.82647.48.

[11] P. Pound, S. Ebrahim, P. Sandercock, M. B. Bracken, and I. Roberts, “Where is the evidence that animal research benefits humans?,” *Br. Med. J.*, vol. 328, no. 7438, pp. 514–517, 2004, doi: 10.1136/bmj.328.7438.514.

[12] D. A. Robinton and G. Q. Daley, “The promise of induced pluriporent stem cells in research and therapy,” vol. 481, no. 7381, pp. 295–305, 2013, doi: 10.1038/nature10761.The.

[13] D. Huh, G. A. Hamilton, and D. E. Ingber, “From Three-Dimensional Cell Culture to Organs-on-Chips,” *Trends Cell Biol*, vol. 21, no. 12, pp. 745–754, 2011, doi: 10.1016/j.tcb.2011.09.005.From.

[14] K. M. Beussman, M. L. Rodriguez, A. Leonard, N. Taparia, C. R. Thompson, and N. J. Sniadecki, “Micropost arrays for measuring stem cell-derived cardiomyocyte contractility,” *Methods*, vol. 94, pp. 43–50, 2016, doi: 10.1016/j.ymeth.2015.09.005.

[15] K. Morishima *et al.*, “Demonstration of a bio-microactuator powered by cultured cardiomyocytes coupled to hydrogel micropillars,” *Sensors Actuators, B Chem.*, vol. 119, no. 1, pp. 345–350, 2006, doi: 10.1016/j.snb.2005.11.063.

[16] K. Kim *et al.*, “Calibrated micropost arrays for biomechanical characterisation of cardiomyocytes,” *Micro Nano Lett.*, vol. 6, no. 5, pp. 317–322, 2011, doi:

10.1049/mnl.2011.0031.

[17] Y. Zhao and X. Zhang, “Cellular mechanics study in cardiac myocytes using PDMS pillars array,” *Sensors Actuators, A Phys.*, vol. 125, no. 2, pp. 398–404, 2006, doi: 10.1016/j.sna.2005.08.032.

[18] A. Kajzar, C. M. Cesa, N. Kirchgeßner, B. Hoffmann, and R. Merkel, “Toward physiological conditions for cell analyses: Forces of heart muscle cells suspended between elastic micropillars,” *Biophys. J.*, vol. 94, no. 5, pp. 1854–1866, 2008, doi: 10.1529/biophysj.107.115766.

[19] J. G. Jacot *et al.*, “Cardiac myocyte force development during differentiation and maturation,” *Ann. N. Y. Acad. Sci.*, vol. 1188, pp. 121–127, 2010, doi: 10.1111/j.1749-6632.2009.05091.x.

[20] A. J. Engler *et al.*, “Embryonic cardiomyocytes beat best on a matrix with heart-like elasticity: Scar-like rigidity inhibits beating,” *J. Cell Sci.*, vol. 121, no. 22, pp. 3794–3802, 2008, doi: 10.1242/jcs.029678.

[21] L. B. Hazeltine *et al.*, “Effects of substrate mechanics on contractility of cardiomyocytes generated from human pluripotent stem cells,” *Int. J. Cell Biol.*, vol. 2012, 2012, doi: 10.1155/2012/508294.

[22] K. Matsudaira, H. Takahashi, and K. Hirayama-shoji, “A MEMS-based measurement system for evaluating the force-length relationship of human induced pluripotent stem cell-derived cardiomyocytes adhered on a substrate,” 2019.

[23] K. Matsudaira, T. V. Nguyen, K. H. Shoji, T. Tsukagoshi, T. Takahata, and I. Shimoyama, “MEMS piezoresistive cantilever for the direct measurement of cardiomyocyte contractile force,” *J. Micromechanics Microengineering*, vol. 27, no. 10, p. aa8350, 2017, doi: 10.1088/1361-6439/aa8350.

[24] K. Matsudaira, T.-V. Nguyen, K. H. Shoji, T. Tsukagoshi, T. Takahata, and I. Shimoyama, “MEMS Force Sensor Array for Evaluating the Contractility of

IPS Cell-Derived Cardiomyocytes," *Transducers*, pp. 36–38, 2017.

[25] J. Guck *et al.*, "Optical Deformability as an Inherent Cell Marker for Testing Malignant Transformation and Metastatic Competence," vol. 88, no. May, pp. 3689–3698, 2005, doi: 10.1529/biophysj.104.045476.

[26] N. Thanh-Vinh *et al.*, "High-sensitivity microelectromechanical systems-based tri-axis force sensor for monitoring cellular traction force," *Micro Nano Lett.*, vol. 11, no. 10, pp. 563–567, 2016, doi: 10.1049/mnl.2016.0246.

[27] C. G. Galbraith, K. M. Yamada, and M. P. Sheetz, "The Relationship between force and focal complex development," *J. Cell Biol.*, vol. 159, no. 4, pp. 695–705, 2002, doi: 10.1083/jcb.200204153.

[28] D. M. Immunotherapeutic, R. Immunol, Y. Wang, E. L. Botvinick, Y. Zhao, and M. W. Berns, "Visualizing the mechanical activation of Src," vol. 434, no. April, 2005, doi: 10.1038/nature03464.

[29] S. Hu *et al.*, "Mechanical anisotropy of adherent cells probed by a three-dimensional Mechanical anisotropy of adherent cells probed by a three-dimensional magnetic twisting device," no. February 2016, 2004, doi: 10.1152/ajpcell.00224.2004.

[30] F. Ziemann, J. Radler, and E. Sackmann, "Local Measurements of Viscoelastic Moduli of Entangled Actin Networks Using an Oscillating Magnetic Bead Micro-Rheometer," vol. 66, no. June, pp. 2210–2216, 1994.

[31] N. Wang, J. P. Butler, D. E. Ingber, N. Wang, J. P. Butler, and E. Donald, "Mechanotransduction Across the Cell Surface and Through the Cytoskeleton Published by : American Association for the Advancement of Science Stable URL : https://www.jstor.org/stable/2881613 Mechanotransduction Across the Cell Surface and Through the Cytos," vol. 260, no. 5111, pp. 1124–1127, 2020.

[32] X. Ding *et al.*, "Surface Acoustic Wave Microfluidics," vol. 13, no. 18, pp.

3626–3649, 2014, doi: 10.1039/c3lc50361e.Surface.

[33] H. D. Espinosa, Y. Zhu, M. Fischer, and J. Hutchinson, “An experimental/computational approach to identify moduli and residual stress in MEMS radio-frequency switches,” *Exp. Mech.*, vol. 43, no. 3, pp. 309–316, 2003, doi: 10.1007/BF02410529.

[34] H. D. Espinosa, B. C. Prorok, and B. Peng, “Plasticity size effects in free-standing submicron polycrystalline FCC films subjected to pure tension,” *J. Mech. Phys. Solids*, vol. 52, no. 3, pp. 667–689, 2004, doi: 10.1016/j.jmps.2003.07.001.

[35] Y. Zhang *et al.*, “A MEMS tensile testing device for mechanical characterization of individual nanowires,” *Proc. IEEE Sensors*, no. November, pp. 2581–2584, 2010, doi: 10.1109/ICSENS.2010.5690164.

[36] D. Zhang, J. M. Breguet, R. Clavel, L. Phillippe, I. Utke, and J. Michler, “In situ tensile testing of individual Co nanowires inside a scanning electron microscope,” *Nanotechnology*, vol. 20, no. 36, 2009, doi: 10.1088/0957-4484/20/36/365706.

[37] M. F. Pantano, B. Calusi, B. Mazzolai, H. D. Espinosa, and N. M. Pugno, “Load Sensor Instability and Optimization of MEMS-based Tensile Testing Devices,” vol. 6, no. July, pp. 1–8, 2019, doi: 10.3389/fmats.2019.00161.

[38] Y. Zhu, A. Corigliano, and H. D. Espinosa, “A thermal actuator for nanoscale in situ microscopy testing: Design and characterization,” *J. Micromechanics Microengineering*, vol. 16, no. 2, pp. 242–253, 2006, doi: 10.1088/0960-1317/16/2/008.

[39] R. A. Bernal *et al.*, “Effect of growth orientation and diameter on the elasticity of GaN nanowires. A combined in situ TEM and atomistic modeling investigation,” *Nano Lett.*, vol. 11, no. 2, pp. 548–555, 2011, doi: 10.1021/nl103450e.

[40] R. Agrawal, B. Peng, E. E. Gdoutos, and H. D. Espinosa, “Elasticity size effects in ZnO nanowires-A combined experimental- computational approach,” *Nano Lett.*, vol. 8, no. 11, pp. 3668–3674, 2008, doi: 10.1021/nl801724b.

[41] S. S. Hazra, M. S. Baker, J. L. Beuth, and M. P. De Boer, “Demonstration of an in situ on-chip tensile tester,” *J. Micromechanics Microengineering*, vol. 19, no. 8, 2009, doi: 10.1088/0960-1317/19/8/082001.

[42] J. J. Brown, A. I. Baca, K. A. Bertness, D. A. Dikin, R. S. Ruoff, and V. M. Bright, “Tensile measurement of single crystal gallium nitride nanowires on MEMS test stages,” *Sensors Actuators A. Phys.*, vol. 166, no. 2, pp. 177–186, 2011, doi: 10.1016/j.sna.2010.04.002.

[43] C. Livermore, “Design Choices: MEMS Actuators,” Cambridge, 2008.

[44] A. A. Geisberger, N. Sarkar, M. Ellis, and G. D. Skidmore, “Electrothermal properties and modeling of polysilicon microthermal actuators,” *J. Microelectromechanical Syst.*, vol. 12, no. 4, pp. 513–523, 2003, doi: 10.1109/JMEMS.2003.815835.

[45] J. S. Park, L. L. Chu, A. D. Oliver, and Y. B. Gianchandani, “Bent-beam electrothermal actuators-Part II: Linear and rotary microengines,” *J. Microelectromechanical Syst.*, vol. 10, no. 2, pp. 255–262, 2001, doi: 10.1109/84.925774.

[46] L. L. Chu and Y. B. Gianchandani, “A micromachined 2D positioner with electrothermal actuation and sub-nanometer capacitive sensing,” *J. Micromechanics Microengineering*, vol. 13, no. 2, pp. 279–285, 2003, doi: 10.1088/0960-1317/13/2/316.

[47] C. Y. Lin and J. C. Chiou, “Design and fabrication of MEMS-based thermally-actuated image stabilizer for cell phone camera,” *Solid. State. Electron.*, vol. 77, pp. 64–71, 2012, doi: 10.1016/j.sse.2012.05.013.

[48] H. Kapels, R. Aigner, and J. Binder, “Fracture strength and fatigue of polysilicon determined by a novel thermal actuator,” *IEEE Trans. Electron Devices*, vol. 47, no. 7, pp. 1522–1528, 2000, doi: 10.1109/16.848302.

[49] E. Nanomaterials, N. Pala, and A. N. Abbas, *Encyclopedia of Nanotechnology*. 2012.

[50] J. Henriksson, M. Gullo, and J. Brugger, “Integrated long-range thermal bimorph actuators for parallelizable Bio-AFM applications,” *Proc. IEEE Sensors*, pp. 1–4, 2012, doi: 10.1109/ICSENS.2012.6411507.

[51] G. E. Fantner, D. J. Burns, A. M. Belcher, I. W. Rangelow, and K. Youcef-Toumi, “DMCMN: In depth characterization and control of AFM cantilevers with integrated sensing and actuation,” *J. Dyn. Syst. Meas. Control. Trans. ASME*, vol. 131, no. 6, pp. 1–13, 2009, doi: 10.1115/1.4000378.

[52] V. Ionescu, “Numerical Investigation of a MEMS Thermal Actuator Performance by Modifying its Geometric Dimensions,” *Procedia Manuf.*, vol. 32, pp. 820–830, 2019, doi: 10.1016/j.promfg.2019.02.290.

[53] N. Suma, V. S. Nagaraja, S. L. Pinjare, K. N. Neethu, and K. M. Sudharshan, “Design and characterization of MEMS thermal actuator,” *2012 Int. Conf. Devices, Circuits Syst. ICDCS 2012*, no. March, pp. 638–642, 2012, doi: 10.1109/ICDCSyst.2012.6188649.

[54] M. S. Baker, J. A. Walraven, T. J. Headley, and R. A. Plass, “Final Report: Compliant Thermo-mechanical MEMS Actuators, LDRD\# 52553, SAND2004-6635.2004,” *Contract*, no. December, 2004.

[55] M. Chiao and L. Lin, “Self-buckling of micromachined beams under resistive heating,” *J. Microelectromechanical Syst.*, vol. 9, no. 1, pp. 146–151, 2000, doi: 10.1109/84.825789.

[56] Q. A. Huang and N. K. S. Lee, “Analysis and design of polysilicon thermal flexure actuator,” *J. Micromechanics Microengineering*, vol. 9, no. 1, pp. 64–

70, 1999, doi: 10.1088/0960-1317/9/1/308.

[57] C. D. Lott, T. W. McLain, J. N. Harb, and L. L. Howell, “Modeling the thermal behavior of a surface-micromachined linear-displacement thermomechanical microactuator,” *Sensors Actuators, A Phys.*, vol. 101, no. 1–2, pp. 239–250, 2002, doi: 10.1016/S0924-4247(02)00202-9.

[58] R. Hickey, D. Sameoto, T. Hubbard, and M. Kujath, “Time and frequency response of two-arm micromachined thermal actuators,” *J. Micromechanics Microengineering*, vol. 13, no. 1, pp. 40–46, 2003, doi: 10.1088/0960-1317/13/1/306.

[59] F. Ma and G. Chen, “Bi-BCM: A Closed-Form Solution for Fixed-Guided Beams in Compliant Mechanisms,” *J. Mech. Robot.*, vol. 9, no. 1, p. 014501, 2016, doi: 10.1115/1.4035084.

[60] J. Varona, M. Tecpoyotl-Torres, and A. A. Hamoui, “Design of MEMS vertical-horizontal chevron thermal actuators,” *Sensors Actuators, A Phys.*, vol. 153, no. 1, pp. 127–130, 2009, doi: 10.1016/j.sna.2009.04.027.

[61] M. J. Sinclair, “A high force low area MEMS thermal actuator,” pp. 127–132, 2002, doi: 10.1109/itherm.2000.866818.

[62] R.-S. Chiorean, “Electro-Thermo-Mechanical Modeling of V-beam Actuators,” *Procedia Technol.*, vol. 19, pp. 56–61, 2015, doi: 10.1016/j.protcy.2015.02.009.

[63] R. S. Chiorean, M. C. Dudescu, M. Pustan, and M. Hardau, “Analytical and Numerical Study on the Maximum Force Developed by a V-beam Thermal Actuator,” *Procedia Technol.*, vol. 12, pp. 359–363, 2014, doi: 10.1016/j.protcy.2013.12.499.

[64] T. Hu, Y. Zhao, Y. Zhao, and W. Ren, “Integration design of a MEMS based fuze,” *Sensors Actuators, A Phys.*, vol. 268, pp. 193–200, 2017, doi: 10.1016/j.sna.2017.09.051.

[65] M. F. Pantano and N. M. Pugno, “Design of a bent beam electrothermal actuator for in situ tensile testing of ceramic nanostructures,” *J. Eur. Ceram. Soc.*, vol. 34, no. 11, pp. 2767–2773, 2014, doi: 10.1016/j.jeurceramsoc.2013.12.001.

[66] S. Vamegh Estahbanati, R. Dhaouadi, and M. Bakri-Kassem, “Macromodeling of thermally driven V-shaped MEMS actuators,” *Mechatronics*, vol. 46, pp. 193–204, 2017, doi: 10.1016/j.mechatronics.2017.03.006.

[67] J. K. Luo, A. J. Flewitt, S. M. Spearing, N. A. Fleck, and W. I. Milne, “Three types of planar structure microspring electro-thermal actuators with insulating beam constraints,” *J. Micromechanics Microengineering*, vol. 15, no. 8, pp. 1527–1535, 2005, doi: 10.1088/0960-1317/15/8/022.

[68] N. D. Mankame and G. K. Ananthasuresh, “Comprehensive thermal modelling and characterization of an electro-thermal-compliant microactuator,” *J. Micromechanics Microengineering*, vol. 11, no. 5, pp. 452–462, 2001, doi: 10.1088/0960-1317/11/5/303.

[69] G. Stemme, “Resonant silicon sensors,” *J. Micromechanics Microengineering*, vol. 1, no. 2, pp. 113–125, 1991, doi: 10.1088/0960-1317/1/2/004.

[70] H. Dessalegn and T. Srinivas, “Optical MEMS pressure sensor based on double ring resonator,” *2013 Int. Conf. Microw. Photonics, ICMAP 2013*, pp. 1–4, 2013, doi: 10.1109/ICMAP.2013.6733554.

[71] C. Errando-Herranz, F. Niklaus, G. Stemme, and K. B. Gylfason, “A MEMS tunable photonic ring resonator with small footprint and large free spectral range,” *2015 Transducers - 2015 18th Int. Conf. Solid-State Sensors, Actuators Microsystems, TRANSDUCERS 2015*, pp. 1001–1004, 2015, doi: 10.1109/TRANSDUCERS.2015.7181094.

[72] G. Wu, D. Xu, X. Sun, B. Xiong, and Y. Wang, “Wafer-level vacuum packaging for microsystems using glass frit bonding,” *IEEE Trans. Components, Packag. Manuf. Technol.*, vol. 3, no. 10, pp. 1640–1646, 2013, doi: 10.1109/TCPMT.2013.2279135.

[73] M. Rinaldi, Y. Hui, C. Zuniga, A. Tazzoli, and G. Piazza, “High frequency AlN MEMS resonators with integrated nano hot plate for temperature controlled operation,” *2012 IEEE Int. Freq. Control Symp. IFCS 2012, Proc.*, pp. 355–359, 2012, doi: 10.1109/FCS.2012.6243641.

[74] P. Hauptmann, R. Lucklum, and J. Schröder, “Recent trends in bulk acoustic wave resonator sensors,” *Proc. IEEE Ultrason. Symp.*, vol. 1, no. c, pp. 56–65, 2003, doi: 10.1109/ultsym.2003.1293356.

[75] K. Azgin, T. Akin, and L. Valdevit, “Ultrahigh-dynamic-range resonant MEMS load cells for micromechanical test frames,” *J. Microelectromechanical Syst.*, vol. 21, no. 6, pp. 1519–1529, 2012, doi: 10.1109/JMEMS.2012.2211576.

[76] H. A. C. Tilmans and S. Bouwstra, “A novel design of a highly sensitive low differential-pressure sensor using built-in resonant strain gauges,” *J. Micromechanics Microengineering*, vol. 3, no. 4, pp. 198–202, 1993, doi: 10.1088/0960-1317/3/4/007.

[77] S. Seok, H. Kim, and K. Chun, “An inertial-grade laterally-driven MEMS differential resonant accelerometer,” *Proc. IEEE Sensors*, vol. 2, pp. 654–657, 2004, doi: 10.1109/icsens.2004.1426251.

[78] Y. Bin Jia, Y. L. Hao, and R. Zhang, “Double tuning-fork resonant accelerometer,” *Int. Conf. Solid-State Integr. Circuits Technol. Proceedings, ICSICT*, vol. 3, no. 100871, pp. 1812–1815, 2004, doi: 10.1109/icsict.2004.1435186.

[79] R. G. Azevedo *et al.*, “Silicon carbide coated mems strain sensor for harsh environment applications,” *Proc. IEEE Int. Conf. Micro Electro Mech. Syst.*, no. January, pp. 643–646, 2007, doi: 10.1109/memsys.2007.4433166.

[80] A. Torrents, K. Azgin, S. W. Godfrey, E. S. Topalli, T. Akin, and L. Valdevit, “MEMS resonant load cells for micro-mechanical test frames: Feasibility study and optimal design,” *J. Micromechanics Microengineering*, vol. 20, no. 12, 2010, doi: 10.1088/0960-1317/20/12/125004.

[81] K. Azgın, “Very High Dynamic Range Resonant MEMS Load Cells For Micromechanical Test Frames,” Universirty of California, Irvine, 2012.

[82] K. Azgın, “High Performance MEMS Gyroscopes,” Middle East Technical University, 2007.

[83] W. Wai-Chi, A. A. Azid, and B. Y. Majlis, “Formulation of Stiffness Constant and Effective Mass for a Folded Beam,” *Arch. Mech.*, vol. 62, no. 5, pp. 405–418, 2010, doi: 10.1021/jo5027595.